Democratic and Popular Republic of Algeria

Ministry of Higher Education and Scientific Research

University Mohamed Khider of Biskra

Faculty of Exact Sciences and Science of Nature and Life

Department of Material Sciences

Thesis

Presented to obtain the degree of

Doctorate of Sciences

Speciality: Physics of Materials

Deposition and analysis of Zinc Oxide thin films elaborated using spray pyrolysis for photovoltaic applications

Presented by:

BOUAICHI FOUAD

Publicly defended on: 18 / 07 / 2019

To the Jury composed by:

M^r^. A. Chala	Professor	University of Biskra	President
M^r^. A. Attaf	Professor	University of Biskra	Supervisor
Mme. H. Saidi	Professor	University of Biskra	Co-Supervisor
M^r^. N. Attaf	Professor	University of Cons1	Examiner
M^r^. D. Belbacha	Professor	University of Batna1	Examiner
M^r^. A. Naas	MCA	University of Djelfa	Examiner

Academic year 2018-2019

Table of contents

Acknowledgements I

List of Tables II

List of figures III

General Introduction 1

Chapter I: *Review of the Zinc Oxide Thin Films Properties and Growth techniques.*

I.1. **Introduction** 5

I.2. **Chapter Objectives** 5

I.3. **Transparent conducting oxides** 5

I.3.1. Definition 5

I.3.2. TCOs in General 5

I.4. **History of Zinc oxide (ZnO) research** 6

I.5. **ZnO choice** 7

I.6. **Properties of Zinc Oxide** 8

I.6.1. Crystal Structure 8

I.6.2. Electronic band structure of ZnO 10

I.7. **Doping of ZnO** 12

I.8. **ZnO thin films applications** 13

I.8.1. ZnO thin films for photovoltaics 14

I.9. **Different growth techniques of ZnO** 15

I.9.1. Chemical Vapour Deposition 17

I.9.2. Physical Vapour Deposition 18

I.9.3. Radio frequency magnetron sputtering 19

I.9.4. Laser Ablation 20

I.9.5. Sol gel 21

References 24

Chapter II: *Growth process and characterization devices for ZnO thin films*

II.1. **Introduction** 28

II.2. **Chapter Objectives**………………………………………………………….……….. 28
II.3. **Experimental technique**…………………………………………..………….. 28
II.3.1. Spray pyrolysis technique……………………………………………………….. 28
II.3.1.1. General Description of Spray pyrolysis…………………………………..… 28
II.3.1.2. Decomposition of precursor………………………………………………… 31
II.4. **Spray Apparatus**…………………………………………..…..…………… 31
II.4.1. Specifications……………………………………………...…..……… 31
II.4.2. Equipment components……………………………………..……...…… 32
II.4.2.1. Spray pneumatic components……………………………..……..…… 34
II.4.2.1.1. Air compressor……………………………..…………..…………… 34
II.4.2.1.2. Syringe pump (Flow rate controller) …………………………..………… 34
II.4.2.2. Spray ultrasonic components…………………...…………………..………… 34
II.4.2.2.1. Ultrasonic generator…………………………………………..…..……… 34
II.4.2.2.2. Solution flow rate controller……………………………………..……… 34
II.4.2.3. Common components…………………………..……………..……… 34
II.4.2.3.1. Scanning system (XY position controller) ……………………..…..…… 34
II.4.2.3.2. Hot plate……………………………………………………..………… 34
II.4.2.4. Holmac’s software………………………………………...…..………… 34
II.5. **Growth process details**……………………………………………….……… 35
II.5.1. Substrate preparation………………………………………..…..………… 35
II.5.1.1. Substrate selection……………………………………………....………… 35
II.5.1.2. Substrate cleaning…………………………………………....………… 35
II.5.2. Preparation of precursor solution…………………………………..………… 36
II.5.3. Films deposition……………………………………………………..……….. 37
II.6. **Characterization Methods of Thin Films**………………………………………… 40
II.6.1. X-ray Diffraction Technique…………………………………..……..………… 40
II.6.1.1. The texture coefficient…………………………………………..………… 42
II.6.1.2. Grain size determination……………………………..……………..……… 43
II.6.1.3. Stress determination……………………………………………..………… 43
II.6.2. Scanning electron microscopy (SEM) ……………………………………..……… 44
II.6.3. Film thickness calculation…………………………………………….……… 46
II.6.3.1. Scanning electron microscopy………………………………………………… 46
II.6.3.2. UV-Visible Spectrophotometry……………………..……………………… 47
II.6.3.3. Weight difference method…………………………………………..………… 47
II.6.4. HebalOptics software……………………………………..………………… 48

II.6.5. Optical characterization……………………………………………………… 49
II.6.5.1. UV-Vis spectroscopy……………………………………………………… 49
II.6.5.2. The absorption coefficient……………………………………………… 51
II.6.5.3. Refractive index and extinction coefficient calculation……………………… 51
II.6.5.4. Band gap energy………………………………………………………… 51
II.6.5.5. Urbach energy…………………………………………………………… 52
II.6.6. Electrical resistivity measurement…………………………………………… 53
II.6.6.1. Four probes method……………………………………………………… 53
II.6.6.2. Electrical resistivity calculation………………………………………… 54
II.6.7.1. Hall effect measurement………………………………………………… 55
References……………………………………………………………………… 58

Chapter III: Results and Discussion - Ultrasonic Spray

III.1. Introduction………………………………………………………………… 61
III.2. Chapter Objectives…………………………………………………………… 61
III.3.Effect of Molarity…………………………………………………………… 61
III.3.1. Structural Characterization……………………………………………… 61
III.3.1.1. The texture coefficient………………………………………………… 63
III.3.1.2. Grain size determination……………………………………………… 64
III.3.1.3. Stress variation of ZnO thin films…………………………………… 65
III.3.1.4. Film thickness calculation of ZnO thin films……………………………… 66
III.3.1.5. Surface Morphology (Scanning electron microscopy) ……………………… 67
III.3.2. Optical characterization (UV-Vis) ……………………………………… 67
II.3.2.1. Band gap energy and urbach energy……………………………………… 68
III.3.3. Electrical characterization……………………………………………… 70
III.3.3.1. Resistivity of Zinc Oxide Films………………………………………… 70
III.3.4. In summary ……………………………………………………………… 70
III.4. **Effect of dopants**……………………………………………………………… 71
III.4.1. **Effect of aluminium doping**……………………………………………… 71
III.4.1.1. Structural Characterization…………………………………………… 71
III.4.1.1.1.The texture coefficient………………………………………………… 73
III.4.1.1.2. Grain size variation of Al-doped ZnO thin films……………………… 75
III.4.1.1.3. Stress variation of Al-doped ZnO thin films…………………………… 77

III.4.1.1.4. Film thickness calculation of Al-doped ZnO thin films……………………… 78
III.4.1.1.5. Surface Morphology (Scanning electron microscopy) ……………………… 79
III.4.1.1.6. The Energy X-ray Dispersive Spectroscopy (EDS)…………………………. 81
III.4.1.2. Optical characterization (UV-Vis) ……………………………………………….. 82
III.4.1.2.1. Band gap energy Urbach energy………………………………………………… 83
III.4.1.3. Electrical characterization……………………………………………………… 85
III.4.1.3.1. Resistivity of Al-doped ZnO thin Films……………………………………… 85
III.4.1.4. In summary ……………………………………………………………………….. 87
III.4.2.**Effect of Indium doping**……………………………………………………… 88
III.4.2.1.Structural Characterization………………………………………………………… 88
III.4.2.1.1.The texture coefficient……………………………………………………… 90
III.4.2.1.2.Grain size of Indium ZnO thin films…………………………………………… 91
III.4.2.1.3.Stress variation of In-doped ZnO thin films ………………………………… 92
III.4.2.1.4.Film thickness calculation of In-doped ZnO thin films……………………… 93
III.4.2.2.Optical characterization (UV-Vis) …………………………………………… 94
III.4.2.2.1.Band gap energy and urbach energy……………………………………… 95
III.4.2.3.Electrical characterization……………………………………………………… 97
III.4.2.3.1.Electrical conductivity of In-doped ZnO thin films…………………………… 97
References…………………………………………………………………………… 99

Chapter IV: *Results and Discussion - Pneumatic Spray*

IV.1. Introduction………………………………………………………………….. 104
IV.2. Chapter Objectives…………………………………………………………….. 104
IV.3.Effect of Substrate temperature…………………………………………… 104
IV.3.1. Part one: Substrate temperature – Spray pressure: 1,5 bar ………………… 104
IV.3.1.1.Structural Characterization…………………………………………………… 104
IV.3.1.1.1.Grains size of undoped ZnO thin films………………………………… 106
IV.3.1.1.2.Stress variation of undoped ZnO thin films……………………………… 107
IV.3.1.1.3.Film thickness of undoped ZnO thin films ……………………………… 109
IV.3.1.2.Optical characterization (UV-Vis) …………………………………………… 110
IV.3.1.2.1.Band gap energy and Urbach energy of undoped ZnO…………………… 111
IV.3.1.3.Electrical characterization…………………………………………………….. 112
IV.3.1.3.1.Resistivity of Zinc Oxide Films…………………………………………. 112

IV.3.2.Part two: Substrate temperature – Spray pressure: 1 bar………...…..….… 113
IV.3.2.1.Structural Characterization………………..…………………………………… 114
IV.3.2.1.1.Grain size calculation of undoped ZnO thin films…………………………… 115
IV.3.2.1.2.Stress variation of undoped ZnO thin films……………………….….…… 116
IV.3.2.1.3.Film thickness variation of undoped ZnO thin films………………….……… 118
IV.3.2.2.Optical characterization (UV-Vis) ………………..…………………………… 118
IV.3.2.2.1.Band gap energy and Urbach energy …………………...…………….…… 119
IV.3.2.3.Electrical characterization……………………………………………………… 121
IV.3.2.3.1.Resistivity of Zinc Oxide thin films……………..…………………………… 121
III.3.2.4. In summary ……………………………………………………………………. 122
IV.4.Effect of Aluminium doping………...……………..…………………...………… 123
IV.4.1.Structural Characterization…………………………….………………………… 123
IV.4.1.1.Grain size calculation of Al-doped ZnO thin films……………….………… 126
IV.4.1.2.Stress variation of Al-doped ZnO thin films……….…………………...…… 127
IV.4.2.1.3. Film thickness variation of Al-doped ZnO thin films…………….………… 128
IV.4.2.Optical characterization (UV-Vis) ……………….………………………….…… 129
IV.4.2.1.Band gap energy and Urbach energy of Al-doped ZnO thin films………..…… 130
IV.4.3.Electrical characterization…………………………………………………….……… 132
IV.4.3.1.Electrical conductivity of Al-doped ZnO thin films ……..…………………… 132
III.4.4. In summary ……………………………………………………………………… 133
References…………………...……………………………………………………...... 134

General Conclusion……..…………………………..………………………...... 136

Abstract ……..………………………..…………………………………...... 138

"In the name of Allah, The most merciful and the most beneficial"

Acknowledgments

At the outset, I bow my head before the almighty 'ALLAH', the Lord of worlds who endowed me with the enough vehemence to complete the task. Words are not enough to praise and thank for all the things given.

My foremost thanks go to my supervisor Professor ***Mr. Attaf Abdallah***, Professor at Mohamed Khider University of Biskra, I thank him greatly with regards for his patience and encouragement that carried me on through difficult times and for his insights and suggestions that helped to shape my research skills. Besides of being an excellent supervisor, he was as close as a relative and a good friend to me.

I am thankful to **Mrs. Saidi Hanane**, Co-Supervisor of my thesis, Professor at Mohamed Khider University of Biskra for her support and advice, encouraged me, and helped me to carry out this work.

I am honored that **Mr. Abdlouahed Chala**, Professor at Mohamed Khider University of Biskra, has agreed to chair the jury of my thesis. I thank him warmly.

I also thank **Mr. Nadhir Attaf**, Professor at the University of Constantine 1, **Mr. El- Djemai Belbacha**, Professor at the University of Batna 1, and **Mr. Abdelkarim Naas**, MCA at University of Djelfa, for having agreed to do part of the jury of this thesis as examiners, that their remarks and their criticisms are welcome. I thank everyone in the discussion committee for accepting the request and i am grateful to them for reading my thesis and thanks and gratitude to Professor ***Mr. Aida Mohamed Salah*,** a Professor at King Abdulaziz University, Jeddah for his advice and opinions, which he did not hesitate to give with confidence in this work.

With immense pleasure, i would tkank ***Dr. Mohamed Othmane*** without his continuous support this study would not have been completed.

Many thanks and regards to ***Mr. Saad Rahmane*** Professor in the Department of Physics of the Faculty of Exact Sciences of the University of Biskra for providing me the logistic support and and nice suggestions from time to time. I thank ***Mr.Toufik Tebermacine***, Professor in the Department of Physics of the Faculty of Exact Sciences of the University of Biskra, for all the electrical measurements made on my thin films, my utmost gratitude to ***Mr. Gasmi Brahim***, engineer at the Mohamed Khider University of Biskra for his kindness and help for his contribution to X-ray diffraction measurements (XRD).

I would like to express my gratitude to my ***mother***, brothers and sister, for their support and encouragement throughout my education and life. They have instilled in me a work ethic and ambition that has led me this far.

I would also like to show my love and thanks to my wife ***safia*** and my children ***Ayoub sirajeddine*** and ***elbatoul*** for giving me encouragement and support during my academic study.

In the end, I would also like to thank all of my friends and coworkers from our laboratory (Laboratoire de Physique des Couches Minces et Applications « LPCMA ») who have contributed greatly during my graduate program.

List of Tables

Tab I.1: Physical properties of the zinc oxide in the wurtzite form………..………… 10
Tab I.2: Survey and classification of thin-film deposition technologies……………… 16

Tab II.1: Table presents Holmarc's Spray Pyrolysis Equipment Specifications……... 32
Tab II.2: the experimental conditions of the deposit ZnO thin films, for ultrasonic… process. 38
Tab II.3: the experimental conditions of the deposit ZnO thin films, for pneumatic… process. 38

Tab III.1: Properties of ZnO films deposited by spray pyrolysis technique at… different solution molarities. 64
Tab III.2: results of undoped ZnO thin films deposited at deferent solution… molarities. 64
Tab III.3: peaks diffraction angles (2θ) and FWHM of Al-doped ZnO thin films…. with different doping rates. 73
Tab III.4: Diffraction angle, FWHM and Grain size of ZnO films deposited at… different Aluminium doping rates. 76
Tab III.5: results of the whole Al doping ZnO thin films……………………………. 78
Tab III.6: calculated optical band gap and Urbach energy of undoped ZnO thin… films. 85
Tab III.7: measured electrical resistivity and conductivity of Al-doped ZnO thin… films deposited with varied doping rates. 86
Tab III.8: the electrical and optical properties of Al-doped ZnO thin films……….. 87
Tab III.9: diffraction angles, FWHM and the grain size measurements……………… 92
Tab III.10: Results of In doped ZnO thin films deposited at varied doping rates…… 93
Tab III.11: The optical band gap Eg and Urbach energy Eu of In-doped ZnO thin… films. 96
Tab III.12: estimated electrical resistivity and conductivity of In-doped ZnO thin… films. 98

Tab IV.1: peaks diffraction angles (2θ) and intensity of ZnO films deposited at… various substrate temperatures with 1.5 bar as carrier gas pressure. 106
Tab IV.2: Variation of diffraction angle, FWHM and Grain size with substrate… temperature of ZnO films deposited at 1.5 bar as carrier gas pressure. 107
Tab IV.3: Results of undoped ZnO thin films deposited at varied substrate… temperatures. 108
Tab IV.4: calculated optical band gap and Urbach energy of undoped ZnO thin… films. 112
Tab IV.5: measured electrical resistivity and conductivity of undoped ZnO thin….. films deposited at varied substrate temperatures. 113
Tab IV.6: peaks diffraction angles (2θ) and intensity of ZnO films deposited at… various substrate temperatures with 1 bar as carrier gas pressure. 115

Tab IV.7: Variation of diffraction angle, FWHM and Grain size with substrate… temperature of ZnO films deposited at 1 bar as carrier gas pressure. 116
Tab IV.8: Results of undoped ZnO thin films deposited at varied substrate…. temperatures. 118
Tab IV.9: calculated optical band gap and Urbach energy of undoped ZnO thin… films. 120
Tab IV.10: measured electrical resistivity and conductivity of undoped ZnO thin….. films deposited at varied substrate temperatures. 121
Tab IV-11: Variation of diffraction angle (2θ), FWHM and intensity with………. Al-doping rate. 127
Tab IV.12: Results of Al-doped ZnO thin films deposited at varied aluminium… doping rates. 128
Tab IV.13: calculated optical band gap and Urbach energy of Al-doped ZnO thin… films. 131
Tab IV.14: measured electrical resistivity and conductivity of Al-doped ZnO thin… films. 133

List of figures

FigI.1: increase of the number of publications about zinc oxide according to the... literature data base SCOPUS. 6
FigI.2: (a) An orange zincite crystal, (b) a synthetic zinc oxide crystal. The mineral... in (a) exhibits a size of 30×25×6 mm^3. 8
FigI.3: Crystal structures of ZnO (a) rocksalt (b) zinc blend and (c) wurtzite... hexagonal. Shaded gray and black spheres denote Zn and O atoms, respectively. 9
FigI.4: Wurtzite ZnO crystal structures from different angles............................ 9
FigI.5: Band structure and symmetries of hexagonal ZnO. The splitting into the..... three valence bands (A, B, C) is jointly caused by the crystal field and spin-orbit splittings 11
FigI.6: The Bulk band structure of the ZnO crystal....................................... 11
FigI.7: Schematic representation the applications of ZnO.............................. 13
FigI.8: Actual photovoltaic structures: (a) Copper Indium Gallium Selenide (CIGS)... seen in cross section using SEM. (b) Schematic illustrations of the structures. 15
FigI.9: Chemical thin film deposition methods... 15
FigI.10: Schematic of the CVD process... 17
FigI.11: Schematic of a typical thermal or electron-beam evaporation system. The... source material is heated by an electrical current in thermal evaporation or by bombardment by an electron beam in electron-beam evaporation. 18
FigI.12: Schematic (not to scale) of rf (radio-frequency) magnetron sputtering......... 19
FigI.13: Schematic of the PLD process.. 21
FigI.14: shows the steps of the sol-gel processing of materials and examples of the... microstructures of final products. Bold-lined rectangles show possible final products of the sol-gel method. 22
FigI.15: Schematic diagram of sol-gel, (a) spin-coating (b) dip-coating.............. 23

FigII.1: Diagram showing the breakup of a liquid jet by high pressure gas............. 29
FigII.2: Standing surface waves patterns during the ultrasonic atomisation ...... (water, f=50kHz). 30
FigII.3: Mechanism of droplet break-up for the ultrasonic atomisation.................. 30
FigII.4: Description of the deposition processes initiated with increasing substrate... temperature. 30
FigII.5: Schematic diagram of Holmarc's spray pyrolysis system (pneumatic system).. 33
FigII.6: Schematic diagram of Holmarc's spray pyrolysis system (ultrasonic system)... 33
FigII.7: Holmac's software interface... 35
FigII.8: Schematic illustration of the Cleaning Process of the substrates................ 36
FigII.9: Schematic diagram of Bragg diffraction from set parallel planes............... 40
FigII.10: D8 ADVANCE diffractometer.. 41
FigII.11: The schematic diagram of X-ray diffractometer optical system............... 41
FigII.12: X-ray diffraction spectrum (XRD) with stoichiometric ZnO powder..... (ASTM 36-1451). 42
FigII.13: A schematic representation of the sub-surface electron interaction volume... 44
FigII.14: Schematic diagram of the electron gun column of a SEM..................... 45

FigII.15: JSM-6301F scanning electron microscope……………………………….. 46
FigII.16: SEM cross section photograph of Al-doped ZnO (1 at%), Shows that….. the thickness is about 300nm. 46
FigII.17: UV/VIS/NIR transmission curve of ZnO film…………………………….. 47
FigII.18: the sample dimensions used to calculate film thickness…………………… 48
FigII.19: Transmittance of light through a sample…………………………………… 49
FigII.20: Simplified schematic diagram of the CARY model 14 spectrometer……… 50
FigII.21: band gap energy determination using an linear region extrapolation of a… plot *(αhυ)*^{2} as a function of photon energy for a ZnO thin film doped by Al at 3 at%. 52
FigII.22: Four-points probe…………………………………………………………. 53
FigII.23: **C4S4 –Point Probe Head model,** four points device……………………… 54
FigII.24: Hall Effect composition…………………………………………………. 55
FigII.25: The contacts on the sample to measure V_H………………………………… 55
FigII.26: $\Delta V_H = f(B)$ graph……………………………………………………. 56
FigII.27: The Hall Effect apparatus………………………………………………….. 57

FigIII.1: X-ray diffraction spectra of ZnO thin films deposited at different solution… molarities. 62
FigIII.2: The variation of the texture coefficient TC(hkl) of (100), (002), (101) and… (102) peaks related to the solution molarity. 63
FigIII.3: The variation of grain size as a function of solution molarity related to…. (100) and (002) planes. 64
FigIII.4: The evolution of stress and (002) peak position shift against the solution… molarity. 65
Fig III.5: The variation of film thickness of ZnO thin films deposited at different solution… molarities. 66
FigIII.6: (a and b) Scanning electron micrographs of ZnO thin films grown at…… 0,1 (mol.l^{-1}) solution molarity. 67
FigIII.7: Transmission spectra of ZnO thin films for different solution molarity…….. 68
FigIII.8: The plot $(ahv)^2$ versus (hv) for the calculate the optical band gap energy E_g.. 69
FigIII.9: The variation of the optical band gap Eg and Urbach energy Eu with…. solution molarity, 69
FigIII.10: The Variation of electrical conductivity σ of ZnO thin films with…… solution molarity. 70
FigIII.11: XRD patterns of undoped ZnO and Al-doped ZnO with various……….. Al doping rates. 72
FigIII.12: The variation of the texture coefficient TC(hkl) of (100), (002) and (101)... peaks with Al doping rate of ZnO thin films. 74
FigIII.13: a–c Idealized crystal habits of different ZnO structures; d–j projections….. of the crystallographic planes within the wurtzite structure; k, l scheme of the possible substitutional and interstitial sites to incorporate Al^{3+} ions. 75
FigIII.14: The variation of grain size of ZnO doped Al thin films…………………… 77
FigIII.15: The variation of stress and peak position shift of ZnO doped with…….. different Al concentrations. 78
FigIII.16: Thickness variation of ZnO doped Al thin films………………..……... 80

FigIII.17: SEM surface and cross section micrographs of Al-doped ZnO………. films prepared with various doping rates (a and b) undoped ZnO, (c, d, e, f and g) present Al concentration 1, 2, 3, 4 and 5 at % respectively. 84
FigIII.18: SEM surface Micrograph of our films Al-doped ZnO at 3 at % (a), ……… (b) AL-doped ZnO (0.5 %) deposited by spray pyrolysis method, (c) Al-doped ZnO (2,5 at %)ultrasonic spray pyrolysis. 81
FigIII.19: Energy X-ray Dispersive Spectroscopy spectra of four samples……….. of ZnO doped Al at 2, 3 and 5 at %. 82
FigIII.20: Variation of the transmittance of the ZnO films doped with Al depending... on the wavelength. 83
FigIII.21: The variation of optical band gap and Urbach energy of ZnO doped with… different Al concentrations. 84
FigIII.22: The variation of electrical conductivity with atomic doping rate……….. of aluminium. 86
FigIII.23: X-ray diffraction analysis (XRD) of ZnO doped Indium………………….. 89
FigIII.24: The variation of the texture coefficient TC(hkl) of In-doped ZnO … according of (100), (002) and (101) peaks. 90
FigIII.25: Variation of crystallite size of ZnO thin films as a function of indium… doping rate. 91
FigIII.26: Variation of stresses and (002) peak shift of the In-doped ZnO thin films… 92
FigIII.27: The variation of film thickness of ZnO doped In thin films……………… 94
FigIII.28: Transmittance variation of In-doped ZnO thin films according to….. the wavelength. 95
FigIII.29: The optical band gap Eg and Urbach energy Eu variations as a function…. of In-doping rate. 96
FigIII.30: The variation of electrical conductivity of ZnO doped at different……… In concentrations. 97

FigIV.1: X-ray diffraction (XRD) patterns of ZnO films deposited with various… substrate temperatures at 1.5 bar as carrier gas pressure. 105
FigIV.2: The grain size variation of ZnO films with substrate temperature deposited at 1.5 bar. 106
FigIV.3: The variation of stress and peak shift as a function of substrate temperature.. at 1.5 bar. 108
FigIV.4: The thickness variation of undoped ZnO thin films deposited at…… different substrate temperatures. 109
FigIV.5: Transmittance versus wavelength of ZnO thin films grown at…….. different substrate temperatures with pressure of 1,5 bar. 110
FigIV.6: band gap and Urbach energy of undoped ZnO thin films grown at…….. different substrate temperatures with pressure of 1.5 bar. 111
FigIV.7: The variation of electrical conductivity and resistivity of undoped…….. ZnO films deposited at 1 bar. 113
FigIV.8: X-ray diffraction (XRD) patterns of ZnO films deposited with……… various substrate temperatures at pressure of 1 bar. 114

FigIV.9: The grain size variation of ZnO films deposited at 1 bar, according……… to (002) peak, with different substrate temperatures. 115
FigIV.10: The variation of stress and peak shift as a function of substrate……… temperature at pressure of 1 bar. 117
FigIV.11: The thickness variation of undoped ZnO thin films deposited at……… different substrate temperatures. 118
FigIV.12: Transmittance versus wavelength of ZnO thin films grown at……… different substrate temperatures at pressure of 1 bar. 119
FigIV.13: band gap and Urbach energy of undoped ZnO thin films grown at……… different substrate temperatures at pressure of 1 bar. 120
FigIV.14: The variation of electrical conductivity and resistivity of undoped……. ZnO films deposited at 1 bar. 121
FigIV.15: XRD patterns of undoped ZnO and Al-doped ZnO with various Al…… doping rates, at air pressure of 1 bar and 400°C substrate temperature. 124
FigIV.16: The variation of (002) peak position and intensity of undoped and doped… ZnO deposited with various doping rates at 1 bar. 125
FigIV.17: Grain size of Al-doped ZnO films according to (002) diffraction peak, in... dependence of the aluminium doping rates deposited at 1 bar and 400°C. 126
FigIV.18: The variation of the stress and peak shift as a function of aluminium…. doping rates at 1 bar as air pressure and 400°C substrate temperature. 127
FigIV.19: The variation of Al-doped ZnO thin films thickness deposited at……… different doping rates. 129
FigIV.20: Transmittance versus wavelength of Al-doped ZnO thin films grown……. with different doping rates at 1 bar air pressure and 400°C substrate temperature. 130
FigIV.21: band gap and Urbach energy of Al-doped ZnO thin films grown…….. with different doping rates. 131
FigIV.22: The variation of electrical conductivity and resistivity of Al-doped……… ZnO films deposited at 1 bar and 400°C. 132

General Introduction

TCOs are materials which combine optical transparency with electrical conductivity. In order for materials to be transparent they must display a band gap greater than the highest frequency of visible light (3.1 eV). Metals for instance are highly conductive but do not transmit visible light and transparent materials such as glasses are insulators. TCOs exhibit intrinsic conductivity due to defect states in the crystal structure [1].

It has been known for some time that ZnO can be prepared as a transparent conducting film. ZnO has been commonly used in its polycrystalline form for over a hundred years in a wide range of applications: facial powders, ointments, sunscreens, catalysts, lubricant additives, paint pigmentation, piezoelectric transducers, varistors, and as transparent conducting electrodes [2].

To prepare zinc oxide as a thin film many methods can be used; Such as spray pyrolysis, sputtering, sol-gel, pulsed laser deposition (PLD), chemical vapor deposition (CVD) [3]; Among this methods spray pyrolysis are considered that a cheap and efficient method [4].

The objective of this work was to deposit undoped and doped ZnO thin films by spray pyrolysis; in fact two types (two atomization modes) of this method were used, ultrasonic and pneumatic spray pyrolysis; at a wide range of preparation conditions. In order to understand the growth behavior of ZnO thin films, preparation conditions effects on ZnO thin films properties and to establish the optimum growth procedure to get a thin film has extremely well structural, electrical and optical properties.

Various techniques were employed to characterize the films and thus determine the optimum growth conditions (i.e measurement of film thickness, resistivity, X-ray diffraction, Scanning electron microscopy and UV-Visible Spectrophotometry).

This thesis consists of four chapters. The first Chapter presents a review of the properties of ZnO and growth techniques. Chapter two presents a general description of spray pyrolysis, description of the experimental spray pyrolysis kit and its method of use, presents the growth conditions of undoped and doped ZnO thin films and the characterization techniques employed on the films are also described.

The third chapter presents the characterization results of Zinc oxide thin films doped with different elements which are Indium and Aluminium; where the aim is for finding out the effect of doping rate on the ZnO characteristics; the films were synthesized by ultrasonic spray pyrolysis technique; in line with this the results have get enough interpretation and discussion.

The fourth chapter is divided into two parts: the first presents the characterization results of undoped Zinc oxide thin films prepared using pneumatic spray pyrolysis technique and an interpretation of the impact of different substrate temperatures (from 300 to 450 °C) at two deposition spray pressures (1 and 1.5 bar). The second part presents the study of the Aluminium doping effect on the zinc oxide thin films properties using the same spray method.

We conclude our thesis by a general conclusion, a discussion, some final comments and suggestions for further work.

References

[01] D. S. Bhachu, the synthesis and characterization of metal oxide thin films, doctoral thesis, UCL (University College London), 2013.

[02] C. Jagadish and S. Pearton, Zinc Oxide Bulk Thin Films and Nanostructures, book published by Elsevier Science, 1st Edition, 2006.

[03] S. Ilican, Y. Caglar, M. Caglar, Journal Of Optoelectronics And Advanced Materials, 10 (2008) 2578-2583.

[04] A. J. C. Fiddes, Deposition of zinc oxide by spray pyrolysis, doctoral thesis, Durham University, 1993.

Chapter I:

Review of the Zinc Oxide Thin Films Properties and Growth techniques.

I.1.*Introduction:*

The growth and characterization of II-VI semiconductor, such as ZnO, has been becoming a more and more active research field in recent years. The research works have been encouraged by both scientific significance and the potential of various practical applications such as light-emitting diode (LEDs) and ultraviolet photodetector, V-blue semiconductor laser, flat panel displays, solar cell, gas sensor, and surface acoustic wave devices, and so on [1].

I.2.*Chapter Objectives:*

The objectives of this chapter are to:

1. Review the properties of zinc oxide.
2. Describe the applications of ZnO.
3. Summarize the different growth techniques of ZnO thin films.

I.3.*Transparent conducting oxides:*

TCOs are very useful materials to transparent optoelectronics because they have unique features of optical properties in the visible light region such as the transparency over ~85% and optical band gap greater than 3 eV and controllable electrical conductivity such as carrier concentrations of at least 10^{20} cm^{-3} and resistivity of about 10^{-4} $\Omega\cdot cm$.

I.3.1.*Definition:*

Transparent conducting oxides (TCOs) are electrical conductive materials with comparably low absorption of electromagnetic waves within the visible region of the spectrum [2].

I.3.2.*TCOs in General:*

In transparent conducting oxides (TCOs), the nonmetal part, B, consists of oxygen. In combination with different metals or metal-combinations, A, they lead to compound semiconductors, A_yB_z, with different opto-electrical characteristics. These opto-electrical characteristics can be changed by doping, A_yB_z:D (D = dopant), with metals, metalloids or nonmetals. Hence, metals can be part of the compound semiconductor itself, A, or can be a dopant, D.

The first transparent conductive oxide (TCO) thin film was reported by Badeker [3] in 1907, about 100 years ago. This first TCO was a thin film of CdO (Cadmium Oxide) prepared by

thermally oxidizing a vacuum sputtered film of cadmium metal. While CdO is not widely used today because of toxicity concerns, it remains of theoretical interest because of its high electron mobility apparently due to a low effective electron mass.

The first 50 years following the discovery of CdO saw little practical development of TCO until the 1940s when a chemical deposition method (pyrolysis) for TO (Tin Oxide), SnO_2, from $SnCl_4$ was developed. Transparent conductive IO (indium oxide) also was made by chemical deposition (pyrolysis) from $InCl_4$.

During the second 50 years after its discovery, TCO films have undergone very significant development and are “seen” by most of us virtually every day in applications ranging from digital watches to computer screens or other types of displays [3].

TCOs have been used in several applications for three or four decades but, despite the huge volume of experience in the field, there remain many unanswered questions at both applied and fundamental levels [4].

I.4.*History of Zinc oxide (ZnO) research:*

ZnO is not “a new semiconductor”. It has a long history of studies of its growth techniques and characterization of its material properties, has been investigated already in 1912. With the beginning of semiconductors age after the invention of the transistor, lattice parameters of ZnO are known from 1935, whereas detailed values of optical parameters were available in mid 50s. Systematic investigations of ZnO as a compound semiconductor were performed in 1960.

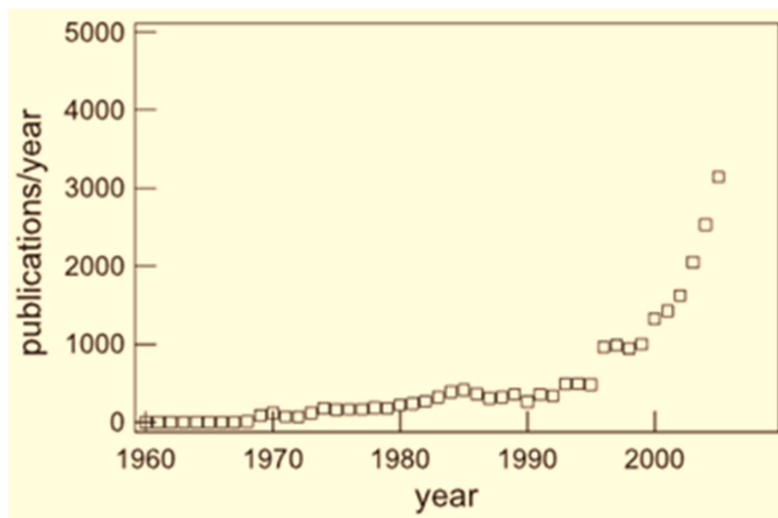

FigI.1: increase of the number of publications about zinc oxide according to the literature data base SCOPUS [7].

Currently, research on ZnO as a semiconducting material sees a renaissance after intensive research periods in the 1950s and 1970s. Even though good quality thin films (by chemical vapour deposition) were prepared in 1970, only recently ZnO attracts an increasing attention. Since about 1990 an increase of the number of publications on ZnO occurred (see FigI.1) and more recent reviews on ZnO have been published [5, 6, 7].

I.5.*ZnO choice:*

Most of the recent interests on ZnO material have been focused on the future potentials of UV-blue light emitting devices (LED) and UV-blue lasers [1].

The most desirable features of ZnO can be listed as follows [1, 7, 8, 9]:

1. ZnO has the extremely large exciton binding energy of 60 meV which is much greater than the thermal energy (26 meV) at room temperature. This is one of the key parameters that enable the UV laser diode and other exciton related light emitting devices to be 2 operated at room temperature.
2. High transparency in the visible and near infrared spectral region
3. ZnO is one of the “hardest” materials in II-VI compound semiconductors due to the higher melting point and larger cohesive energy. It can be expected that a degradation of the material due to the generation of dislocations during the device operation will be reduced.
4. Low material costs, nontoxicity, And abundance in the earth crust.
5. Interfacial energy between ZnO and sapphire or other oxide substrates is such that two-dimensional growth is favored, which results in high quality films at lower temperature.
6. Possibility to prepare highly doped films with free electron density $n>10^{20}$ cm^{-1} and low resistivity ($<10^{-3}$ Ω cm).
7. Good contact to the active semiconductors (absorber layers)
8. Possibility to prepare the TCO layer on large areas (>1 m^2) by deposition methods like magnetron sputtering
9. Possibility to prepare ZnO films with suitable properties at low substrate temperature.

I.6.*Properties of Zinc Oxide:*

ZnO is an oxide compound naturally occurring as rare mineral zincite, which crystallizes in the hexagonal wurtzite structure $P6_3mc$. Zincite is usually colored red or orange by manganese impurities. Photographs of zincite are shown in FigI.2 [7].

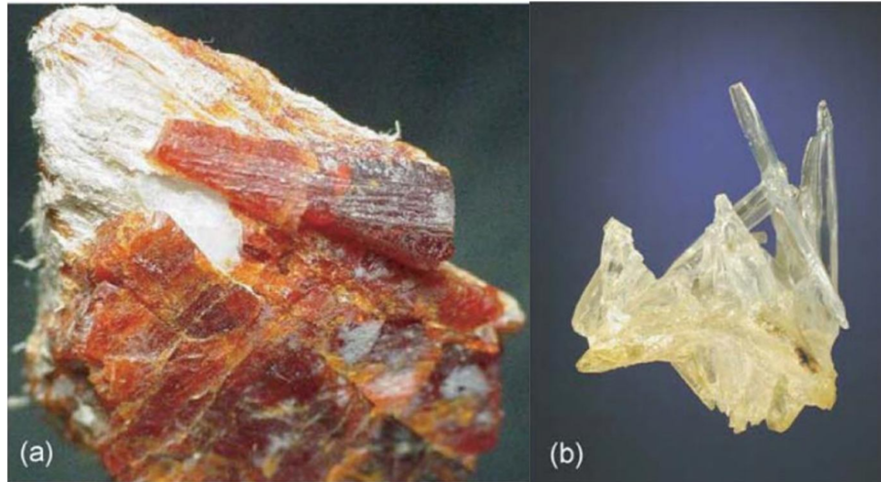

FigI.2: (a) An orange zincite crystal, (b) a synthetic zinc oxide crystal. The mineral in (a) exhibits a size of 30×25×6 mm^3.

I.6.1.*Crystal Structure:*

ZnO is a II-VI compound semiconductor and have crystal structures of wurtzite, zinc blend and rock salt. These structures are shown in FigI.3 [10].

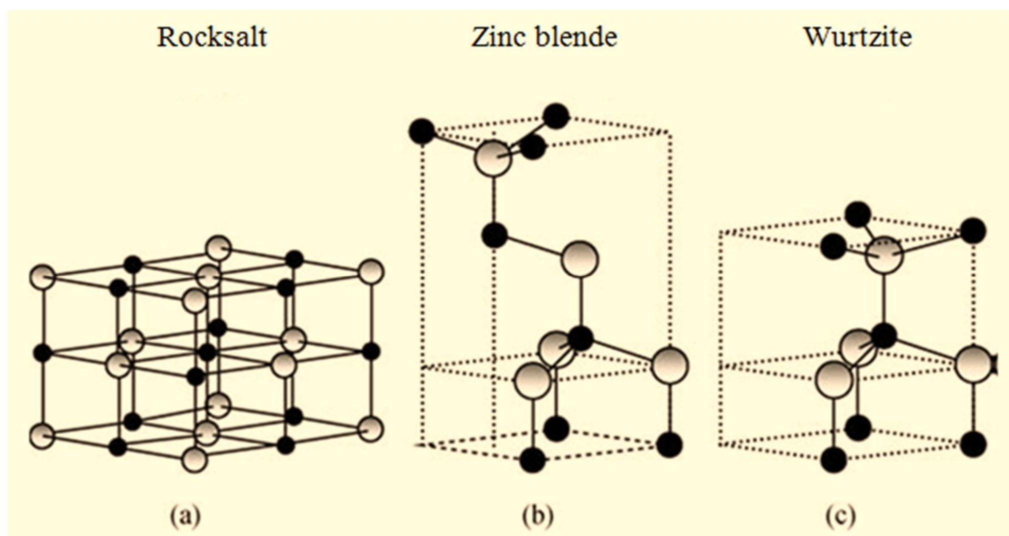

FigI.3: Crystal structures of ZnO (a) rocksalt (b) zinc blend and (c) wurtzite hexagonal. Shaded gray and black spheres denote Zn and O atoms, respectively.

The wurtzite crystal structure is the most stable structure of ZnO and it has also been found theoretically that this crystal structure is energetically favorable compared to the rocksalt and zinc blend structures [9]. These structures from different angles are shown in FigI.4.

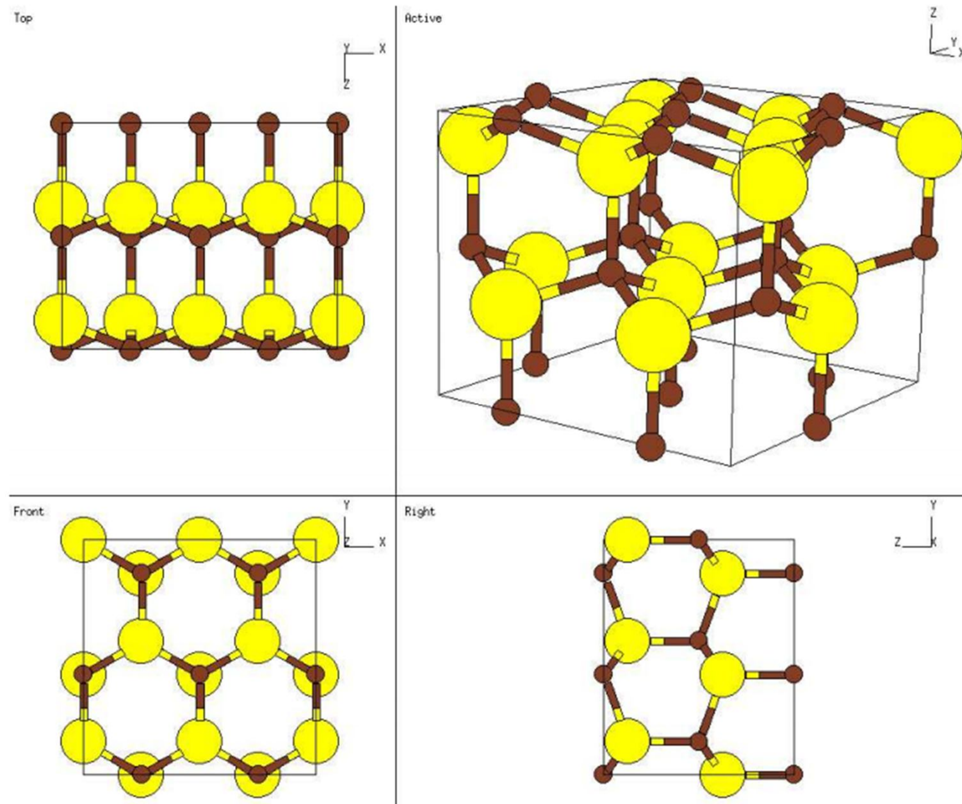

FigI.4: Wurtzite ZnO crystal structures from different angles.

The wurtzite structure has a hexagonal unit cell with two lattice parameters a and c with (a = 0.3296 and c = 0.520 65 nm [11]) in the ratio of $\frac{c}{a} = \sqrt{8/3} = 1.633$ (in an ideal wurtzite structure) [12]. It is characterized by two interconnecting sublattices of Zn^{2+} and O^{2-}, such that each Zn ion is surrounded by tetrahedra of O ions, and vice-versa. This tetrahedral coordination gives rise to polar symmetry along the hexagonal axis. This polarity is responsible for a number of the properties of ZnO, including its piezoelectricity and spontaneous polarization, and is also a key factor in crystal growth, etching and defect generation [13]. Various physical properties of the hexagonal structure of zinc oxide are summarized in Tab I.1.

Tab I.1: Physical properties of the zinc oxide in the wurtzite form [5, 14, 15, 16].

Property	Value
Lattice constants (T = 300 K) a_0 c_0 c_0/a_0	 0.32495 nm 0.52069 nm 1,602 (1,633 in an ideal wurtzite structure)
Density	5.606 g/cm^3
stable structure (T = 300 K)	wurtzite
Melting point	2248 K
Relative dielectric constant	8.66
Refractive index	2,008-2,029
Gap Energy	3.4 eV, direct
Intrinsic carrier concentration	< 106 cm^{-3}
Exciton binding Energy	60 meV
Electron effective mass	0.24
Electron mobility (T = 300 K)	200 cm^2/V.s
Hole effective mass	0.59
Hole mobility (T = 300 K)	5-50 cm^2/V.s

I.6.2.*Electronic band structure of ZnO:*

As a direct band gap semiconductor with wurtzite symmetry, the valence band (VB) of ZnO is split into the three branches of A, B and C jointly by the hexagonal crystal field Δcr and spin orbit interaction Δso (see FigI.5). At low temperature, the gaps are:

$$E_g^A = 3{,}437eV;\ E_g^B = 3{,}442eV;\ E_g^C = 3{,}481eV, \text{ respectively [8].}$$

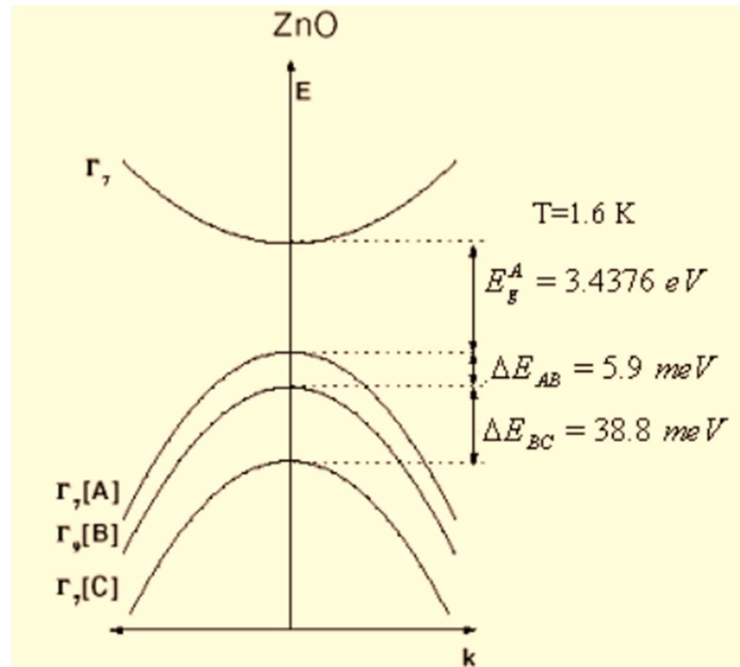

FigI.5: Band structure and symmetries of hexagonal ZnO. The splitting into the three valence bands (A, B, C) is jointly caused by the crystal field and spin-orbit splittings [13].

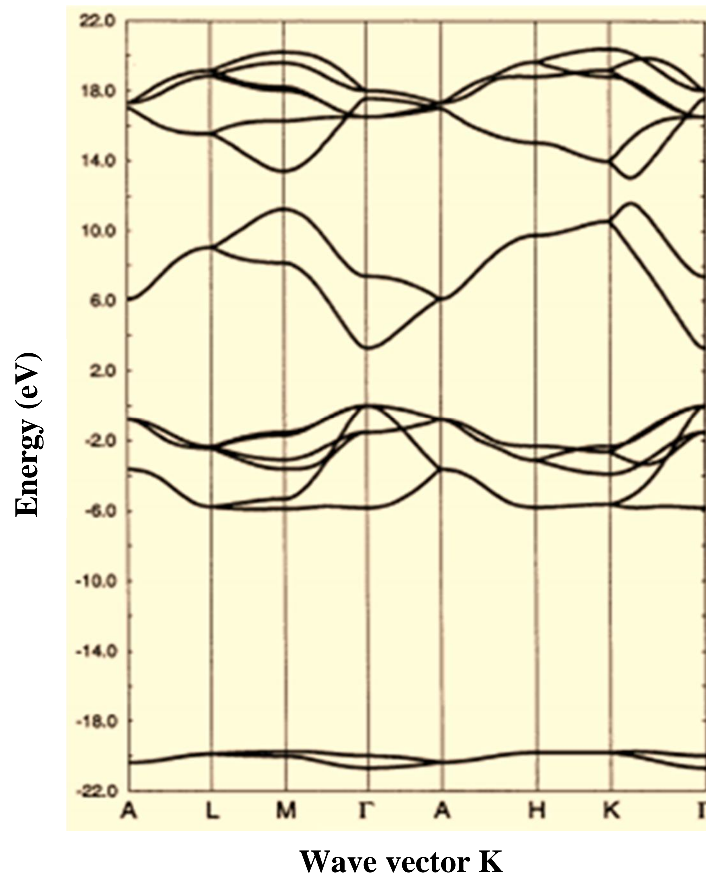

FigI.6: The Bulk band structure of the ZnO crystal.

FigI.6 shows the band structure for the ZnO crystal. The points denoted by F, K, M, A, H, L are high symmetry points in the Brillouin zone. The wave vectors used to calculate the band structure shown in FigI.6 is k vectors along the line A→L→M→Γ→A→H→K→Γ in the Brillouin zone. The narrow lowest valence band near ~ 20eV corresponds to an atomic-like oxygen 2s state, the upper valence bands are mainly derived from the oxygen 2p state with a sizable mixture of Zn 4s and 4p states. The lowest conduction band is composed primarily of Zn 4s states [17].

I.7.*Doping of ZnO:*

To realize any type of device technology, it is important to have control over the concentration of intentionally introduced impurities, called dopants, which are responsible for the electrical properties of ZnO.

ZnO is a direct band gap semiconductor with Eg = 3.4 eV. The band gap of ZnO can be tuned via divalent substitution on the cation site to produce heterostructures [18]. This band gap can be tuned in a range between 3.0 to 4.0 eV by doping with metals such as Cd and Mg [19].

The main problem for the application of ZnO as a material for electro-optic devices is ambipolar doping. This problem is found frequently for wide band gap materials, namely that doping of one type (n-type) is easily possible up to high densities, while the opposite type (p-type) is hardly achievable. The semiconductors ZnO is generally n-type [16].

Temperature-dependent Hall measurements have shown that zinc interstitials (Zni) are one of the three principal donor types in bulk ZnO crystals. Recent reports have shown that the Zni-NO complex (with a 0.9eV binding energy) could be the most abundant donor in ZnO. This complex forms because zinc interstitials are mobile at room temperature and likely have to form complexes in order to become stable. The oxygen vacancies are the most abundant donors in ZnO, though neither zinc interstitials nor oxygen vacancies exhibit characteristics consistent with the high electron concentrations observed in undoped ZnO [20].

The attainment of intentional n-type doping of ZnO is relatively easy compared to p-type doping. As n-type dopants, group III elements B [21], Al [22], Ga [23] and In [24], rare earth metals (group IIIB), group IV elements Si [25], Ge [26], and Sn [27], and group VII elements can be used.

Group III elements Al, Ga, and In as substitutional elements for Zn are probably more suitable for n-type doping of ZnO due to their lower vapor pressures compared to group VII elements such as Cl, Br, and I substituting for O [16].

I.8.*ZnO thin films applications:*

Zinc oxide can be called a multifunctional material thanks to its unique physical and chemical properties. It is already widely used in our society, and indeed it is a key element in many industrial manufacturing processes, we are now moving into an era where ZnO devices will become increasingly functional and exotic [13]. The FigI.7 represents a schematic of the ZnO application [28].

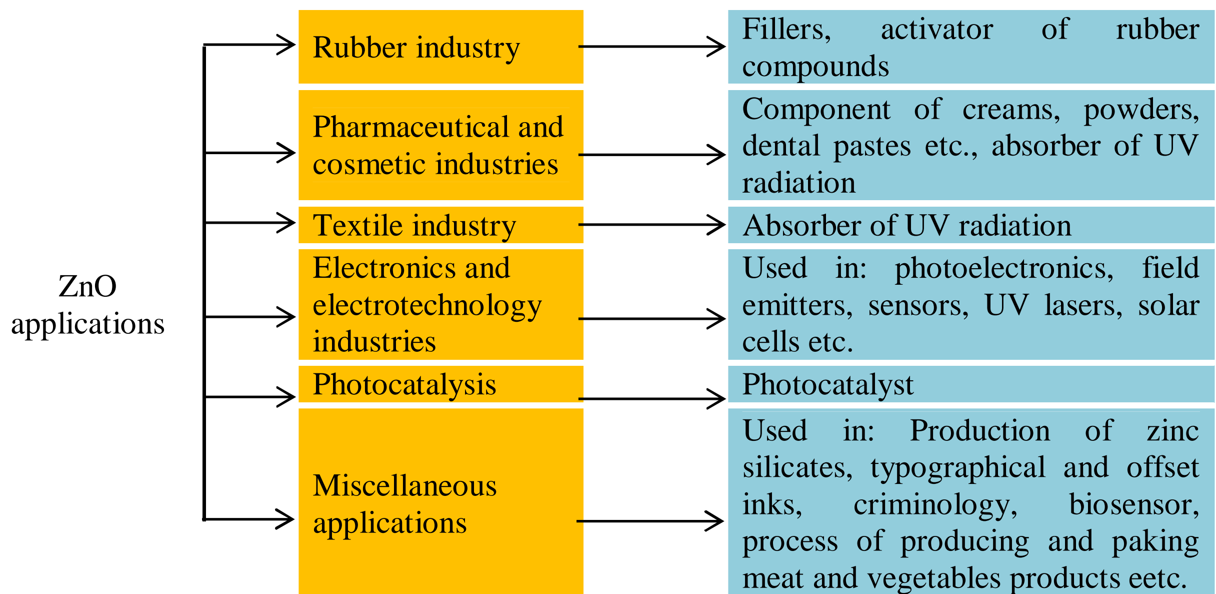

FigI.7: Schematic representation the applications of ZnO.

Zinc oxide as cream used for preventing and treating diaper rash. It can also be used to treat minor skin irritations [29].

Doped and undoped ZnO thin films have widely been used for liquid crystal displays, electronic and optoelectronic devices, transparent conducting materials and other applications [30].

ZnO have attracted significant attention towards gas sensing due to their simple implementation, low cost, and good reliability for real-time control systems with respect to other gas sensors [19].

The variety of structures of nanometric zinc oxide means that ZnO can be classified among new materials with potential applications. Zinc oxide can occur in one (1D), two (2D), and three dimensional (3D) structures. One dimensional structure make up the largest group, including nanorods, needles, helixes, springs and rings, ribbons, tubes and combs. Zinc oxide can be obtained in 2D structures, such as nanoplate/nanosheet and nanopellets. Examples of 3D structures of zinc oxide include flower, dandelion, snowflakes, coniferous urchin-like, etc [28].

Thus ZnO Mentioned applications (are a tip of the ice-berg) have enormous opportunities for society and industry alike due to its unique properties which are now being explored and applied. The future in which ZnO devices become part of our everyday lives is already approaching reality.

I.8.1. *ZnO thin films for photovoltaics:*

One of the highly attractive features of ZnO is that it can be deposited using a variety of different techniques, many of which are low cost, and it can grow in a large variety of nanostructured morphologies. Thus, ZnO has large variety of applications, including applications in optoelectronic devices such as solar cells. Where, several types of photovoltaic cells have been produced by combining ZnO with semiconductors.

Noting that, in the undoped state, ZnO is highly resistive because zinc oxide native point defects are not efficient donors. However, reasonable impurity doping efficiencies can be achieved through substitutional doping with Al, In, or Ga [31].

The simplest application of ZnO-based materials in photovoltaic is antireflection and/or light-trapping coatings and contacts. For applications as transparent contacts in solar cells, doping with group III elements is usual. Whereas, doped ZnO electrodes are commonly used both as contacts and to enhance light trapping in thin film solar cells via textured electrode surface. The majority of the works of ZnO-based electrodes have been reported for inorganic solar cells [32].

A CIGS (Copper Indium Gallium Selenide) cell is shown in FigI.8 [31]. The requirements for the top TCO contact in CIGS cells are both demanding and unique to this technology. Typically the TCO used in these applications has been Al doped ZnO.

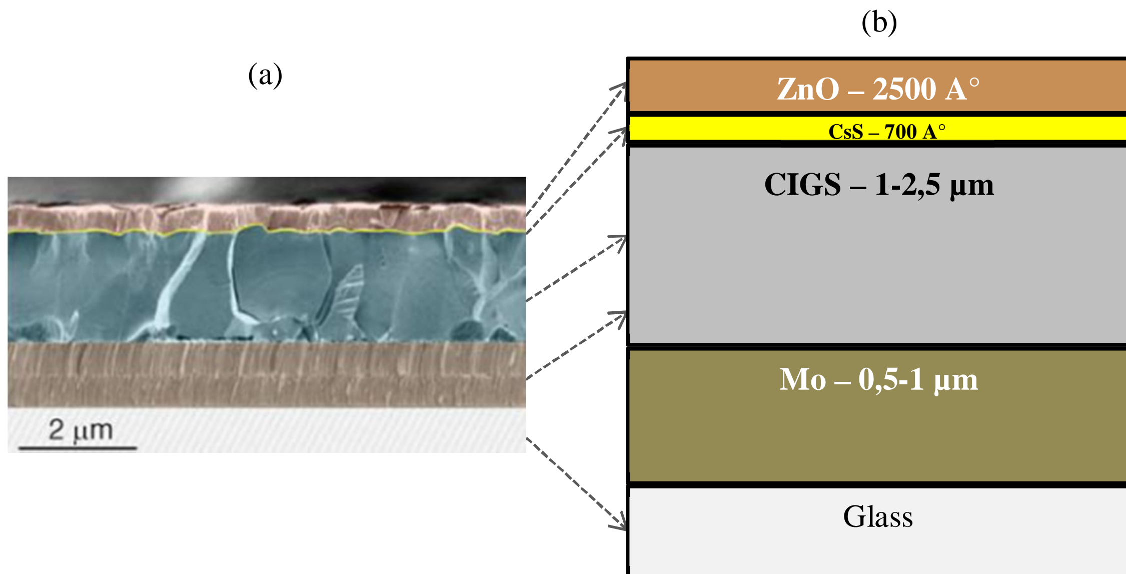

FigI.8: Actual photovoltaic structures: (a) CIGS seen in cross section using SEM. (b) Schematic illustrations of the structures.

I.9.*Different growth techniques of ZnO:*

ZnO thin films have been prepared by a variety of thin films deposition techniques, which can be divided into two groups based on the nature of the deposition process viz., physical or chemical.

The physical methods include physical vapour deposition (PVD), laser ablation, molecular beam epitaxy, and sputtering. The chemical methods comprise gas-phase deposition methods and solution techniques (FigI.9) [33]. The aim of any deposition technique is the preparation of thin films in reproducible, controllable and predictive ways [34].

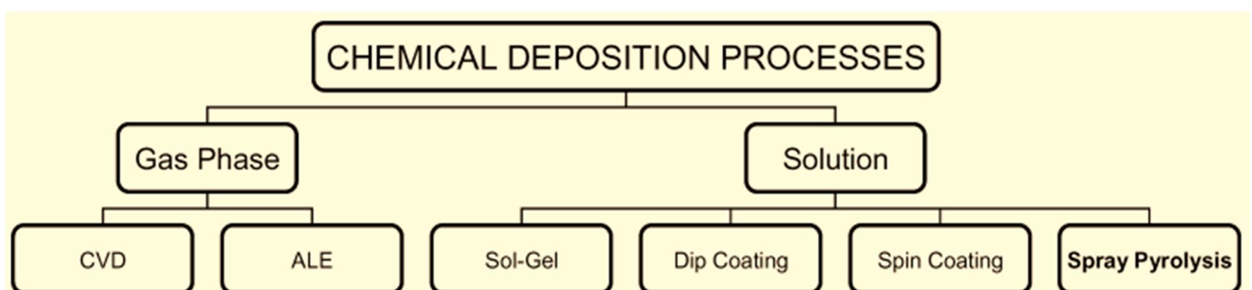

FigI.9: Chemical thin film deposition methods.

A classification scheme is presented in Table I.2 where we have grouped thin-film deposition technologies according to evaporative glow discharge, gas-phase chemical, and liquid-phase chemical processes [35].

Table I.2: Survey and classification of thin-film deposition technologies.

Evaporative Methods	
• Vacuum Evaporation	
Conventional vacuum evaporation Electron-beam evaporation	Molecular-beam epitaxy (MBE) Reactive evaporation
Glow-Discharge processes	
• Sputtering	**• Plasma Processes**
Diode sputtering Reactive sputtering Bias sputtering (ion plating) Magnetron sputtering Ion beam deposition Ion beam sputter deposition Reactive ion plating Cluster beam deposition (CBD)	Plasma-enhanced CVD Plasma oxidation Plasma anodization Plasma polymerization Plasma nitridation Plasma reduction Microwave ECR plasma CVD Cathodic arc deposition
GAS-PHASE CHEMICAL PROCESSES	
• Chemical Vapor Deposition (CVD)	**• Thermal Forming Processes**
CVD epitaxy Atmospheric-pressure CVD (APCVD) Low-pressure CVD (LPCVD) Metalorgainc CVD (MOCVD) Photo-enhanced CVD (PHCVD) Laser-induced CVD (PCVD) Electron-enhanced CVD	Thermal oxidation Thermal nitridation Thermal polymerization Ion implantation
LIQUID-PHASE CHEMICAL TECHNIQUES	
• Electro Processes	**• Mechanical Techniques**
Electroplating Electroless plating Electrolytic anodization Chemical reduction plating Chemical displacement plating Electrophoretic deposition	Spray pyrolysis Spray-on techniques Spin-on techniques Liquid phase epitaxy

I.9.1.*Chemical Vapour deposition:*

The chemical vapour deposition (CVD) technique uses gas phase sources to form thin films by chemical reactions on the substrate surface. When the source gases are introduced into the reaction chamber, they diffuse to the substrate surface where the thin film is formed by a chemical reaction between the various gas atoms and the substrate [36].

The key steps of CVD are shown in FigI.10, which include [37]:

Evaporation and transport of reagents in the bulk gas flow region into the reactor;

1. Mass transport of the reactants to the substrate surface;
2. Adsorption of the reactants on the substrate surface;
3. Surface diffusion to growth sites;
4. Nucleation and surface chemical reactions leading to film growth;
5. Desorption and mass transport of remaining fragments of the decomposition away from the reaction zone.

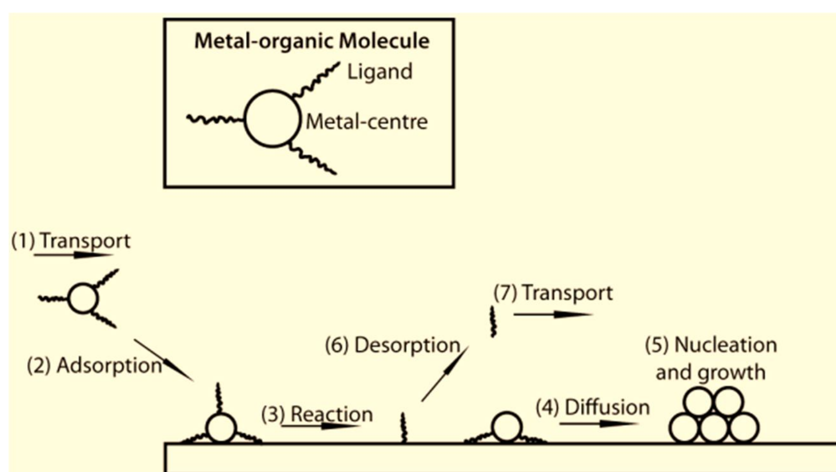

FigI.10: Schematic of the CVD process.

There are a wide range of techniques that fall under the CVD category and ultimately differ in one parameter [38]:

- Metal-organic chemical vapour deposition (MOCVD) is a specific type of CVD that utilizes metal-organic precursors.
- Metal-organic vapour phase epitaxy (MOVPE) or organometallic vapour phase epitaxy (OMVPE) is an MOCVD process that produces single crystal films on single crystal substrates from metal-organic precursors.

- Plasma-assisted or plasma-enhanced CVD (PECVD) is a technique in which electrical energy rather than thermal energy is used to initiate homogeneous reactions for the production of chemically active ions and radicals that can participate in heterogeneous reactions, which, in turn, lead to layer formation on the substrate.
- Atomic layer chemical vapour deposition (ALCVD), sometimes called atomic layer epitaxy (ALE), is a modification of the CVD process in which gaseous precursors are introduced sequentially to the substrate surface and the reactor is purged with an inert gas, or evacuated, between the precursor pulses.
- Chemical beam epitaxy (CBE) is high vacuum CVD technique that uses volatile metal-organic precursors and gaseous co-precursors.

I.9.2.*Physical Vapour Deposition:*

The term 'physical vapour deposition (PVD)' was first laid on paper by C.F. Powell, J.H. Oxley and J.M. Blocher Jr. in their 1966 book Vapour Deposition [39]. *Physical vapor deposition* (PVD) involves the generation of a vapor flux and its subsequent condensation in the form of a thin film on a substrate in a vacuum chamber [40].

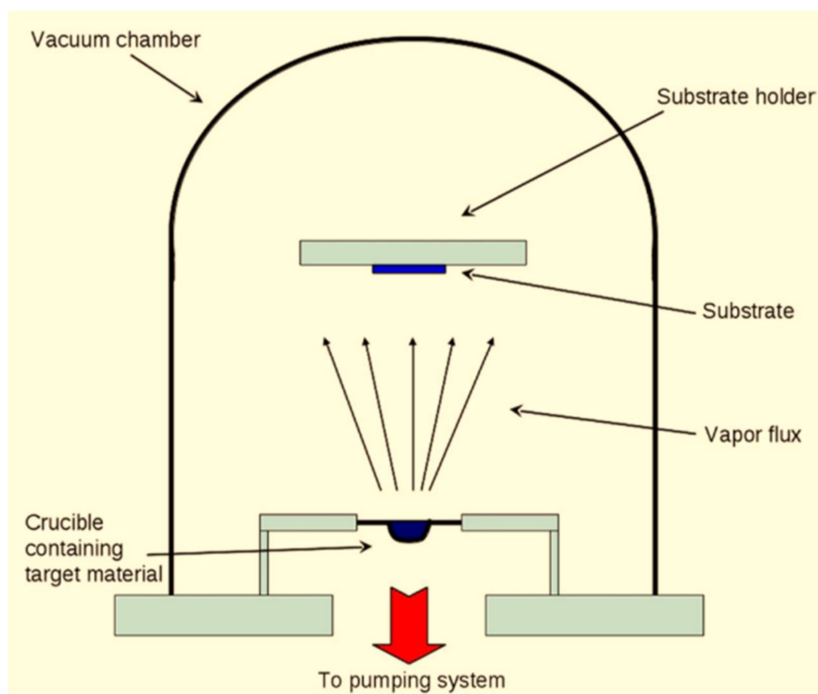

Fig I.11: Schematic of a typical thermal or electron-beam evaporation system. The source material is heated by an electrical current in thermal evaporation or by bombardment by an electron beam in electron-beam evaporation.

PVD techniques used in production are basically two in nature: thermal evaporation by resistively heating or by using an electron- beam heating, and sputtering, a no thermal process [41].

- The term PVD encompasses several techniques, including, [42]:
- Evaporative deposition-resistive heating is used to vaporize the material which is then allowed to deposit onto a substrate.
- Electron beam vapour deposition- a high energy beam of electrons bombards the sample material causing vaporization; Fig I.11 presents a schematic representation of an evaporation system.
- Sputter coating - involves the use a plasma discharge to vaporize the material.
- Pulsed laser deposition- a high energy laser pulse causes evaporation of the material.

I.9.3.*Radio frequency magnetron sputtering:*

Sputter deposition is a physical vapor deposition (PVD) method for depositing thin films, which is one of the most popular growth techniques due to its low cost, simplicity, large area, and low deposition temperature. Sputtering means to eject material from a target and then deposit it on the substrate [43].

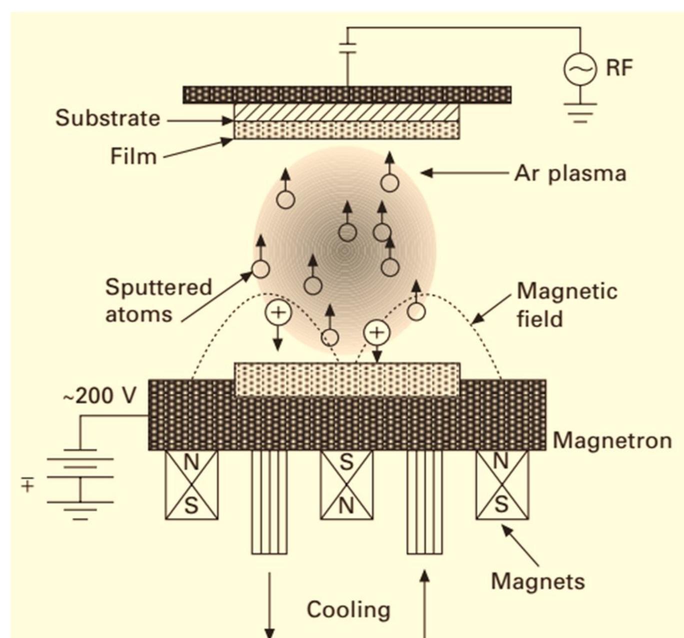

FigI.12: Schematic (not to scale) of rf (radio-frequency) magnetron sputtering.

In most forms of sputtering there is an electrical potential difference (can be of the order of 1500 v) between the target and the substrate, that (via generation of plasma) is the source of the high-energy ions. Sputtering is a complex process where the material in a solid target is vaporized by bombardment with high-energy ions (FigI.12). Where we can show the target species projected towards the substrate. the atoms of, e.g., Ar low-pressure gas are ionized in the chamber due to the large electric field and are excited to create a stable plasma. Magnets are used to control volume and position of the plasma. Water cooling is necessary as thermal energy is released upon collision of Ar+ ions with the target material, which could fracture due to an uneven temperature if left uncooled [34].

I.9.4.*Laser Ablation:*

In *laser ablation*, also called *pulsed laser deposition* (PLD), an intense, pulsed laser beam irradiates the target. When the laser pulse is absorbed by the target, its energy is used first for electronic excitation and then converted into thermal, chemical, and mechanical forms of energy, resulting in evaporation, ablation, plasma formation, and even exfoliation. The ejected material expands into the surrounding vacuum in the form of a plume containing many energetic species, including atoms, molecules, electrons, ions, clusters, particles, and molten globules. These diverse species finally condense onto a substrate as a thin film [40].

In PLD, show schematically in FigI.13, a pulsed laser is focused onto a target of the material to be deposited. For sufficiently high laser energy density, each laser pulse vaporizes or ablates a small amount of the material creating a plasma plume. The ablated material is ejected from the target in a highly forward-directed plume. The ablation plume provides the material flux for film growth.

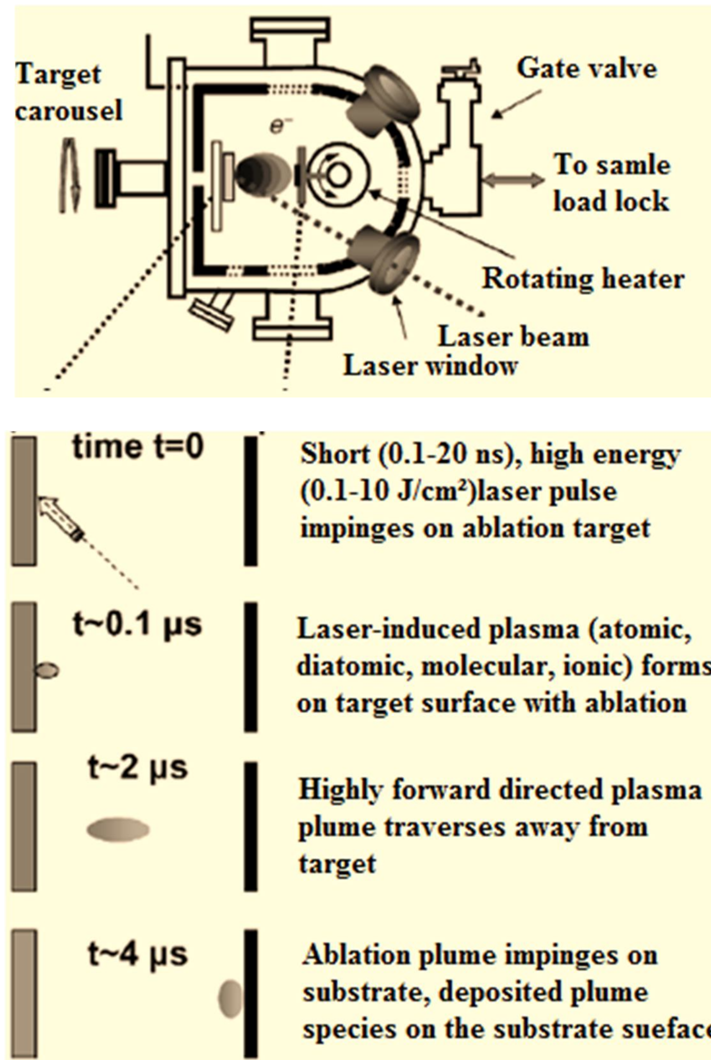

FigI.13: Schematic of the PLD process [44].

I.9.5.*Sol gel:*

Sol–gel method is widely used to obtain various kinds of functional oxide films, including ZnO and doped ZnO [45]. There are many benefits in comparison to other processes due to its simplicity and the low equipment costs. Other benefits lie in the good adherence between film and substrate, the easy controlling of doping levels and in the possibility to deposit the layers on complex shaped substrates [46]. The type of materials processed by this method covers metallic, inorganic, organic and hybrid materials. The use of the materials covered by this method ranges from highly advanced materials to materials for general use. The areas of technology covered by this method ranges from photonics to biology. These indicate that the sol-gel method can be applied to processing of an extremely many kinds of materials [47].

A **SOLS** is a stable suspension of colloidal solid particles within a liquid. A **GEL** is a porous three dimensionally interconnected solid network that expands in a stable fashion throughout a liquid medium and is only limited by the size of the container [48, 49].

A gel forms when the homogenous dispersion present in the initial sol rigidifies. This process, called gelation, prevents the development within the material. A sol can be transformed into a colloidal (or polymeric) gel by going through what is called a gel-point [48].

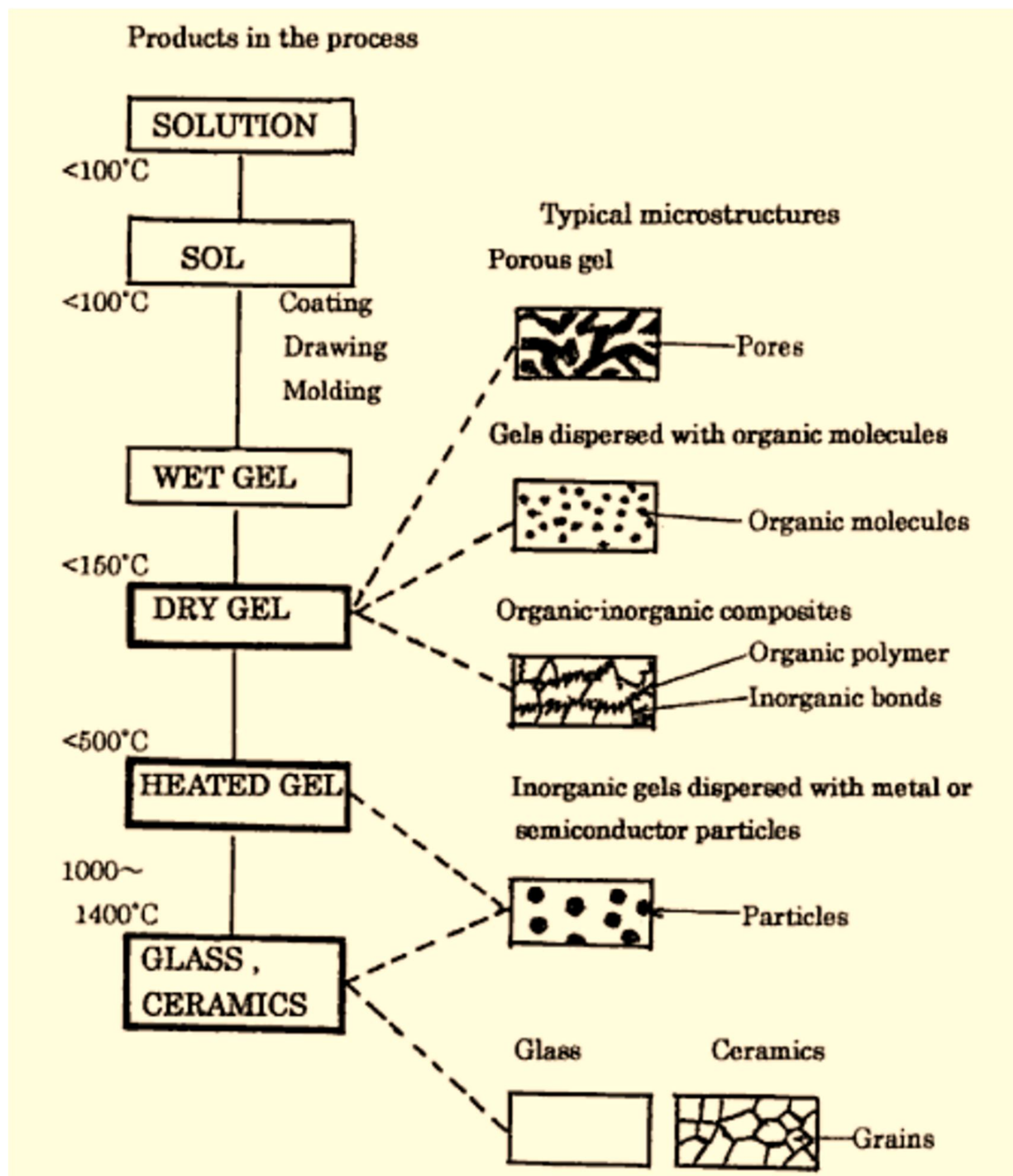

FigI.14: shows the steps of the sol-gel processing of materials and examples of the microstructures of final products. Bold-lined rectangles show possible final products of the sol-gel method.

FigI.14 shows the steps of the sol-gel processing of materials and examples of the microstructures of final products. The final products are the dried gel, the heated gel and the glass and ceramics [47]. The most widely used techniques for sol-gel are "spin-coating" and "dip-coating" (FigI.15).

Dip coating, or immersion coating, technique is the most commonly used technique in both academia and industry for many chemical and nanomaterial engineering research projects. The process normally refers to the immersing of a substrate into a tank containing coating material, withdrawn the piece from the tank under controlled speed, temperature and atmospheric conditions and finally allowing it to drain. The coated piece can be dried either by force-drying or baking [50, 51].

Spin coating is a simple process for rapidly depositing thin coatings onto relatively flat substrates. The substrate to be covered is held by some rotatable fixture (often using vacuum to c1amp the substrate in place) and the coating solution is dispensed onto the surface; the action of spinning causes the solution to spread out and leave behind a very uniform coating of the chosen material on the surface of the substrate [52].

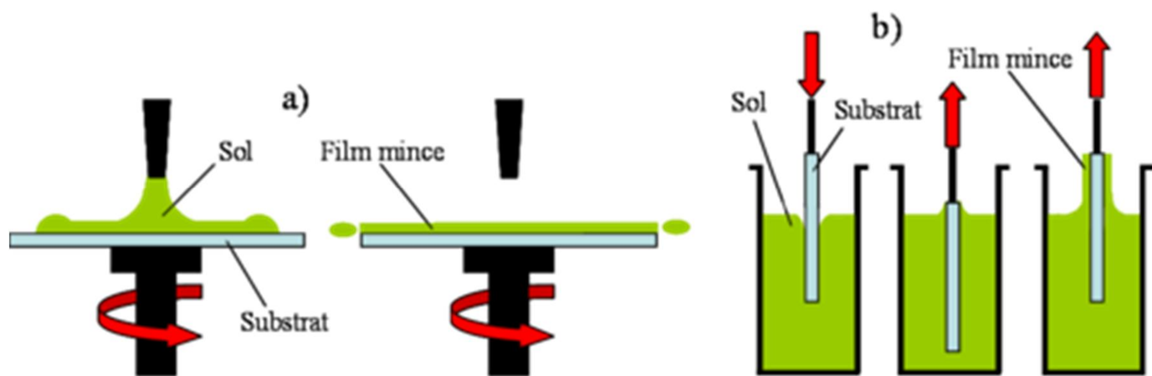

FigI.15: Schematic diagram of sol-gel, (a) spin-coating (b) dip-coating.

References:

[1] C. Jin, Growth and Characterization of ZnO and ZnO-Based Alloys_$Mg_xZn_{1-x}O$ and $Mn_xZn_{1-x}O$, doctoral thesis, North Carolina State University, 2003.

[2] A. Stadler, Materials, 5 (2012) 661-683.

[3] C. I. Bright, Review of Transparent Conductive Oxides, Society of Vacuum Coaters, (2007) 38-45.

[4] T. J. Coutts, T. O. Mason, J. D. Perkins, and D. S. Ginley, Transparent conducting oxides: status and opportunities in basic research, 34 (1999) 1-17.

[5] B. El Zein, Growth And Characterization Of Zno Nanostructures For Photovoltaic Applications, doctoral thesis, university of Lille 1 Sciences Et Technologies, 2012.

[6] A. Tomaszewska-Grzeda, W. Lojkowski, M. Godlewski, S. Yatsunenko, K. Drozdowicz-Tomsia, E.M. Goldys and M.R. Phillips, Acta Physica Polonica A, 108 (2005) 897-902.

[7] K. Ellmer, A. Klein, K. Ellmer, A. Klein, B. Rech, Transparent Conductive Zinc Oxide Basics and Applications in Thin Film Solar Cells, book published by Springer, 2008.

[8] S. Shenlei, Exciton Related Optical Properties Of ZnO, doctoral thesis, University of Hong Kong, 2006.

[9] A. Khan, Synthesis, Characterization And Luminescence Properties Of Zinc Oxide Nanostructures, doctoral thesis, Ohio University, 2006.

[10] S. Rahmane, Elaboration Et Caractérisation De Couches Minces Par Spray Pyrolyse Et Pulvérisation Magnétron, doctoral thesis, University of Mohamed Kheider Biskra, 2008.

[11] Z. L. Wang, Traitement de l’oxyde de zinc et étude de ses propriétés physicochimiques superficielles, Topical review, J. Phys.Condens. Matter, 16 (2004) 829–858.

[12] H. Morkoç and U. Ozgur, Zinc Oxide Fundamentals: Materials and Device Technology, book published by Wiley-VCH, 2009.

[13] C. Jagadish and S. Pearton, Zinc Oxide Bulk Thin Films and Nanostructures, book published by Elsevier, 1st Edition, 2006.

[14] C. Nadia, Traitement de l’oxyde de zinc et étude de ses propriétés physicochimiques superficielles, doctoral thesis, Badji MokhtarAnnaba University, 2014.

[15] Z. Fan and J. G. Lu, Zinc Oxide Nanostructures: Synthesis and Properties, Journal of Nanoscience and Nanotechnology, 5 (2005) 1561-1573.

[16] C. Klingshirn, ZnO: From basics towards applications, Review Article, phys. stat. sol, 244 (2007) 3027-3073.

[17] C. Yan, Electronic Structure and Optical Properties of ZnO: Bulk and Surface, doctoral thesis, Oregon State University, 1994.

[18] D. P. Norton, Y. W. Heo, M. P. Ivill, K. Ip, S. J. Pearton, M. F. Chisholm and T. Steiner, Elsevier, 7 (2004) 34-40.

[19] M. B. Rahmani, S. H. Keshmiri, M. Shafiei1, K. Latham, W. Wlodarski, J. du Plessis, and K. Kalantar-Zadeh, American Scientific Publisher, 7 (2009) 1-8.

[20] A. L. Allenic, Structural, Electrical And Optical Properties Of P-Type ZnO Epitaxial Films, doctoral thesis, University of Michigan, 2008.

[21] Q. Yua ,L. Jiang, S. Gao, S. Zhang, T. Ai, X. Feng, W. Wang, Ceramic International, 43 (2017) 2864-2866.

[22] K.M. Sandeep, S. Bhat and S.M. Dharmaprakash, Journal of Physical and Chemistry of Solids, 104 (2017) 36-44.

[23] L. Gong, Y. Liu, L. Jiang, F. Liuc, Materials Science in Semiconductor Processing, 66 (2017) 105-108.

[24] R. K.Chava, M. Kang, Journal of Alloys and Compounds, 692 (2017) 67-76.

[25] J. H. Kim, H-S. Im, D-W. Hwang, S-K.g Kim, D. Bae, Y-Z. Yoo, K-S. Lee, T-Y. Seong, Ceramic International, 43 (2017) 3693-3697.

[26] Y-b. Lv, Y. Dai, K. Yang, Z. Zhang, W. Wei, M. Guo, B. Huang, Physica B: Condensed Matter, 406 (2011) 3926-3930.

[27] V. Postica, M. Hoppe, J. Gröttrup, P. Hayes, V. Röbisch, D. Smazna, R. Adelung, B. Viana, P. Aschehoug, T. Pauporté, O. Lupan, Solid State Sciences, 71 (2017) 75-86.

[28] A. Kołodziejczak-Radzimska and T. Jesionowski, Zinc Oxide From Synthesis to Application: A Review, Materials, 7 (2014) 2833-2881.

[29] H. R. Godfrey, N. J. Godfrey, J. C. Godfrey, D. Riley, Alternative Therapies,7 (2001) 49-56.

[30] L. Castaneda, A. Garcia-Valenzuela, E.P. Zironi, J. Canetas-Ortega, M. Terrones, A. Maldonado, Thin Solid Films, 503 (2006) 212-218.

[31] E. Fortunato, D. Ginley, H. Hosono and D. C. Paine, MRS Bulletin, 32 (2007) 242-247.

[32] A. B. Djurišic, X. Liu, and Y. H. Leung, phys. Status Solidi RRL, 8 (2014) 123-132.

[33] D. P. Ludwig, J. Gauckler, Journal of Electroceramics, 14 (2005) 103-111.

[34] J. Orava, T. Kohoutek, T. Wagner, Deposition techniques for chalcogenide thin films, book published by Woodhead, 2014.

[35] K. Seshan, Thin-Film Deposition Processes And Techniques Principles, Methods, Equipment and Applications, book published by Noyes Publications, 2^{sec} Edition, 2002.

[36] N. D. Khan, An Investigation of the Performance and Stability of Zinc Oxide Thin-film Transistors and the Role of High-k Dielectrics, doctoral Thesis, Montfort University, 2010.

[37] D. S. Bhachu, the synthesis and characterization of metal oxide thin films, doctoral thesis, University College London, 2013.

[38] A. C. Jones And M. L. Hitchman, Chemical Vapour Deposition: Precursors, Processes and Applications, book published by springer, 2009.

[39] I. S. Abela, Physical vapour deposition on Mg alloys for biomedical applications,

Woodhead Publishing Series in Biomaterials, II (2015) 81-100.

[40] R. J. Martín-Palma and A. Lakhtakia, Vapor-Deposition Techniques, book published by Elsevier Inc (chapter 15), 2013.

[41] A. Moarrefzadeh, Wseas Transactions On Applied And Theoretical Mechanics, 7 (2012) 106-111.

[42] M. R. Waugh, The Synthesis, Characterization and Application of Transparent Conducting Thin Films, doctoral thesis, University College London, 2011.

[43] D. Wang, Fabrication and Characterization of ZnO Related Materials Thin Films for Optical Device Application, doctoral thesis, University of Technology Kochi Japan, 2012.

[44] R. Eason, Pulsed Laser Deposition Of Thin Films, book published by Wiley, 2007.

[45] A. Verma, F. Khan, D. Kumar, M. Kar, B.C. Chakravarty, S.N. Singh, M. Husain, Thin Solid Films, 518 (2010) 2649-2653.

[46] Y. H. Hwang, S-J. Seo and B-S. Bae, J. Mater. Res, 25 (2010) 695-700.

[47] S. Sakka, Handbook of Sol-Gel Science and Technology: application of sol-gel technology, book published by Springer US (volume III), 2015.

[48] A. C. Pierre, Introduction to Sol-Gel Processing, book published by Springer US, 1998.

[49] A. Caumont-Potdevin, Synthèse par voie sol-gel et caractérisation de matériaux luminescents nanostructures applicables dans une nouvelle génération de lampes propres, doctoral thesis, university of Blaise Pascal - Clermont Ferrand Ii, 2007.

[50] L.E. Scriven, Physics And Applications Of Dip Coating And Spin Coating, Article Review, j. Mater. Res., 121 (1998) 717-729.

[51] J. K. Kim, S. Thomas, P. Saha, Multicomponent Polymeric Materials, book published by Springer Media Dordrecht, 2016.

[52] M. A. Aegerter and M. Mennig, Sol-gel technologies for glass producers and users, book published by Springer Media New York, 2004.

Chapter II:

Growth process and characterization devices for ZnO thin films.

II.1.*Introduction:*

This chapter contains the experimental details of the deposition of undoped and doped zinc oxide, includes a description of the apparatus used and the deposition procedures.

The choice and preparation of substrates and precursor solutions are then described. Finally the techniques used to characterize ZnO thin films and the underlying principles are outlined together with a brief description of the equipment used and the practical aspects of applying the technique to ZnO.

II.2.*Chapter Objectives:*

The objectives of this chapter are to:

1. General Description of Spray pyrolysis.
2. Specify the experimental details to deposition process.
3. Select the different characterization methods of ZnO thin films.

II.3.*Experimental technique:*

II.3.1.*Spray pyrolysis technique:*

II.3.1.1.*General Description of Spray pyrolysis:*

Spray pyrolysis has been applied to deposit a wide variety of thin films. These films were used in various devices. It is observed that often the properties of deposited thin films depend on the preparation conditions.

Spray pyrolysis is a processing technique being considered in research to prepare thin and thick films, ceramic coatings, and powders. Unlike many other film deposition techniques, spray pyrolysis represents a very simple and relatively cost-effective processing method.

It offers an extremely easy technique for preparing films of any composition. Spray pyrolysis does not require high-quality substrates or chemicals. The method has been employed for the deposition of dense films, porous films, and for powder production. Even multilayered films can be easily prepared using this versatile technique. Spray pyrolysis has been used for several decades in the glass industry and in solar cell production [1, 2].

Typical spray pyrolysis equipment consists of an atomizer, precursor solution, substrate heater, and temperature controller. The following atomizers are usually used in spray pyrolysis technique: air blast, ultrasonic and electrostatic [3].

There are at least four types of spray guns available. They are the pneumatic, the airless, the pneumatic airless, and the ultrasonic.

In the pneumatic system atomization of the solution takes place by the action of compressed air on a fine jet of the spray solution. This jet is broken up by the flow of high pressure gas as shown in FigII.1, which forces the liquid out of the atomizer through a narrow orifice.

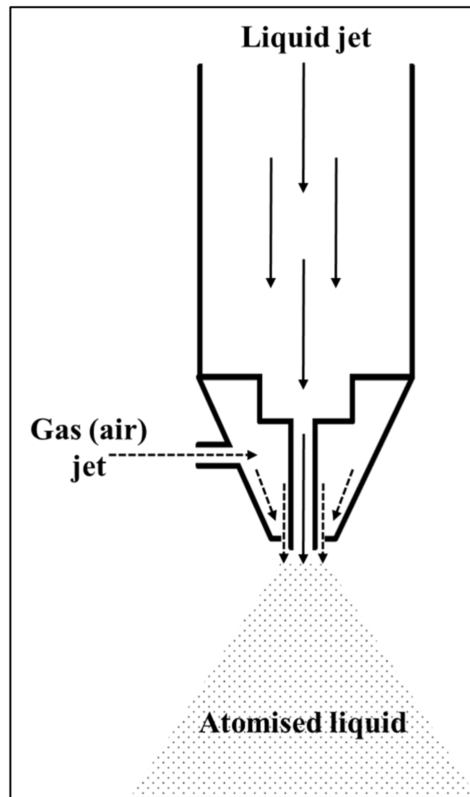

FigII.1: Diagram showing the breakup of a liquid jet by high pressure gas.

The second type of spray atomizer is the airless or centrifugal type, where atomization is achieved by forcing the solution directly through a specially designed orifice under high pressure. Using this method the droplets on leaving the atomizer have sufficient velocity to be transported to the substrate without the need for a carrier gas.

The third type of spray atomizer is a combination of (1) and (2). This has the effect of producing a more uniform droplet size.

The fourth type of atomizer is the ultrasonic variety in which a solution is shaken violently as a result of which mists are produced which have a very narrow droplet size distribution [4].

In spray ultrasonic, a thin liquid film formed on a high-frequency vibrating surface will break-up in a fine uniform spray. The ultrasonic vibration induces surface waves in the liquid film. As frequency is tuned, very regular square cells can be observed on the free surface just before reaching the resonance frequency (FigII.2). When resonance is reached, the amplitude grows till droplets break-up (FigII.3). The very regular square cells generate uniform size droplets [5].

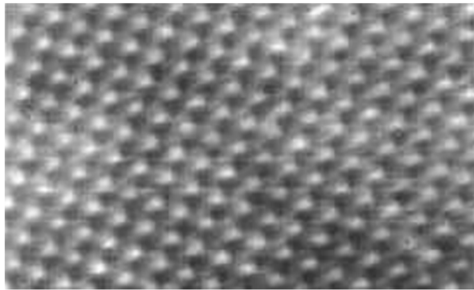

FigII.2: Standing surface waves patterns during the ultrasonic atomisation (water, f=50kHz).

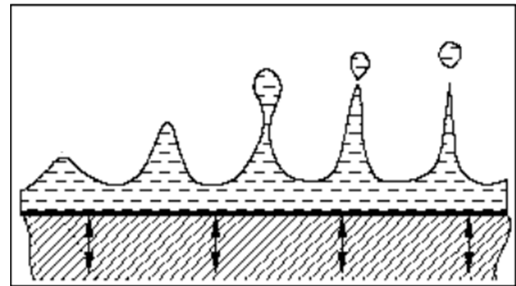

FigII.3: Mechanism of droplet break-up for the ultrasonic atomisation.

II.3.1.2.*Decomposition of Precursor:*

Many processes occur simultaneously when a droplet hits the surface of the substrate: evaporation of residual solvent, spreading of the droplet, and salt decomposition. Many models exist for the decomposition of a precursor.

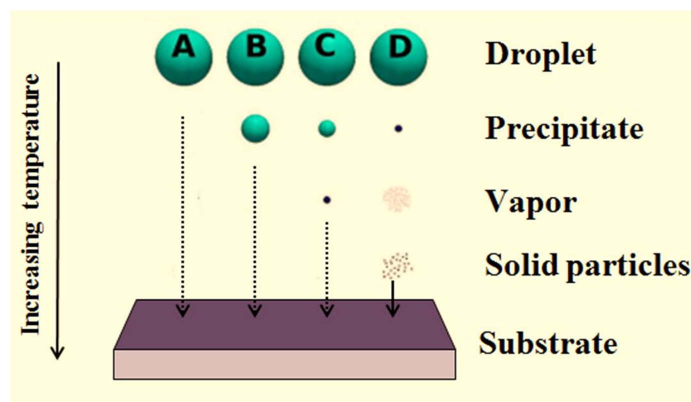

FigII.4: Description of the deposition processes initiated with increasing substrate temperature.

Viguie and Spitz proposed the following processes that occur with increasing substrate temperature [6]. In the lowest temperature regime (process A) the droplet splashes onto the substrate and decomposes (FigII.4). At higher temperatures (process B) the solvent evaporates completely during the flight of the droplet and dry precipitate hits the substrate, where decomposition occurs. At even higher temperatures (process C) the solvent also evaporates before the droplet reaches the substrate. Then the solid precipitate melts and vaporizes without decomposition and the vapor diffuses to the substrate to undergo a CVD process [3].

Highest temperatures (process D) the precursor vaporizes before it reaches the substrate, and consequently the solid particles are formed after the chemical reaction in the vapour phase. It is believed that the processes.

II.4.*Spray Apparatus:*

Our films were grown using an automated spray system, Holmarc's spray pyrolysis system model HO_TH_04 Company (HOLMARC «OPTO-MECHAT RONICS PVT.LTD», special for Physics Laboratory of Thin Films and Applications LPCMA (University of Biskra, Algeria), this one has been designed for research laboratories in thin films. Parameters like dispensing rate of the solution and speed of spray head (atomizer) movement are controlled precisely which are difficult to be controlled in manual process. A positive displacement pump controlled by stepper motor and microprocessor is used to dispense solution as per requirement. The spray head movement is also controlled by stepper motor driven linear stages in X and Y direction. The temperature of the substrate heater plate is controlled independently through a dedicated controller.

A desk top computer with windows OS is used to control the operations through serial port. This software for spray pyrolysis system can as well be used for documenting the relevant parameters used for sample preparation like temperature, air pressure, duration, etc.

II.4.1.*Specifications:*

The table below (Tab II.1) shows the deferent specifications of Holmarc's Spray Pyrolysis Equipment used in the current work.

Tab II.1: Table presents Holmarc's Spray Pyrolysis Equipment Specifications.

Actuator	Stepper motor
Dispensing unit capacity	50ml and 250ml
Dispensing rate	1 – 20ml.min^{-1}
Sprayer:	
Drive speed X axis (min-max)	10 – 800mm.sec^{-1}
Drive speed Y axis (min-max)	1 – 12mm.sec^{-1}
Sprayer traverse	X - Y 200mm max
Substrate base plate:	
Dimension	150 x 150mm
Max. temperature	500 °C
Power input	230V, 50Hz
PC connectivity	Serial port (RS 232)

II.4.2.*Equipment components*:

The schematic diagram of Holmarc's spray pyrolysis system is given in FigII.5 and FigII.6. The equipment consists of an atomizer (spray nozzle), a substrate heater (hot plate), a resistance, a temperature controller (thermocouple), and a solution container (syringe). The nozzle is moved in the X and Y directions over the substrate surface by the use of two stepper motors. Under our spray system configuration, the nozzle to substrate distance, the gas pressure as well as the solution flow can be varied (controlled). The microcontrollers of the spray unit are connected to the PC through serial ports and all data can be stored in the PC. The spraying and pause periods are controlled automatically. They are obtained considering surface temperature variations of 5% with respect to its optimum value. The nozzle movement (scanning speed) in the X-Y plane is also controlled automatically.

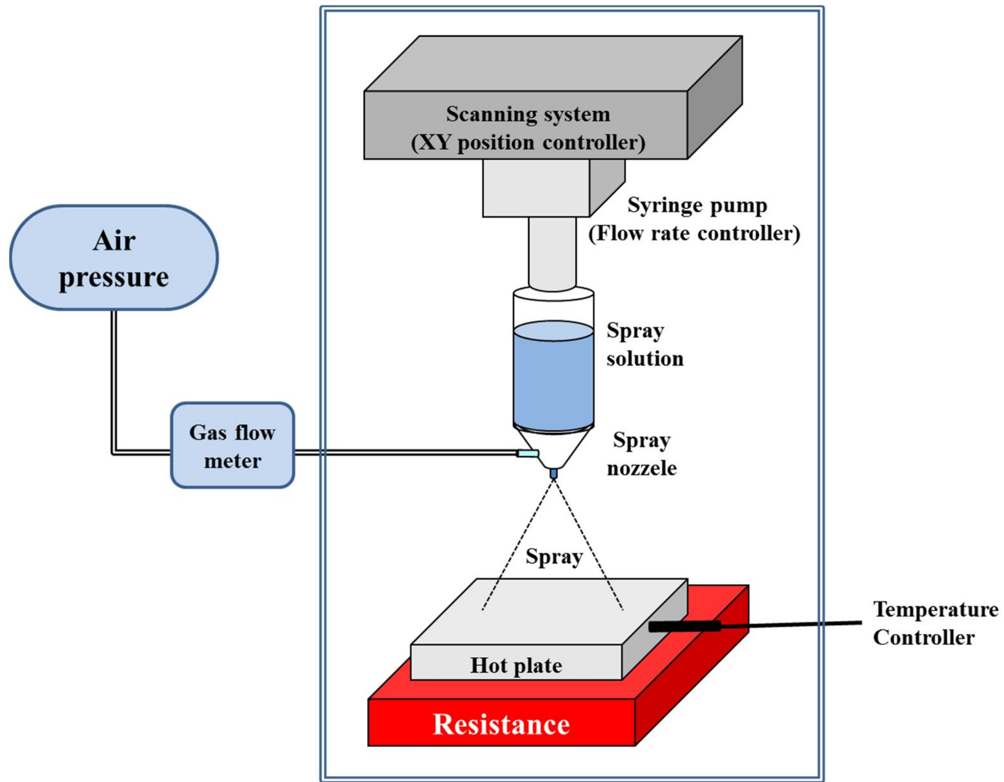

FigII.5: Schematic diagram of Holmarc's spray pyrolysis system (pneumatic system).

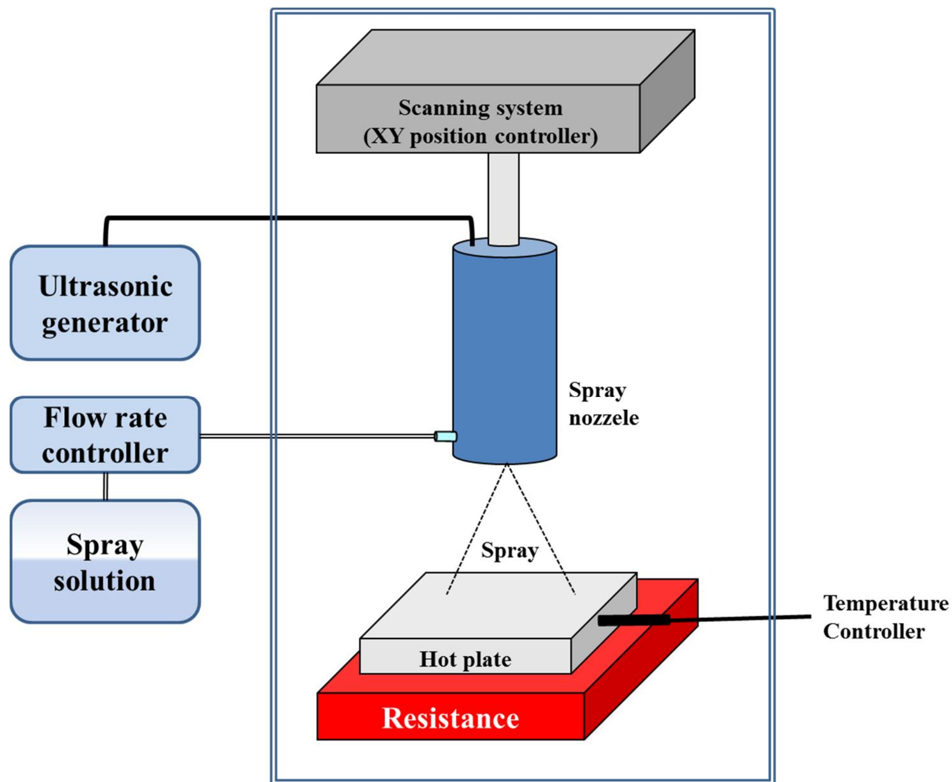

FigII.6: Schematic diagram of Holmarc's spray pyrolysis system (ultrasonic system).

II.4.2.1.*Spray pneumatic components:*

II.4.2.1.1.*Air compressor*:

This makes it possible to compress the carrier gas (in our case the air) which can be controlled by a Gas flow meter as needed. The high pressure action is broken up the spray solution into a jet of very fine droplets.

II.4.2.1.2.*Syringe pump (Flow rate controller)*:

Is a small infusion pump, fixed in the scanning system, used to control the flow rate of our spray solution; this one can be managed by Holmarc's software.

II.4.2.2.*Spray ultrasonic components:*

II.4.2.2.1.*Ultrasonic generator:*

With a frequency of 40 KHz, Ultrasonic generator employ high-frequency sound waves (outside human audible range) to produce atomization, that transforms the solution at the atomizer level (spray nozzle) into a jet of very fine droplets of 40 µm.

II.4.2.2.2.*Flow rate controller:*

Help us to control the flow rate of our spray solution as needed.

II.4.2.3.*Common components:*

II.4.2.3.1.*Scanning system (XY position controller)*:

The spray head, spray nozzle, can scan an area of 15cm x 15cm. The speed in X direction can be changed in the range of 10 – 800 mm/sec, while in Y direction in the range of 1 – 12 mm/sec. The speed in the X direction is the most critical due to it determines the kinetics of the deposition, while movement in the Y direction is only used to move the nozzle in this direction. Computerized scanning system Allow obtaining homogeneous thickness.

II.4.2.3.2.*Hot plate:*

Heated by joule effect (electrical resistance witch can be heated the plate so to 500°C), the temperature can be controlled using a K-type thermocouple. This plate is covered by Aluminum paper to avoid contamination.

II.4.2.4.*Holmac's software*:

The FigII.7 presents Holmac's software using to control our experience conditions in the spray pyrolysis Holmac's equipment and allows seeing the various experimental parameters.

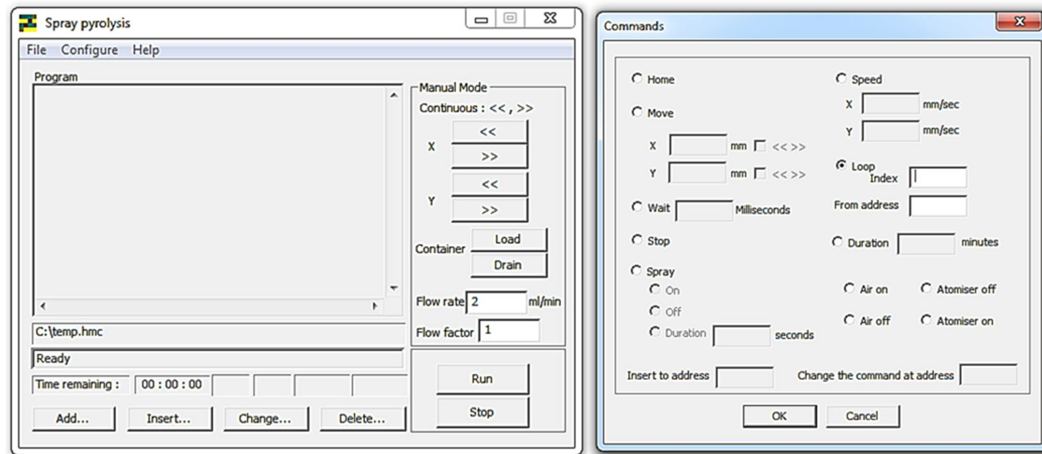

FigII.7: Holmac's software interface.

II.5.*Growth process details:*

II.5.1.*Substrate Preparation:*

II.5.1.1.*Substrate selection:*

Thin film requires a substrate to support itself [7]. The substrate is very important for the growth of thin films in terms of the lattice and thermal mismatching between it and the film because it commonly leads to the development of stress in the deposited film. The choice of substrate affects crystalline quality as well as optical and electrical properties of ZnO film [8].

In this work, our undoped and doped ZnO thin films were deposited in a microscopy slide glass substrates in a size of $1.5 \times 1.5\ cm^2 \times 0.1$ cm. The choice of glass as substrate was due to three reasons, for economic reasons, to perform a good optical characterization of our films and to minimize the stresses because the two materials constituting the sample (glass + zinc oxide) have a very close expansion (dilatations) Coefficients (α_{glass}=8,5 10^{-6} K^{-1}, α_{ZnO}=7,2 10^{-6} K^{-1}) [9, 10, 11].

II.5.1.2.*Substrate Cleaning:*

Substrate cleaning in thin film technology is an important step prior to deposition. It is necessary to remove the contaminants that would otherwise affect the properties of the film. Cleaning involves the removal of contaminants without damage to the substrate. While cleaning, the bond between the substrates is broken and contaminants are set free from the substrates. The properties that can be affected by the presence of contaminants include

morphology, nucleation electronic properties and the substrate film interface. Expected contaminants include fingerprints, dust, oil, and lint particles [7].

Initially, the substrates were wiped with cotton to remove the visible contamination such as air dust [12], then, were successively sonicated (placed in an ultrasonic bath) in Acetone and Di-ionized water for 05 minutes each. Substrates were rinsed with methanol before the sonication. Finally they were purged with dryer. Cycle presented in FigII.8.

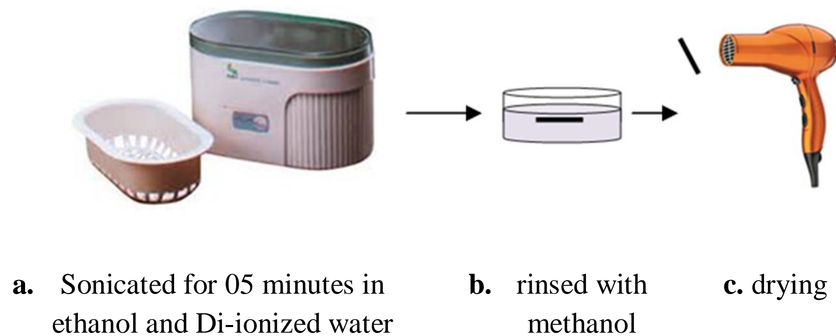

a. Sonicated for 05 minutes in ethanol and Di-ionized water **b.** rinsed with methanol **c.** drying

FigII.8: Schematic illustration of the Cleaning Process of the substrates.

When we finish cleaning, the substrate introduced in the used equipment and Start the heating process.

II.5.2.*Preparation of precursor solution*:

To study the influence of the deposition parameters on the ZnO thin films properties we have performed a variety of sample series, this samples are numbered corresponding to the deposition parameters (see Table II.2 and Table II.3). We can divide our experimental work into two parts:

First, ***ultrasonic study***, were we used spray pyrolysis ultrasonic system to deposit undoped and doped ZnO thin films.

Second, ***pneumatic study***, were we used spray pyrolysis pneumatic system to deposit undoped and doped ZnO thin films.

The spraying solution used in this work was prepared using two types of precursors, zinc acetate $[Zn(C_2H_3O_2)_2.2H_2O]$ (from Sigma Aldrich) with molar mass 219.4986 $g.mol^{-1}$and zinc chloride $[ZnCl_2]$ (from Sigma Aldrich) with molar mass 136 $g.mol^{-1}$, diluted in a volume absolute methanol solution (99.995%) purity, the solvent, then we have added a few drops of

acetic acid (CH_3COOH) as a stabilized, the mixture solution was stirred at room temperature for 1h using a Magnetic Agitator Mixer to yield a clear and homogeneous solution.

In the first study part, ultrasonic study, we have prepared three series of ZnO thin films:

a) Spraying solutions (without doping) with a different ZnO's concentrations.

b) Aluminum doped ZnO thin films were deposited using $Al(NO_3)_3.9H_2O$ (with a molar mass equal 375.1338 $g.mol^{-1}$; from Sigma Aldrich) as a dopant source.

c) Indium doped ZnO thin films were deposited using $In(NO_3).XH_2O$ (with a molar mass equal 390,91 $g.mol^{-1}$; from Sigma Aldrich) as a dopant source.

In the second study part, pneumatic study, we have prepared three series of ZnO thin films:

a) ZnO thin films none doped were performed at a different substrate temperatures using 1 bar of atmospheric air pressure as a carrier gas.

b) ZnO thin films none doped were performed at a different substrate temperatures using 1,5 bar of atmospheric air pressure as a carrier gas.

c) Aluminium doped ZnO thin films were deposited using $Al(NO_3)_3.9H_2O$ (with a molar mass equal 375,13 $g.mol^{-1}$; from Sigma Aldrich) as a dopant source.

Noting that, we have prepared our spraying solutions using Chemical lab glassware of the LPCMA laboratory: test tubes, pipettes, beakers, flasks, gauge, funnel ... and High Precision Balances with 0.0001 g precision. Also, to get the required doping ratio we have added the appropriate weight of dopant precursor in the start solution before mixing process.

II.5.3.*Films deposition:*

This part of the research involved the growth of doped and undoped zinc oxide in thirty-four growth experiments (Successful, without taking into account the other) which were carried out realized in order to investigate the influence of deposition conditions on the film properties. The conditions of ZnO deposition are described below in the Tab II.2 and Tab II.3.

Tab II.2: the experimental conditions of the deposit ZnO thin films, for ultrasonic process.

	Solution molarity ($Mol.L^{-1}$)	Substrate temperature (°C)	Solution flow rate ($ml.min^{-1}$)	Nozzle-substrate distance (cm)	Deposit time (min)	Atomic ratio [dopant]/[Zn] (at %)	Dopant source
Series n°1	0,05	350	0,5	9	10	/	/
	0,075						
	0,1						
	0,15						
	0,2						
	0,3						
	0,4						
	0,5						
Series n°2	0,1	350	0,5	9	10	0	**$Al(NO_3)_3$ 375.1338 $g.mol^{-1}$**
						1	
						2	
						3	
						4	
						5	
Series n°3	0,1	420	0,5	9	10	0	**$In(NO_3)_3.xH_2O$ 390,91 $g.mol^{-1}$**
						1	
						2	
						3	
						4	
						5	

Tab II.3: the experimental conditions of the deposit ZnO thin films, for pneumatic process.

	Solution molarity ($Mol.L^{-1}$)	Substrate temperature (°C)	Air pressure (bar)	Solution flow rate ($ml.min^{-1}$)	Nozzle-substrate distance (cm)	Deposit time (min)	Atomic ratio [dopant]/[Zn] (at %)	Dopant source
Series n°1	0,1	300	1	0,3	11,5	10	/	/
		350						
		400						
		450						
Series n°2	0,1	300	1,5	0,3	11,5	10	/	/
		350						
		400						
		450						
Series n°3	0,1	400	1	0,2	11,5	20	0	**$Al(NO_3)_3.9H_2O$ 375,13 $g.mol^{-1}$**
							1	
							2	
							3	
							4	
							5	

ZnO thin films were synthesized by spray pyrolysis deposition system using Holmarc's equipment at Physics Laboratory of Thin Films and Applications LPCMA, University of Biskra, Algeria.

Usually, to get our samples we take the following steps for each sample:

1. Chemical lab glassware was very well cleaned.
2. The composite targets (Zn precursors, dopants: Al and In precursors) were prepared. Its powders were first weighted and mixed with corresponding concentrations in solvent by magnetic mixer for 1 hour.
3. Glass was cut by a Glass Cutter Diamond Cutting Wheel Pen to make substrates which are well cleaned according to the previous stages mentioned.
4. Clean substrates were placed into equipment, on the hot plate, to be heated to the required temperature; temperature can be controlled by a thermocouple connected to a Temperature controller integrated in the equipment.
5. Setup the program in the computer and adjust the experience conditions: flow rate, speed of scanning system according X and Y directions (S_X=50 mm/s, S_Y=5 mm/s), deposition time and deposition technique type (ultrasonic or pneumatic)…
6. After achieve the desired substrate temperature and adjust the equipment; in particular determination of pressure value, Nozzle-substrate distance (9 cm for ultrasonic (Optimized by our group search) and 11,5 cm for pneumatic (Not Adjustable Optimized by Manufacturer) and ultrasonic generator amplitude (40 KH); the deposition process can be started.

After the end of deposition process, the substrate temperature will decrease to room temperature by about 2 degrees per minute.

II.6.*Characterization Methods of Thin Films:*

Thin films are usually characterized by their structural, stoichiometric, optical, electrical and mechanical properties. In this section, the characterization methods used in this work are reviewed briefly.

II.6.1.*X-ray Diffraction Technique:*

X-ray diffraction is one of the widely used experimental techniques for determining lattice parameters, preferred orientation of the crystal, phase composition (qualitatively and quantitatively), grain sizes, lattice strain and residual stress etc. [13].

The mechanism of XRD is simple. When a monochromatic *x-ray* beam incident onto a crystal sample, the constructive diffractions (or interference) from parallel planes of atoms with interplanar spacing *d* occur if Bragg's law is satisfied [14] (see FigII.9),

$$2d\sin\theta = n\lambda \qquad \text{Eq } II.1$$

Where n is integer that indicates the order of the reflection, θ is Bragg angle, and λ is the wave length of the *x-ray* beam. By measuring the Bragg angle θ, the interplanar distant d can be obtained if the wavelength of the x-ray beam is known.

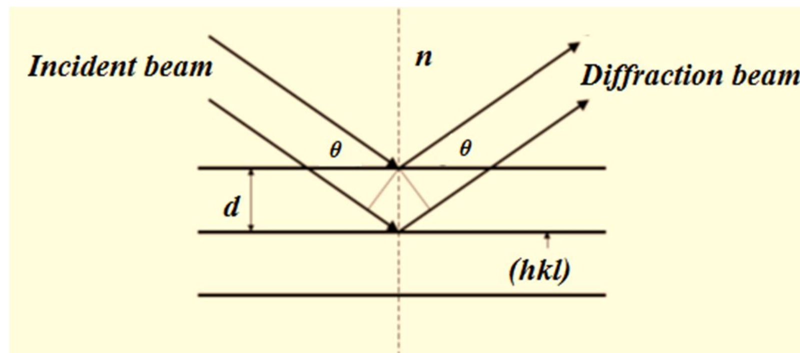

Fig II.9: Schematic diagram of Bragg diffraction from set parallel planes [13].

The crystal structure of our ZnO doped and undoped thins films were characterized using an X-ray diffraction system, Bruker D8 ADVANCE diffractometer available at Mohamed Khaider Biskra university level, FigII.10; employing a Cu Kα tube (λ = 0.154183 nm) radiation. The data obtained were background subtracted using the program included in the DIFFRAC.SUITE provided by Bruker. The schematic diagram of X-ray diffractometer optical system is cited in FigII.11 [15].

FigII.10: D8 ADVANCE diffractometer.

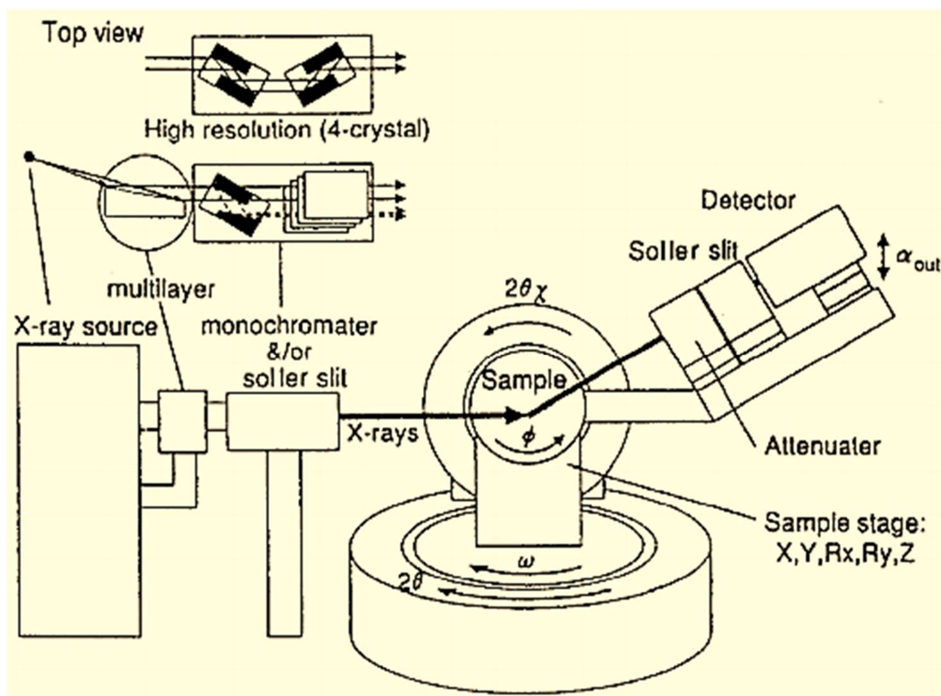

FigII.11: The schematic diagram of X-ray diffractometer optical system.

The theoretical peak positions for zinc oxide along with their relative intensities were obtained by compared with the X-ray diffraction spectrum (XRD) with stoichiometric ZnO powder from ASTM files (ASTM 36-1451) shown in FigII.12 [9].

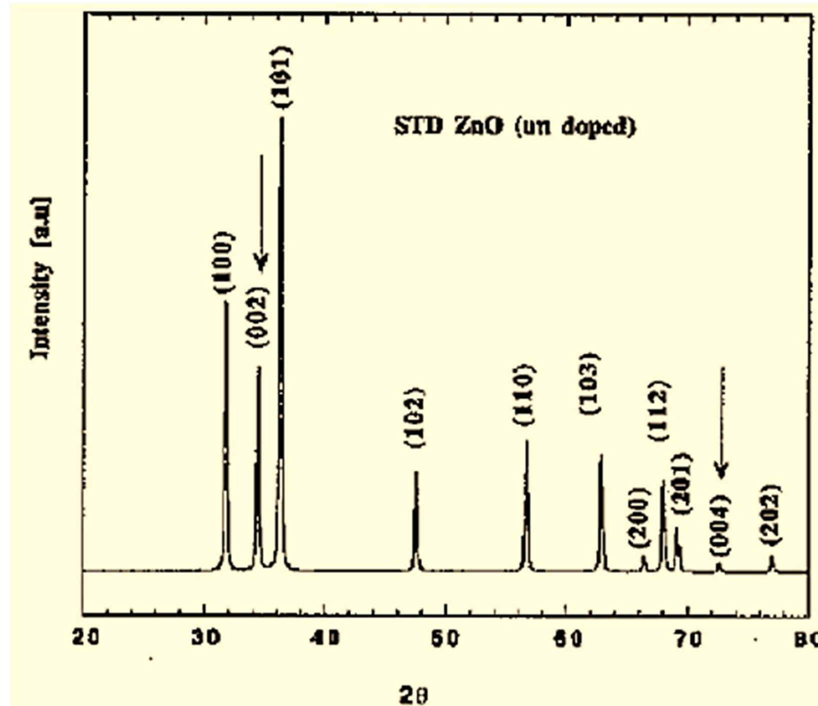

FigII.12: X-ray diffraction spectrum (XRD) with stoichiometric ZnO powder (ASTM 36-1451).

II.6.1.1.*The texture coefficient:*

The texture coefficient represents the texture of the particular plane, deviation of which from unity implies the preferred growth; it allows us to evaluate the preferred orientation of the ZnO films.

The texture coefficient *TC*(*hkl*) can be calculated from the X–ray data using the formula of the intensity peaks correspond to the (100), (002), (101) and (102) planes [16]:

$$TC = \frac{I(hkl)/I_0(hkl)}{N^{-1}\sum_n I(hkl)/I_0(hkl)} \qquad Eq\,II.2$$

where $I(hkl)$ is the measured relative intensity of a plane (*hkl*), $I_0(hkl)$ is the standard intensity of the plane (*hkl*) taken from the JCPDS data card 36–1451, *N* is the reflection number and is the number of diffraction peaks. The texture coefficient was related to the atomic densities corresponding to that plan as X-ray intensities, which was corresponds to planer densities.

II.6.1.2.*Grain size determination:*

The grain size G can be estimated using the Scherrer's formula [17]:

$$G = \frac{0.94\lambda}{\Delta(2\theta)cos\theta} \qquad Eq\ II.3$$

Where λ is the *X-ray* wavelength (1.54056 A°), θ and $\Delta(2\theta)$ are the Bragg diffraction angle of the XRD peak (in degree) and the full width at half maximum (in radian) of intensive diffraction peak respectively.

II.6.1.3.*Stress determination:*

The stress σ_{film} values in our films were estimated from the observed shift, in the diffraction peak between their positions in the XRD spectra via the formula, which is valid for a hexagonal lattice [18]:

$$\sigma_{film} = \frac{2c_{13}^2 - c_{33}(c_{11} + c_{12})}{2c_{13}} \times \frac{c_{film} - c_0}{c_0} \qquad Eq\ II.4$$

Where c_{ij} (i,j = 1, 2, 3) stands for the elastic constants. c_0 (0.5205 nm) is the lattice constant of bulk ZnO and c_{film} is the lattice constant of fabricated ZnO films, which can be calculated using the following equation:

$$c_{film} = 2d_{002} = \frac{\lambda}{\sin\theta} \qquad Eq\ II.4$$

Where θ is the Bragg diffraction angle. Substituting the values of $c$ij (i,j = 1, 2, 3) with $c11$=208.8, $c33$ = 213.8, $c12$ = 119.7, $c13$ =104.2 GPa (ZnO elastic constants). We can obtain the residual stress σ_{film} in ZnO film by the following equation:

$$\sigma_{film} = -232.8 \times \varepsilon \qquad Eq\ II.5$$

Where ε is the strain in the films in the direction of the c-axis:

$$\varepsilon = \frac{c_{film} - c_0}{c_0} \qquad Eq\ II.6$$

The films with values of c greater than the bulk value (0.5205 nm) have a positive (or extensive) strain in them whereas those with lower values have a negative (or compressive strain) [19].

Noting that, The XRD spectra were used to deduce the lattice constants a and c of the ZnO crystal lattice depending on the relation [20]:

$$\frac{1}{d_{hkl}^2} = \frac{4(h^2 + hk + k^2)}{3a^2} + \frac{l^2}{c^2} \qquad Eq\ II.7$$

Where d_{hkl} is the distance of lattice planes, and h, k and l are Miller indices. This was done by calculating d_{hkl} using Bragg's law $d_{hkl} \sin\theta = n\lambda$, where θ is Bragg's angle, 2θ is the scattering angle, λ is the X-ray wavelength which is 1.54 A° for the Cu(Ka) line, and n is an integer representing the order. A plot of $1/d_{hkl}$ against l^2 and a linear fit were performed. The lattice parameters a and c where calculated using *Eq II.7* and the fit parameters.

II.6.2.*Scanning electron microscope (SEM):*

When a surface is bombarded with accelerated electrons, as is the case in scanning electron microscopy, different signals are emitted from the bombarded surface from different depths, as shown in FigII.13.

The three main analytical techniques used in a modern scanning electron microscope are: secondary electron (SE) detection, back-scattered electron (BSE) detection and X-ray detection (energy dispersive spectroscopy–EDS). Secondary electrons are inelastically scattered, low energy (50 eV), abundant and surface specific which makes them ideal for imaging topographic features.

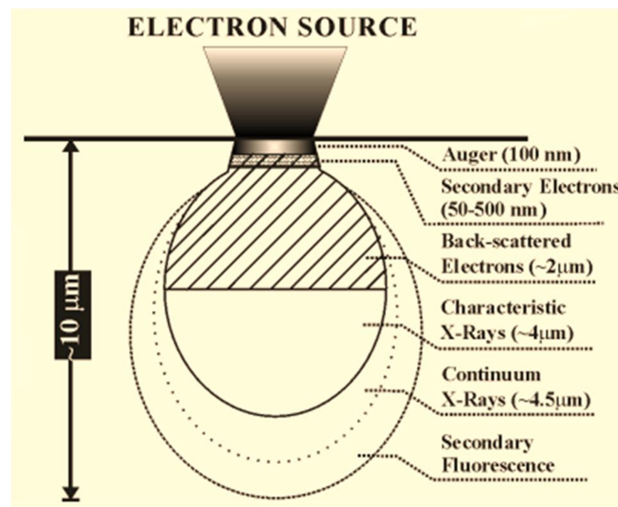

FigII.13: A schematic representation of the sub-surface electron interaction volume.

FigII.14 shows a schematic diagram of the electron gun and the lens system of a SEM [19]. Electrons from a thermionic cathode (tungsten hairpin cathode or LaB6 cathode) or a field-

emission cathode (cold-cathode type: tungsten single crystal emitters; thermally-assisted Schottky type: tungsten tip covered with ZrO_2) are accelerated by a voltage of 1–50 kV between cathode and anode. The beam cross-section with a diameter of 10–50 µm for thermionic and 10–100 nm for field-emission guns is then demagnified by a two- or three-stage electron lens system so that an electron probe of about 1–10 nm carrying an electron probe current between 1–100 pA is formed at the specimen surface. A deflection coil system in front of the last lens scans the electron beam in a raster fashion [21].

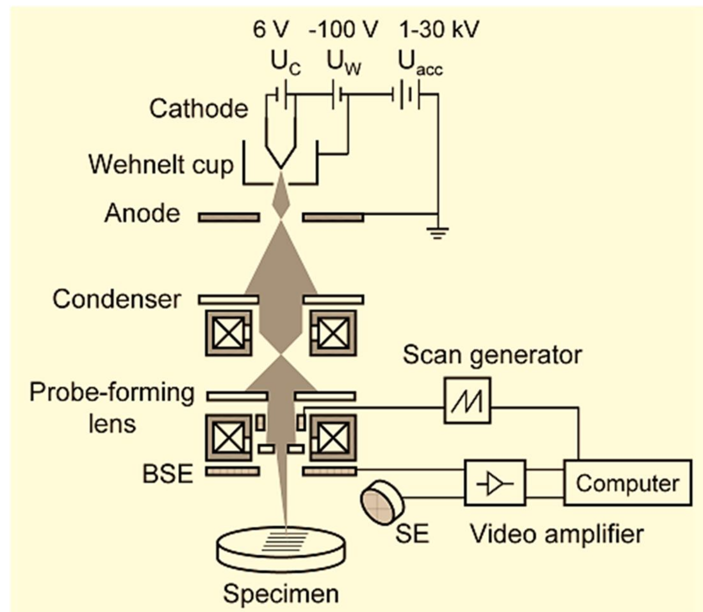

FigII.14: Schematic diagram of the electron gun column of a SEM.

A **JSM-6301F** scanning electron microscope (SEM) FigII.15 was used in this study to investigate the surface morphology for some films; this last is a high performance general purpose Field Emission SEM with a high resolution of 1.5 nm (6.0nm at 1kV). The JSM-6301F is also an analytical SEM with the addition of a backscatter detector and an Energy Dispersive Spectroscopy (EDS) Detector.

FigII.15: JSM-6301F scanning electron microscope.

II.6.3.*Film thickness calculation:*

The thickness measurements of the deposited films were determined by three methods: Scanning electron microscopy, spectrophotometry and weight difference method.

II.6.3.1.*Scanning electron microscopy:*

SEM allowed to get, after transversely cut (make cross sections) the samples, photographs in cross section making it possible to measure the films thickness [22] (see the example in FigII.16). Here, we can use software called "Visiometer" to calculate our film thickness that directly.

This technique makes it possible to obtain thickness measurements with an accuracy of approximately 5 nm, for films whose thickness is greater than 100 nm [9].

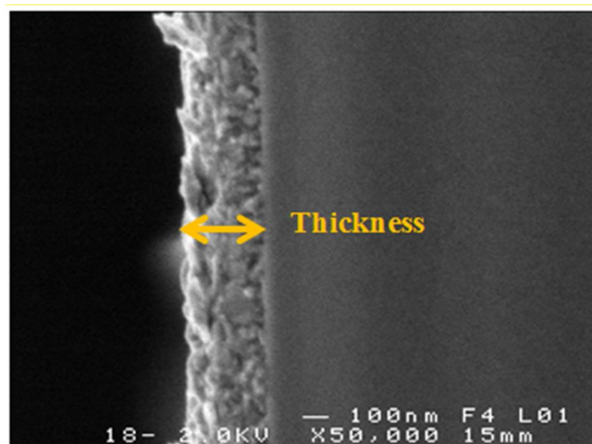

FigII.16: SEM cross section photograph of ZnO:Al (1at %), Shows that the thickness is about 300 nm.

II.6.3.2. *UV-Visible Spectrophotometry:*

FigII.17 shows the optical transmittance spectrum of ZnO thin film in the wavelength range from 200 to 1100 nm.

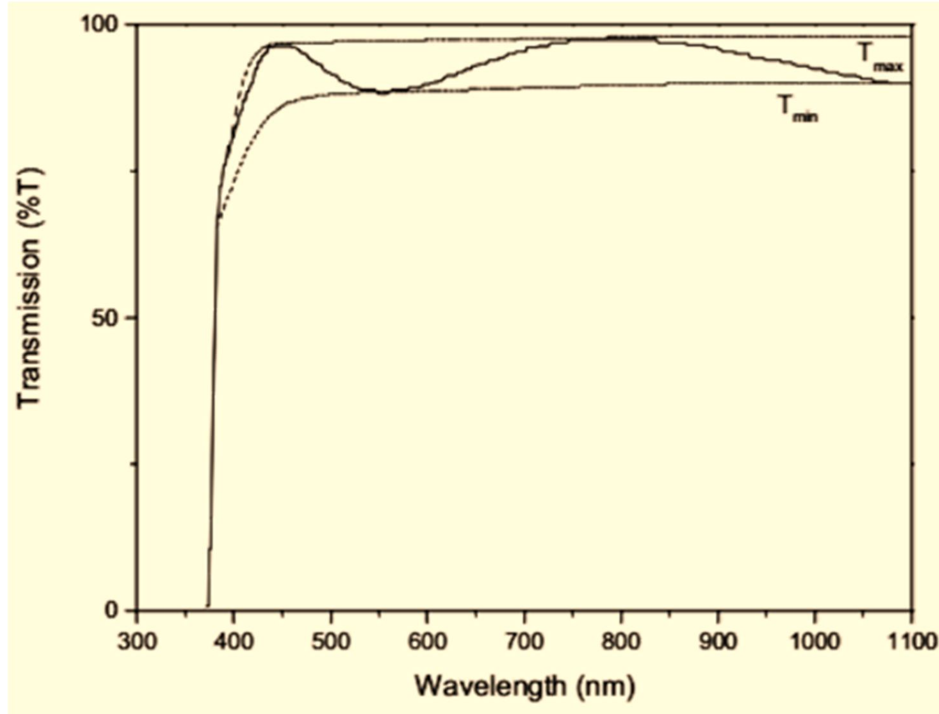

FigII.17: UV/VIS/NIR transmission curve of ZnO film.

The thickness of the film was calculated using the following relation [17]:

$$d = \frac{\lambda_1 \lambda_2}{2\left[n_{(\lambda_1)}\lambda_2 - n_{(\lambda_2)}\lambda_1\right]} \qquad Eq\ II.8$$

Where $n_{(\lambda 1)}$ and $n_{(\lambda 2)}$ are the refractive indices at the two adjacent maxima (or minima) at λ_1 and λ_2, which can be calculated using next mentioned equations.

II.6.3.3. *Weight difference method:*

In this simpler method we have used the mass of the film according to the next details; w_1 is the weight of cleaned substrate, w_2 is the weight of substrate after deposition process (cleaned substrate plus film).

The weight of the film is:

$$\Delta w = w_2 - w_1 \qquad Eq\ II.9$$

The thickness ***d*** of our film can be calculated using the following equation:

$$d = \frac{\Delta w}{a.b.\rho} \qquad Eq\ II.10$$

Where a, b are the film length and width respectively (FigII.18) and ρ is the film density (the ZnO density is 5.67 g/cm^3 [23]) [24].

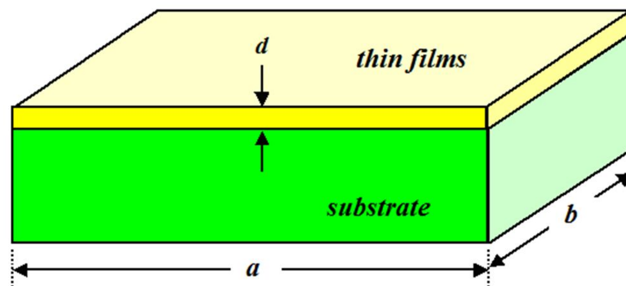

FigII.18: the sample dimensions used to calculate film thickness.

II.6.4. ***HebalOptics software:***

This program is developed and verified by Professor *mr.Djelloul abdelkadeur* and realized by the student *zine el abidinehebal* as a part of his magister project titled “optical properties of thin layers type A2B6” in abbes laghrour university, khenchela, algéria.

To use this program, we load the transmittance data into the program, which gives us after simulation:

- Refractive coefficient.
- Extinction coefficient.
- Refractive coefficient of the substrate.
- Wavelength of optical band gap.
- Film thickness.
- Band gap energy.

II.6.5.*Optical characterization:*

II.6.5.1.*UV-Vis spectroscopy:*

The intensity of light after it passes through the cuvette, can be related it to transmittance (T). Transmittance is the fraction of light that passes through the sample. This can be calculated using the equation [25]:

$$T = \frac{I}{I_0} \qquad Eq\,II.11$$

Where I is the light intensity after the beam of light passes through the cuvette and I_o is the light intensity before the beam of light passes through the cuvette. Transmittance is related to absorption (A) by the expression:

$$A = -\log(T) = -\log\left(\frac{I}{I_0}\right) \qquad Eq\,II.12$$

Noting that absorbance stands for the amount of photons that is absorbed. FigII.19 illustrates transmittance of light through a sample.

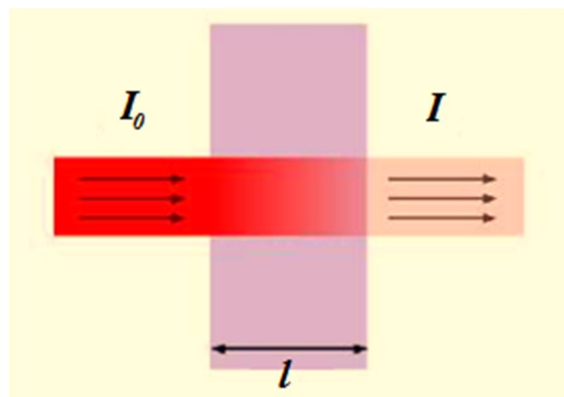

FigII.19: Transmittance of light through a sample.

An UV/Vis spectrophotometer measures the intensity of light passing through a sample (I), and compares it to the intensity of light before it passes through the sample (I_0) expressed in absorbance (A) or transmittance (T) [25]. The spectrophotometer is a double beam double monochromator type with a tungsten source for producing visible and near infrared radiation.

The beam is split into two beams; one is directed to the ZnO sample while the other passes through a blank control (substrate). The path lengths over which the split beams travel are equal. The detector then compares the intensity of the two beams and calculates a transmittance for the film with respect to the substrate. Since the comparison between the sample and reference beams is made simultaneously, the instrument compensates for beam fluctuations FigII.20 [4].

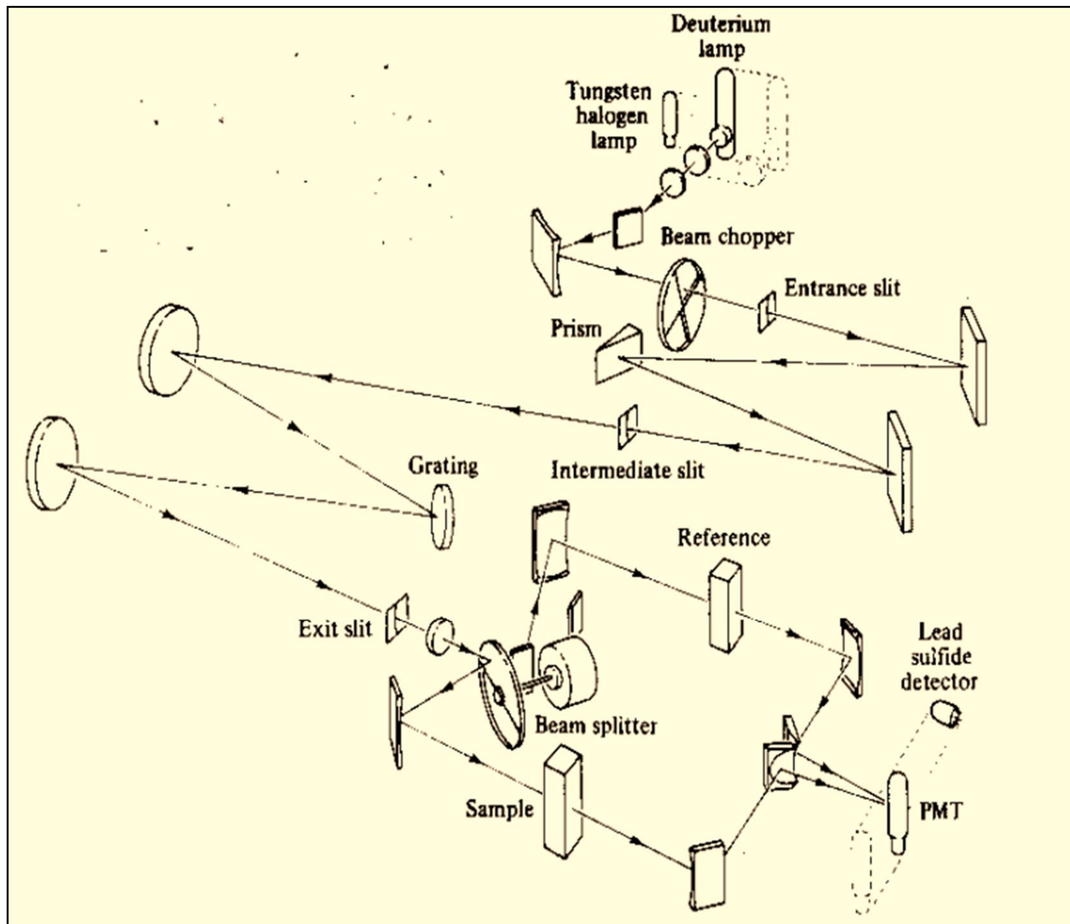

FigII.20: Simplified schematic diagram of the CARY model 14 spectrometer [26].

UV-Vis spectroscopic data allowed getting an optical transmittance spectrum of ZnO thin film in the wavelength range from 200 to 1100 nm. Using this data we can calculate: absorption coefficient, Refractive index, extinction coefficient, band gap energy and Urbach energy.

II.6.5.2.*The absorption coefficient:*

The absorption coefficient α of ZnO films was determined from transmittance measurements. The films' absorption coefficient was calculated using the following expression [27]:

$$T = e^{-\alpha d} \qquad Eq\ II.13,$$

$$\alpha = -\frac{1}{d} ln(T) \qquad Eq\ II.14$$

Where T is the normalized transmittance, d is the film thickness

II.6.5.3.*Refractive index and extinction coefficient calculation:*

The index of refraction n at different wavelengths was calculated using the envelope curve for T_{max} and T_{min} in the transmission spectra (Fig II.17). The expression for refractive index is given by [28],

$$n = \left[N + (N^2 - n_s^2)^{1/2}\right]^{1/2} \qquad Eq\ II.15,$$

$$N = \frac{(n_s^2 + 1)}{2} + 2n_s \frac{(T_{max} - T_{min})}{T_{max} T_{min}} \qquad Eq\ II.16$$

Where n_s is the refractive index of the substrate. T_{max} and T_{min} are maximum and minimum transmittances at the same wavelength in the fitted envelope curves on the transmittance spectrum.

The extinction coefficient can be also calculated by the following equations [29]:

$$K = \frac{\alpha\lambda}{4\pi} Eq \qquad Eq\ II.17$$

Where α is the absorption coefficient and d is the film thickness. λ is the wavelengths.

II.6.5.4.*Band gap energy:*

The optical energy band gaps Eg of the films were calculated using the Tauc's relationship as follows [30]:

$$\alpha h\nu = A(h\nu - E_g)^n \qquad Eq\ II.18$$

Where: α is absorption coefficient, A is constant, h is Planck's constant υ is photon frequency and n is 1/2,2,3/2 and 3 for allowed direct, allowed indirect, forbidden direct and forbidden indirect band gap semiconductors, respectively. Since ZnO is a direct band gap semiconductor, value of n was selected to be 1/2. Noting that: $\frac{hc}{\lambda} = \frac{12400}{\lambda\,(A^{\circ})}$.

An extrapolation of linear region of a plot $(\alpha h\upsilon)^2$ on y axis versus photon energy (hυ) on x axis gives the value of the band gap energy. The direct band gap of ZnO films was estimated by from extrapolation of linear portion of graph $(h\upsilon\alpha)^2=0$ as shown in FigII.21.

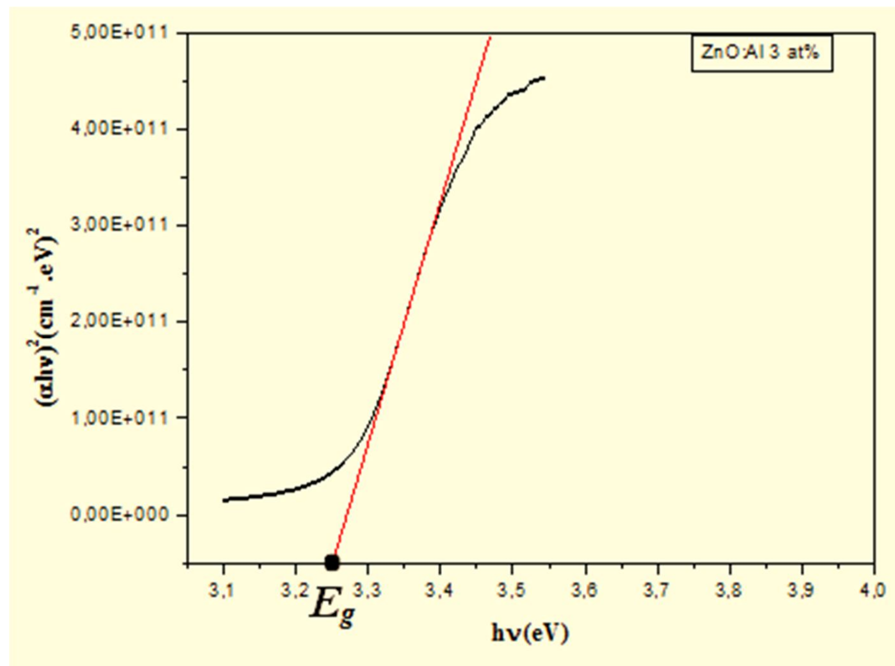

FigII.21: band gap energy determination using an linear region extrapolation of a plot $(\alpha h\upsilon)^2$ as a function of photon energy for a ZnO thin film doped by Al at 3 at%.

II.6.5.5. *Urbach energy:*

The degree of structural disorder present in the film is calculated by a quantity called Urbach energy (E_u). In semiconductors, there is an exponential increase of the fundamental absorption near the band gap energy. The width of the exponential absorption edge is called the Urbach energy [31], which can be obtained using [32, 33]:

$$\alpha = \alpha_0 exp\left(\frac{h\nu}{E_u}\right) \qquad Eq\ II.19$$

Where, and α_0 are constants, E_u is the Urbach energy. The plot of logarithm of absorption coefficient against the photon energy allowed getting E_u value, which is the reciprocal of the slope of the linear portion of the graph.

II.6.6.*Electrical resistivity measurement:*

II.6.6.1.*Four points method*: [34, 35]

The electrical resistivity of a material is its capacity to resist the flow of an external electric current. By definition, it is the resistance R of a unit cube. The resistivity ρ of a prismatic sample of section A and length L is:

$$\rho = R.\frac{A}{L}[\Omega.m] \qquad Eq\ II.20$$

The configuration the most commonly used is the linear array four point probe in which 4 electrodes are used for the measurement: the current is injected through two point sources (current electrodes, C1 and C2) and the potential difference is measured between the two remaining electrodes (P1 and P2) (FigII.22).

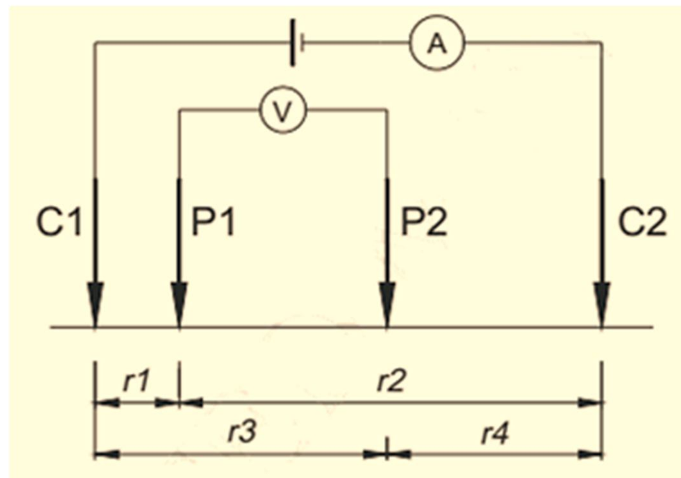

FigII.22: Four-points probe.

The electrical resistivity is determined by:

$$\rho = \frac{2\pi}{\left(\frac{1}{r_1}-\frac{1}{r_2}\right)-\left(\frac{1}{r_3}-\frac{1}{r_4}\right)}.\frac{\Delta V}{I} \qquad Eq\ II.21$$

Where ΔV is the electric potential difference between P1 and P2, I is electric current intensity. This formula is validated for a homogenous and semi-infinite medium.

One of the most used types of four-point measurement is the Wenner configuration (developed by Wenner, 1915). In this configuration, all four probes are equally spaced along a straight line and separated from one another by an equal distance.

Our thin films electrical resistivity was measured via four point device, ***C4S4 –Point Probe Head model*** FigII.23**,** which applies the previously mentioned type of measurement.

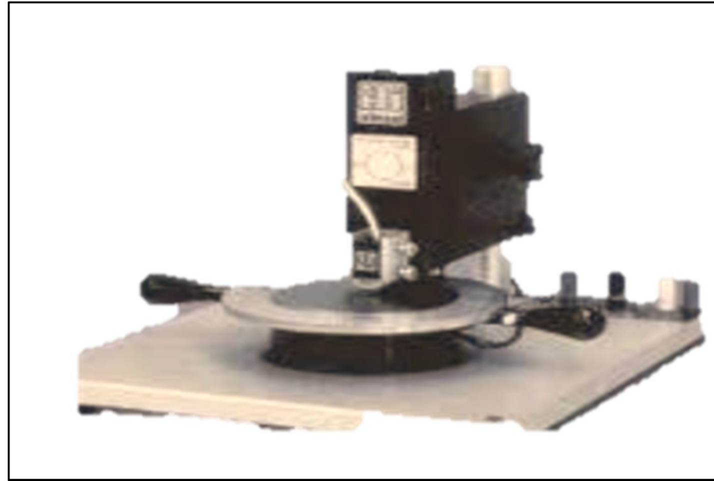

FigII.23: **C4S4 –Point Probe Head model,** four points device.

II.6.6.2.*Electrical resistivity calculation:*

A current in a thin film gives rise to the logarithmic potential [36]:

$$\Delta V = -\frac{I\rho}{2\pi} . \ln r \qquad Eq\ II.22$$

Where ΔV is the potential, I the current, ρ the sheet resistivity and r the distance from the current source.

In particular, the potential for a dipole (+ source and - source) become:

$$\Delta V = \frac{I\rho}{2\pi} . \ln \frac{r_1}{r_2} \qquad Eq\ II.23$$

In the case of a four point probe on a sheet, the two outside (current) represent the dipole. Therefore, the potential difference between the two inner points is, for infinite sheet:

$$\Delta V = \frac{I\rho}{2\pi}.\,ln\,2 \quad Eq\; II.24$$

(Only equal point spacing is considered). Thus, the sheet resistivity is obtained as:

$$\rho = \frac{V}{I}\frac{\pi}{ln\,2} = \frac{V}{I}4.5324 \quad Eq\; II.25$$

II.6.7.1.*Hall Effect measurement:*

Hall Effect measurement is one of the most powerful tools for an investigation of the transport properties such as carrier concentration and Hall mobility of the samples [37]. We have performed Hall Effect measurements on some ZnO doped films, as possible, at a room temperature using the composition shown in FigII.24.

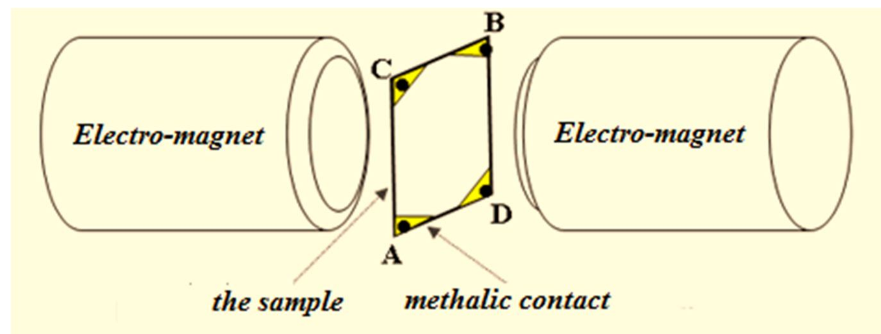

FigII.24: Hall Effect composition.

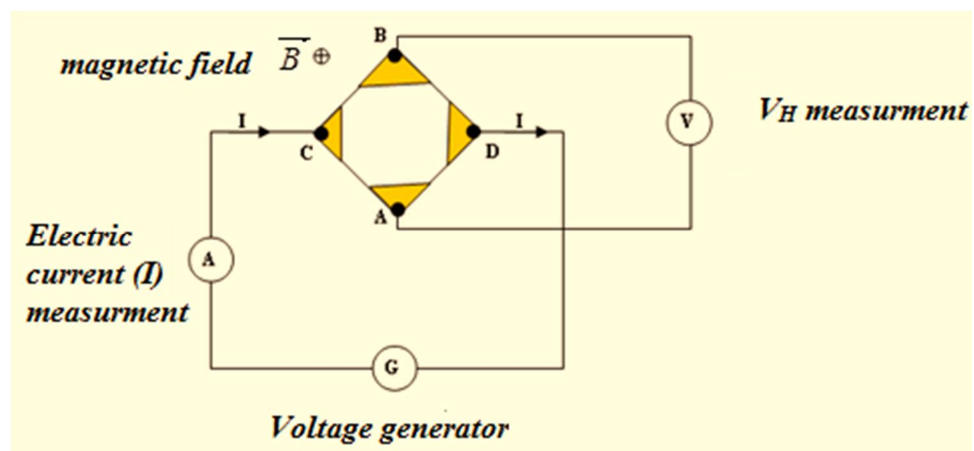

FigII.25: The contacts on the sample to measure V_H.

If an electric current I flow through a conductor along the x-axis (current axis, C to D), in the presence of a perpendicular magnetic field $\vec{B}$ (as shown in FigII.25). The electrons, under the force of Lorentz, deviate to the direction y. This electron drift causes an excess of charges on the side of the sample, leading to a potential between the two sides of the sample. This measurable transverse voltage is called the Hall Effect (V_H) after E. H. Hall who discovered it in 1879 [38]. The Hall Effect apparatus is shown in FigII.27.

The Hall Voltage can be calculated using the following equation [39]:

$$V_H = \frac{I\,B}{e\,N_H\,d} \qquad Eq\,II.26$$

Were, e is the electron charge, d the film thickness and N_H the carrier concentration.

The plot of Hall voltage V_H against the magnetic flux density $B(\Delta V_H = f(B))$ allows getting the carrier concentration N_H (FigII.26), were:

$$\Delta V_H = \frac{I}{N_H\,e\,d} B;\ R_H = \frac{1}{N_H\,e} \qquad Eq\,II.27$$

$$the\ plot = R_H \frac{I}{d}$$

R_H called the Hall coefficient (or constant). The carrier concentration given by:

$$N_H = \frac{1}{R_H\,e} Eq \qquad II.28$$

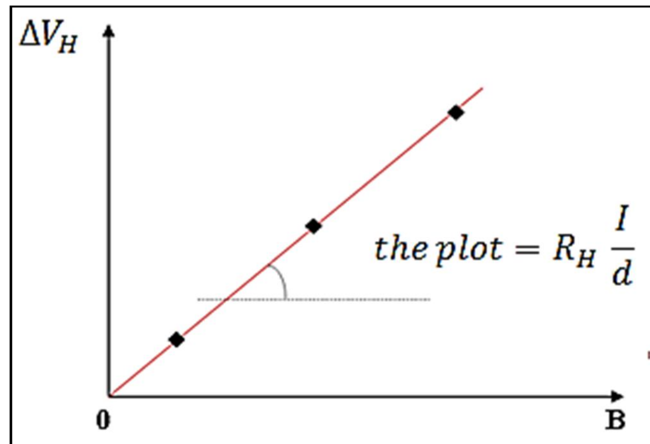

FigII.26: $\Delta V_H = f(B)$ graph.

It is also possible to specify the type of semiconductor (n or p) using the product B * R_H sign, where, for semiconductor n type ($B*R_H$) < 0 [40].

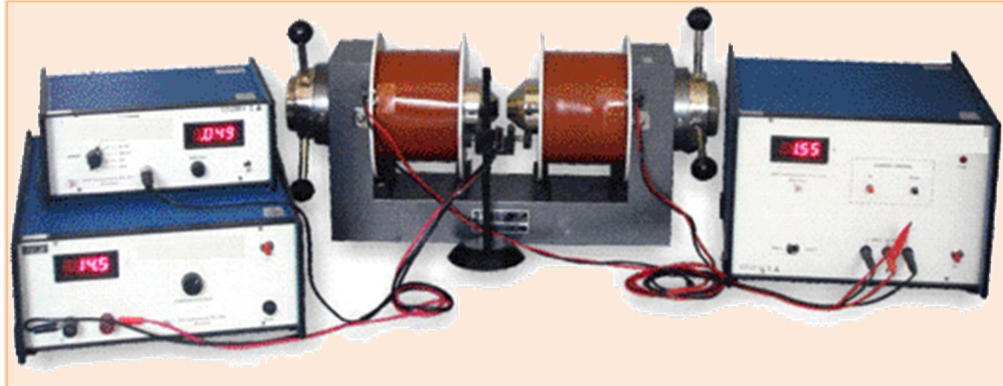

FigII.27: The Hall Effect apparatus.

References:

[1] S. Kozhukharov, S. Tchaoushev, Journal of Chemical Technology and Metallurgy, 48 (2013) 111-118.

[2] L. Filipovic, S. Selberherr, G. C. Mutinati, E. Brunet, S. Steinhauer, A. Kock, J. Teva, J. Kraft, J. Siegert, and F. Schrank, Proceedings of the World Congress on Engineering (WCE), II (2013) 987-992.

[3] D. Perednis and L. J. Gauckler, Journal of Electroceramics, 14 (2005) 103-111.

[4] A. J. C. Fiddes, Deposition of zinc oxide by spray pyrolysis, doctoral thesis, Durham University, 1993.

[5] M. Dobre and L. Bolle, Theoretical prediction of ultrasonic spray characteristics using the maximum entropy formalism, ILASS-Europe'98 Manchester, 1998.

[6] J.C. Viguie and J. Spitz, J. Electrochem, 122 (1975)585-588.

[7] M. S. Sameem, IJRSET, II (2015) 19-24.

[8] A. Taabouche, A. Bouabellou, F. Kermiche, F. Hanini, S. Menakh, Y. Bouachiba, T. Kerdja,C. Benazzouz, M. Bouafia, S. Amara, Materials Physics and Chemistry, 3 (2013) 209-213.

[9] S. Rahmane, Elaboration Et Caracterisation De Couches Minces Par Spray Pyrolyse Et Pulverisation Magnetron, doctoral thesis, University of Mohamed Kheider Biskra, 2008.

[10] K. S. Valeev and V. B. Kvaskov, lnorg. Mater., 9 (1973) 645-46.

[11] C. Wagner, Le verre à usage pharmaceutique, ADF2014 France, N°743 (2014) 52-55.

[12] T. Srinivasulu, K. Saritha, K.T. R. Reddy, Modern Electronic Materials, 3 (2017) 76-85.

[13] C. Jin, Growth and Characterization of ZnO and ZnO-Based Alloys $Mg_xZn_{1-x}O$ and $Mn_xZn_{1-x}O$, doctoral thesis, North carolina State University, 2003.

[14] P. N. Gibson, Thin Films: Characterization by X-Rays, Article review, Materials Science and Materials Engineering, (2016).

[15] D. Wang, Fabrication and Characterization of ZnO Related Materials Thin Films for Optical Device Application, doctoral thesis, University of Technology Kochi, Japan, 2012.

[16] S. Ilican, Y. Caglar, M. Caglar, B. Demirci, Journal Of Optoelectronics And Advanced Materials, 10 (2008) 2592-2598.

[17] C. Gümü, O. M. Ozkendir, H. Kavak, Y. Ufuktepe, Journal Of Optoelectronics And Advanced Materials, 8 (2006) 299-303.

[18] F. Kermiche, A. Taabouche, F. Hanini, S. Menakh, A. Bouabellou, Y. Bouachiba, T. Kerdja, M. Bouafia, S. Amara And C. Benazzouz, SIPP 2011/UKM Algeria, (2011) 287-293

[19] S. Benramache, H. Ben Temam, A. Arif, A. Guettaf, O. Belahssen, Optik 125 (2014) 1816-1820.

[20] H. K. Juwhari, S. J. Ikhmayies, B. Lahlouh, International journal of Hydrogen energy, 42 (2017) 17741-17747.

[21] P. Reuter, Probing Inside a Scanning Electron Microscope, doctoral thesis, Graz university of technology, Austria, 2010.

[22] M. Mekhnache, A. Drici, L. S. Hamideche, H. Benzarouk, A. Amara, L. Cattin, J.C. Bernède, M. Guerioune, Superlattices and Microstructures, 49 (2011) 510-518.

[23] P. A. Rodnyi and I. V. Khodyuk, Optics and Spectroscopy, 111 (2011) 776-785.

[24] R.R. Salunkhe, C.D. Lokhande, Sensors and Actuators B, 129 (2008) 345-351.

[25] F. M. Sanda, M. E. Victor, T. A. Monica, C. Alina, Base Theory For Uv-Vis Spectrophotometric Measurements, Article review, University of Oradea Romania, 2012.

[26] M. M. Almotari, Fabrication and Characterisation of Zinc Oxide Thin Films Singly doped With Trace amounts of Rare Earth Materials, doctoral thesis, University of Canterbury, 2013.

[27] A. Hafdallah, F. Yanineb, M.S. Aida, N. Attaf, Journal of Alloys and Compounds, 509 (2011) 7267–7270.

[28] M. Caglar, Y. Caglar, S. Ilican, Journal Of Optoelectronics And Advanced Materials, 8 (2006) 1410-1413.

[29] V. Srikant and D. R. Clarke, J. Appl. Phys., 83(1998) 5447-5451.

[30] B. V. Rajendra, V. Bhat, D. Kekuda, International Journal of Emerging Technology and Advanced Engineering, 3 (2013) 82-85.

[31] U. Chaitra, D. Kekuda, K. M. Rao, j.ceramint, 43 (2017) 7115-7122.

[32] S. Ilican, Y. Caglar, M. Caglar, Journal Of Optoelectronics And Advanced Materials, 10 (2008) 2578-2583.

[33] F. Yakuphanoglu, S. Ilican, M. Caglar, Y. Caglar, Journal Of Optoelectronics And Advanced Materials, 9 (2007) 2180-2185.

[34] A.Q. Nguyen, G. Klysz, F. Deby, J.-P. Balayssac, Cement and Concrete Composites 83 (2017)308-322.

[35] R. Brennan and D. Dickey, Solid State Technology, 27 (1984) 125-132.

[36] F. M. Smits, Measurement of Sheet Resistivities with the Four-Point Probe, Bell Labs Technical Journal, 37 (1958) 711-718.

[37] K. Hayashi, S. Yamanaka, H. Okushi, and K. Kajimura, Applied Physics Letters 68(1996) 376-378.

[38] S. Faÿ, L'oxyde de zinc par dépôt chimique en phase vapeur comme contact électrique transparent et diffuseur de lumière pour les cellules solaires, doctoral thesis, Federal Institute Of Technology, Lausanne, 2003.

[39] M. Thomson, The Modification of Thin Film Surface Structure via Low Temperature Atmospheric Pressure CVD Post Process Treatment, doctoral thesis, University of Salford, United Kingdom, 2014.

[40] A. L. Allenic, Structural, Electrical And Optical Properties Of P-Type ZnO Epitaxial Films, doctoral thesis, University of Michigan, 2008.

Chapter III:
Results and Discussion for
(Ultrasonic study)

III.1.*Introduction:*

In the present chapter, the structural, optical and electrical properties of zinc oxide thin films were studied as a function of solution molarity and doping concentration of two different dopants (aluminium and indium), in order to find out the influence of Al and In doping rate on zinc oxide thin film properties.

III.2.*Chapter Objectives:*

The objectives of this chapter are:

1. Represent structural, optical and electrical properties discovered in the present study, as a patterns, picture and tables.
2. Interpretation and discussion this results.

III.3.*Molarity effect:*

Undoped Zinc oxide (ZnO) thin films have been deposited with various start solution molarities 0.05, 0.075, 0.1, 0.15, 0.2, 0.3, 0.4 and 0.5 $mol.l^{-1}$, with 350°C and 10min as substrate temperature and deposition time respectively (optimized by our group search), using ultrasonic spray pyrolysis technique onto glass substrates. The effects of start solution molarity on the crystallization behavior, optical and electrical properties of the films have been studied.

III.3.1. Structural Characterization:

To investigate the crystalline quality of ZnO thin films with various molarities, X-ray diffraction (XRD) analysis was carried out and the results are shown in FigIII.1. It shows the evolution of the solution molarity on structure quality of ZnO thin films. A matching of the observed of the (100); (002), (101) and (102) diffraction peaks confirms that the films exhibit polycrystalline structure that belongs to the hexagonal wurtzite type of ZnO [1, 2].

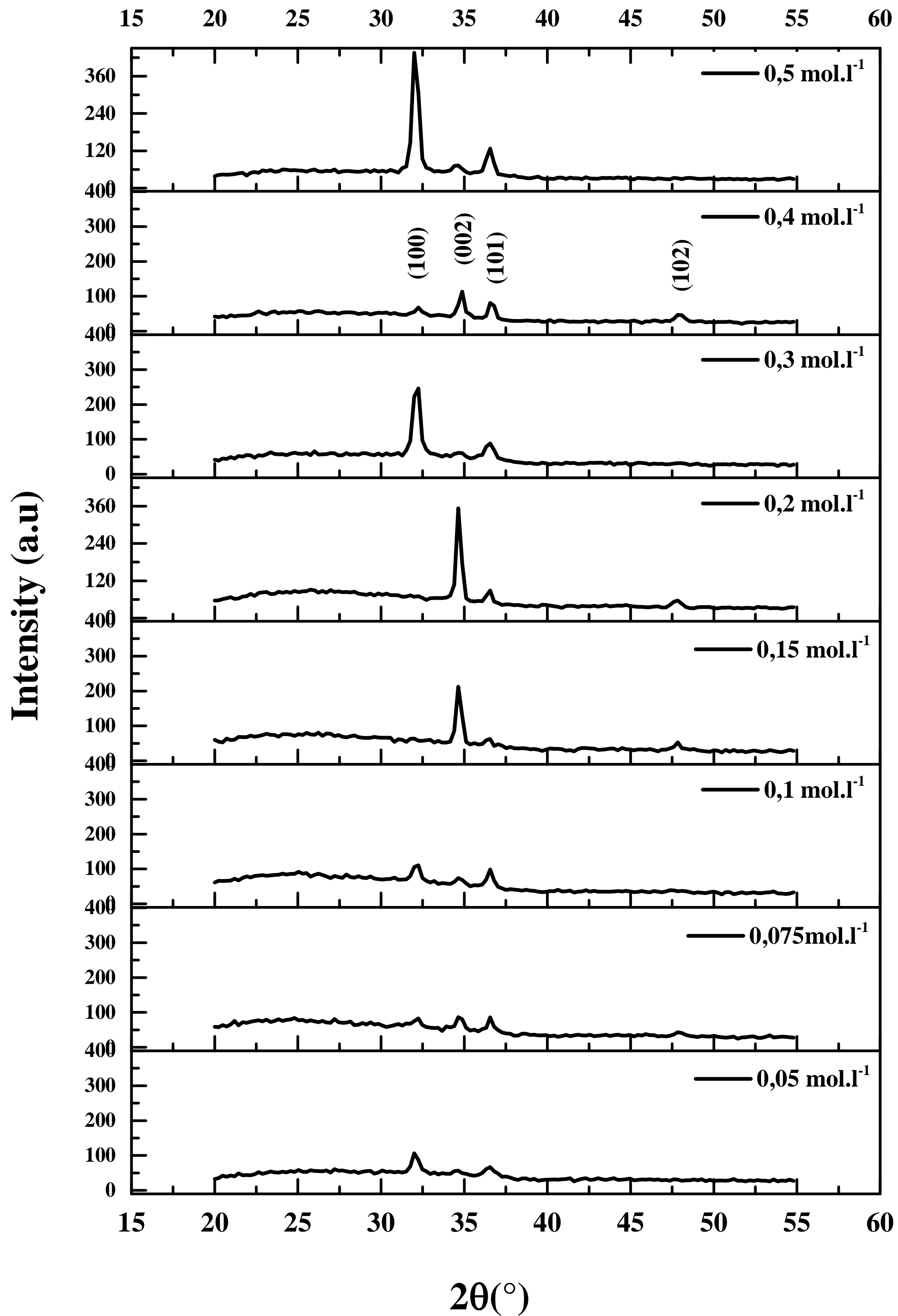

FigIII.1: X-ray diffraction spectra of ZnO thin films deposited at different solution molarities.

The obtained XRD spectra matched well with the space group P63mc (186) (No. 36-1451) of the wurtzite ZnO structure [1]. From analysis data, all deposited films have different orientations of ZnO films, which were strongly related to the higher intensity. The sharp diffraction peaks, frequently observed, indicate the good crystallinity of the prepared films. The diffraction peaks correspond to (100) and (002) planes indicate that the film have preferential a-axis and c-axis orientations, respectively.

III.3.1.1. The texture coefficient:

The texture coefficient was related to the atomic densities corresponding to that plane as X-ray intensities, which was corresponds to planer densities. The TC(hkl) values evolution of the four major peaks of the films shown in FigIII.2. The exact reason for this behavior of TC is decrease at (101) peak and increases at (100) and (002) peak at high solution molarity could be understood as follows; It is a well-known fact that the various factors such as crystallinity and morphology, the increases in the texture coefficient of (100) and (002) which results in reduced planer densities on (101), as discussed with [3], this is an increase of film thickness of ZnO thin films (see Fig III.5).

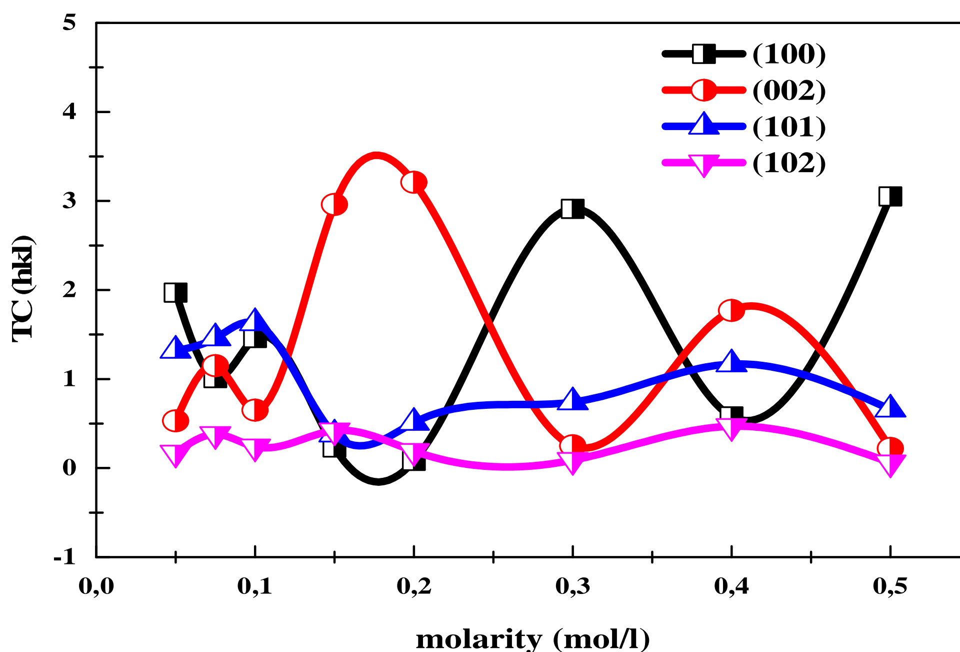

FigIII.2: The variation of the texture coefficient TC(hkl) of (100), (002), (101) and (102) peaks related to the solution molarity.

III.3.1.2.*Grain size determination:*

In order to attain the detailed structure information, the grains sizes G of (100) and (002) planes were calculated. FigIII.3 present the variation of crystallite size as a function of solution molarity, as can be seen, the crystallite size of (100) is inversely of the (002), which were varied in the range of 8 and 25 nm (see Tab III.1).

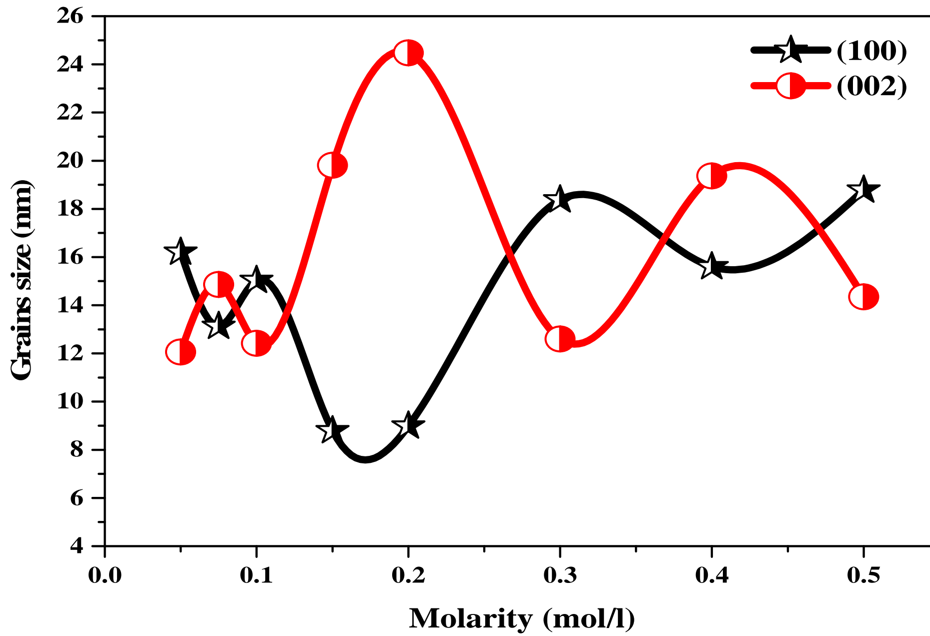

Fig III.3: The variation of grain size as a function of solution molarity related to (100) and (002) planes.

Tab III.1: Properties of ZnO films deposited by spray pyrolysis technique at different solution molarities.

Solution molarity ($mol.l^{-1}$)	G(nm) (100)	(002)	E_g(eV)	ΔE_g(eV)	E_u(meV)
0.05	16,204	12,060	3,265	–	0,09453
0.075	13,126	14,860	3,269	0.004	0,21616
0.1	15,035	12,420	3,268	–0.001	0,08301
0.15	8,7919	19,813	3,256	–0.012	0,06875
0.2	8,9885	24,475	3,264	0.008	0,07138
0.3	18,376	12,600	3,260	–0.004	0,06921
0.4	15,602	19,365	3,270	0.010	0,07887
0.5	18,782	14,347	3,224	–0.046	0,08424

Approximation the crystallite sizes of (002) plane is higher than the (100) plane, it can be see, the increase of the crystallite size of (002) plan has been indicated by the enhancement of the crystallinity and c-axis orientation of ZnO thin films [4]. So that the optimal values of the grain size of the ZnO films was obtained with (002) plane for solution molarities 0.15, 0.2 and $0.4 mol.l^{-1}$.

III.3.1.3.*Stress variation of ZnO thin films:*

The shift in the (002) peak position, according films XRD patterns, compared with the one from a stress free ZnO (powder) demonstrate that our films were under residual planar compressive stress. The stress values for ZnO films deposited in various start solution molarities are given in Tab III.2. FigIII.4 shows the evolution of stress and (002) peak position shift against the solution molarity.

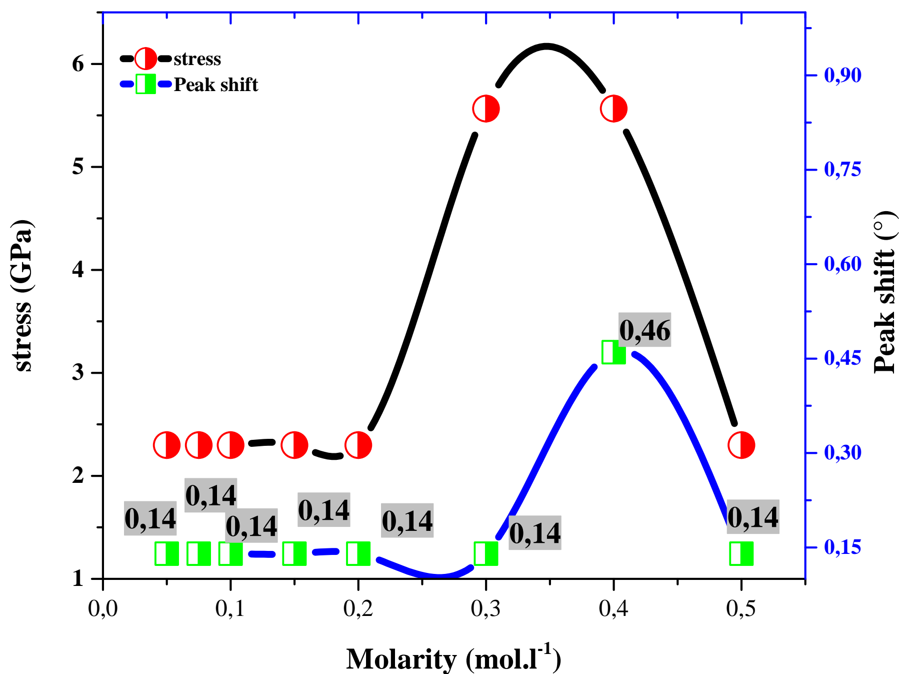

FigIII.4: The evolution of stress and (002) peak position shift against the solution molarity.

The stress is increased when solution molarity increases. The negative sign (positive for strain e_{zz}) indicates that the films exhibit a tensile stress. This stress usually consists of two parts: intrinsic stress, introduced by impurities, defects and lattice distortions in the crystal; extrinsic stress introduced by the lattice mismatch and thermal expansion coefficient mismatch between the film (ZnO $=4\times10^{-6} K^{-1}$) and substrate (glass $=9\times10^{-6} K^{-1}$) [5].

Tab III.2: results of undoped ZnO thin films deposited at deferent solution molarities.

Molarity ($mol.l^{-1}$)	(hkl)	d (A°)	C	e_{zz}	$C_{33\ film}$	σ (GPa)
0,05	(002)	2,5895	5,179	0,004995	213,0157	-2,299
0,075		2,5895	5,179	0,004995	213,0157	-2,299
0,1		2,5895	5,179	0,004995	213,0157	-2,299
0,15		2,5895	5,179	0,004995	213,0157	-2,299
0,2		2,5895	5,179	0,004995	213,0157	-2,299
0,3		2,5722	5,144	0,011631	218,7942	-5,565
0,4		2,5722	5,144	0,011631	218,7942	-5,565
0,5		2,5895	5,179	0,004995	213,0157	-2,299

III.3.1.4.*Film thickness calculation of ZnO thin films:*

The variation of film thickness with solution molarity is shown in FigIII.5, from which it is seen that film thickness of these films were found between 260 and 874 nm. However the film thickness shows mostly an increasing trend with molarity increases. Afterward the thickness decreases at high solution molarities.

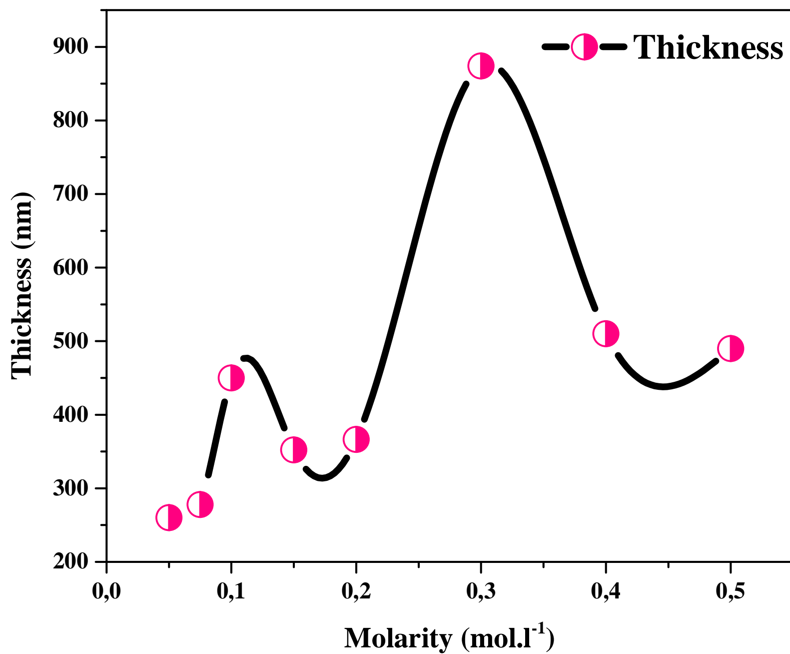

FigIII.5: The variation of film thicknesses of ZnO thin films deposited at different solution molarities.

The expected reason for thickness increment is supply of more number of ingredient ions with increase in solution molarity. This is in good agreement with those reported in literatures [6, 7]. At high molarity the film thickness heading towards decreasing which maybe due to the reorientation effect [7].

III.3.1.5.*Surface Morphology (Scanning electron microscope):*

Fig III.6 (a) and (b) shows the SEM morphologies of ZnO films deposited at 0,1 $mol.l^{-1}$ solution molarity.

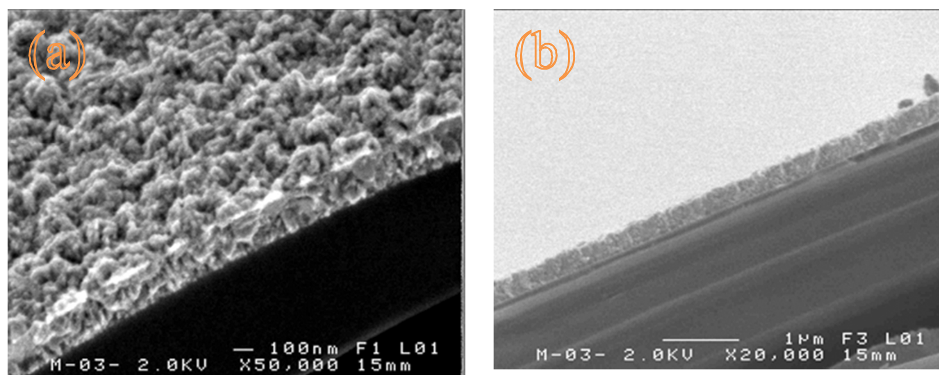

Fig III.6: (a and b) Scanning electron micrographs of ZnO thin films grown at 0,1 ($mol.l^{-1}$) solution molarity.

The microstructure of the films contains of many spherical grains uniformly distributed throughout the film surface. Indeed, the surface morphology of the ZnO film deposited at 0.1 $mol.l^{-1}$ shows a high density of small grains [8].

III.3.2.*Optical characterization (UV-Vis):*

The optical transmission measured as a function of the wavelength is depicted in FigIII.7; it shows the optical transmission spectra of the ZnO thin films deposited at different solution molarities. It may be mentioned that the optical transmission spectra recorded in the visible region are related to the electronic transitions, which are useful in understanding the electronic band structure of the semiconducting films [9, 10].

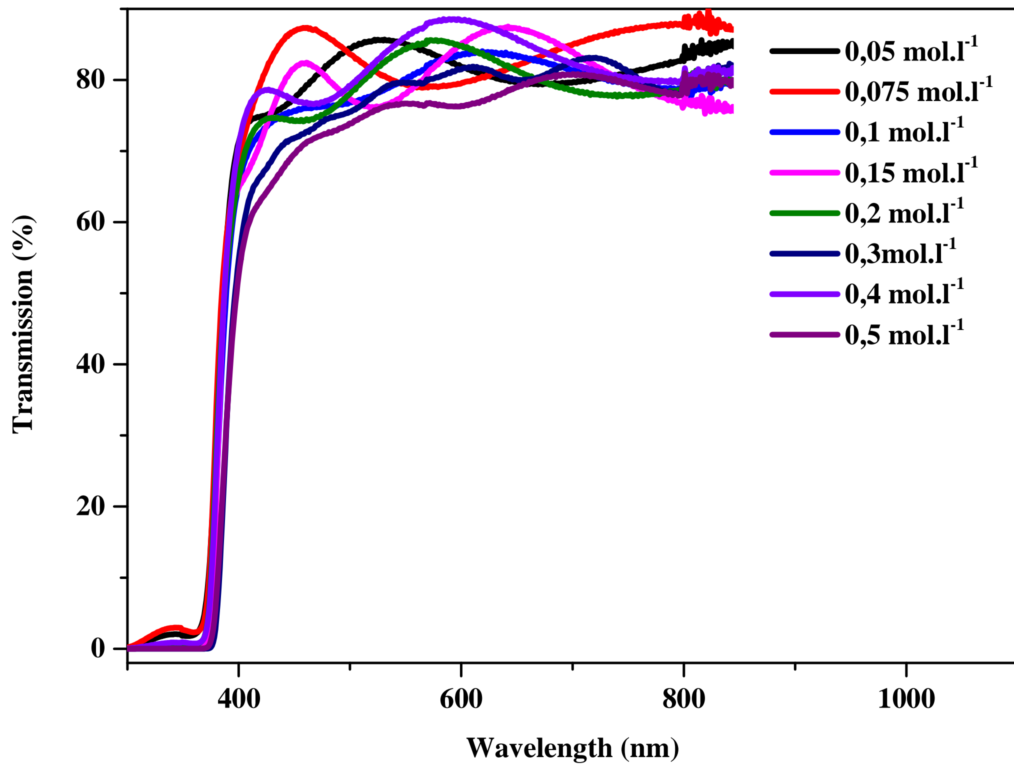

FigIII.7: Transmission spectra of ZnO thin films for different solution molarity.

For the longer wavelengths (λ >400nm) all the films become transparent, it is found that all the films show a high optical transmission, around 85%, in the visible region. The optical absorption at the absorption edge corresponds to the transition from valence band to the conduction band (around 375 nm), while the absorption in the visible region was related to some local energy levels caused by intrinsic defects. In this region found that the transmission decreased because of the onset fundamental absorption in the region between 370–395nm, as it was shown in the FigIII.7, it shows that the ZnO films reveal strong absorption bands at 370–390nm assigned to Zn–O bonding in wurtzite ZnO.

III.3.2.1.*Band gap energy and urbach energy:*

The optical band gap E_g was obtained by extrapolating the linear portion of the plot $(Ahv)^2$ versus (hv) to A = 0 (see FigIII.8) [11]. FigIII.9 shows the variation of the band gap energy Eg and the Urbach energy Eu as a function of the solution molarity. It is observed that the band gap energy of ZnO thin films in order to 3.27eV.

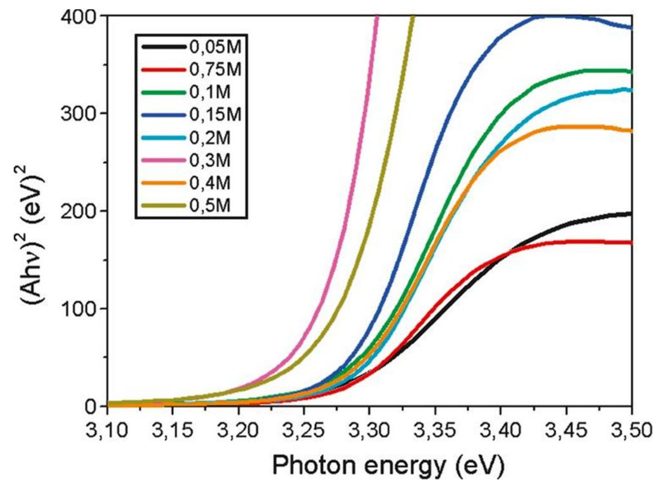

FigIII.8: The plot $(ahv)^2$ versus (hv) for the calculate the optical band gap energy Eg.

In general, the ZnO thin films showed a wider band gap energy as compared with the standard band gap energy of Eg=3.26eV reported for single crystal ZnO [12] and is comparable to the value of Eg=3.33eV reported for Cobalt doped ZnO films [13]. However, it was found that the optical band gap energy of the ZnO thin film decreased with increasing film thickness (see FigIII.5), which was related to the change in barrier height owing to change in crystallite size in polycrystalline films. The decrease in the Urbach energy is attributed to the decrease of the defects [14].

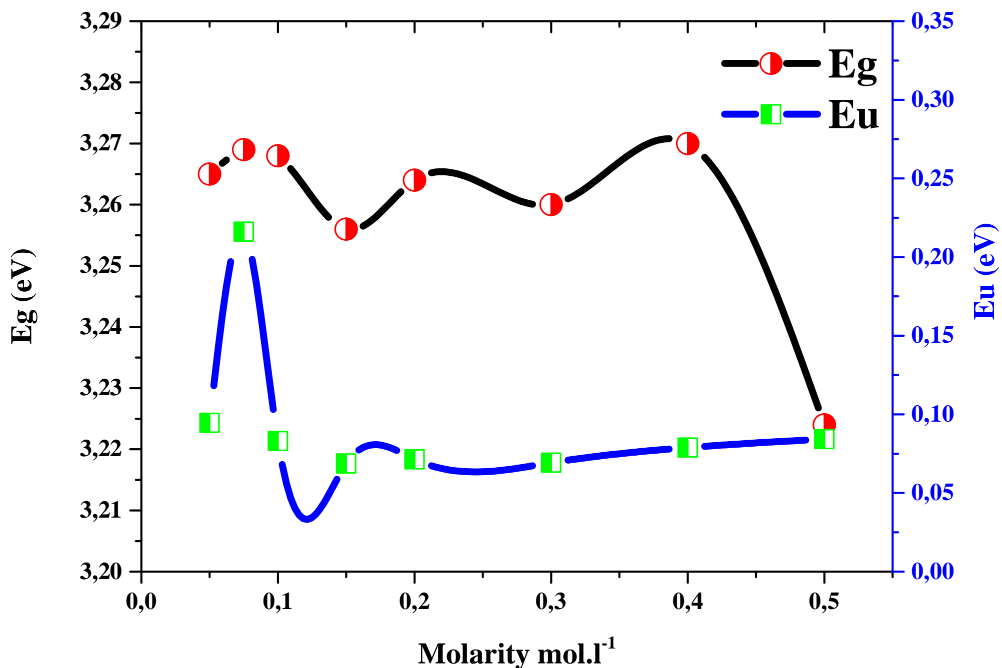

FigIII.9: The variation of the optical band gap Eg and Urbach energy Eu with solution molarity.

III.3.3.*Electrical characterization:*

III.3.3.1.*Resistivity of Zinc Oxide Films:*

FigIII.10 shows the variation of electrical conductivity of ZnO films at different solution molarities. Among all the ZnO thin films studied in the current work, the maximum value of electrical conductivity was 0.023×10^{-2} $(\Omega\text{-cm})^{-1}$ for the 0.075 $mol.l^{-1}$ with 278 nm film thicknesses. In this letter can be noted that the increase in electrical conductivity of the films has been explained by displacement of the electrons, which resulted in an increased carrier density [6].

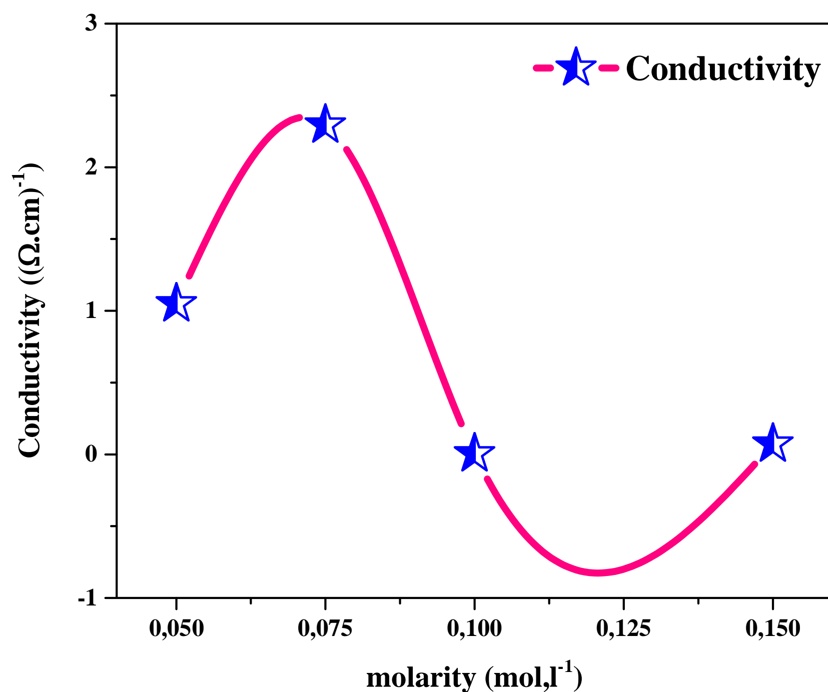

FigIII.10: The variation of electrical conductivity σ of ZnO thin films with solution molarity.

III.3.4.*In summary:* From the obtained results, for ZnO thin films deposited at deferent start solution molarity, following conclusions can be drawn:

1. The Whole undoped ZnO thin films exhibit polycrystalline structure that belongs to the hexagonal wurtzite type of ZnO, whereas the preferred growth orientation related strongly to the start solution molarity. The film thickness increases with molarity increment, then decreases at high molarities.

2. All the films show a high transparency, around 85%, in the visible region with absorption edge at hand 375 nm. The optical band gap decreases with solute molarity increment.
3. The max value of electrical conductivity was 0.023×10^{-2} $(\Omega\text{-cm})^{-1}$ for the 0.075 $mol.l^{-1}$ with 278 nm film thicknesses.

III.4. *Effect of dopants:*

Undoped and (Aluminium and Indium) doped Zinc oxide (ZnO) thin films have been deposited with various doping rates 1, 2, 3, 4 and 5 at%, at substrate temperature 350 °C, start solution molarity 0,1 $mol.l^{-1}$ and 0.5 $ml.min^{-1}$ solution flow rate, using ultrasonic spray pyrolysis technique onto glass substrates. In fact, these experimental conditions were selected based on the results obtained in the current work and the group search results. The effects of doping rate on the crystallization behavior, optical and electrical properties of the films have been studied.

III.4.1. *Effect of aluminium doping:*

In the present part we studied the effect of Aluminium doping concentration on doped ZnO thin films properties deposited using $Al(NO_3)_3$ (from sigma Aldrich with molar mass 375.1338 $g.mol^{-1}$) as dopant source.

III.4.1.1. Structural Characterization:

The XRD studies were carried out for thin films of Al-doped ZnO and were illustrated in FigIII.11 in order to get an idea about the structural changes produced in Al-doped ZnO thin films because of the Al doping rate increasing. The presence of diffraction peaks of Al doped ZnO emphasize the polycrystalline nature of the prepared films. The diffraction peaks appears around the angles 32, 34 and 36° which corresponding with diffraction planes (100), (002) and (101) respectively, see Tab III.3. The XRD data are indexed to the hexagonal wurtzite structure in conformity with the ICDD file 36-1451 witch confirm formation of Al doped ZnO. This indicates that the replacement of $Zn2^{+}$ with Al^{3+} ions does not change the hexagonal wurtzite structure [15]. An absence of Al and Al_2O_3 phases are observed due to the deposition of high purity Al doped ZnO thin films [16].

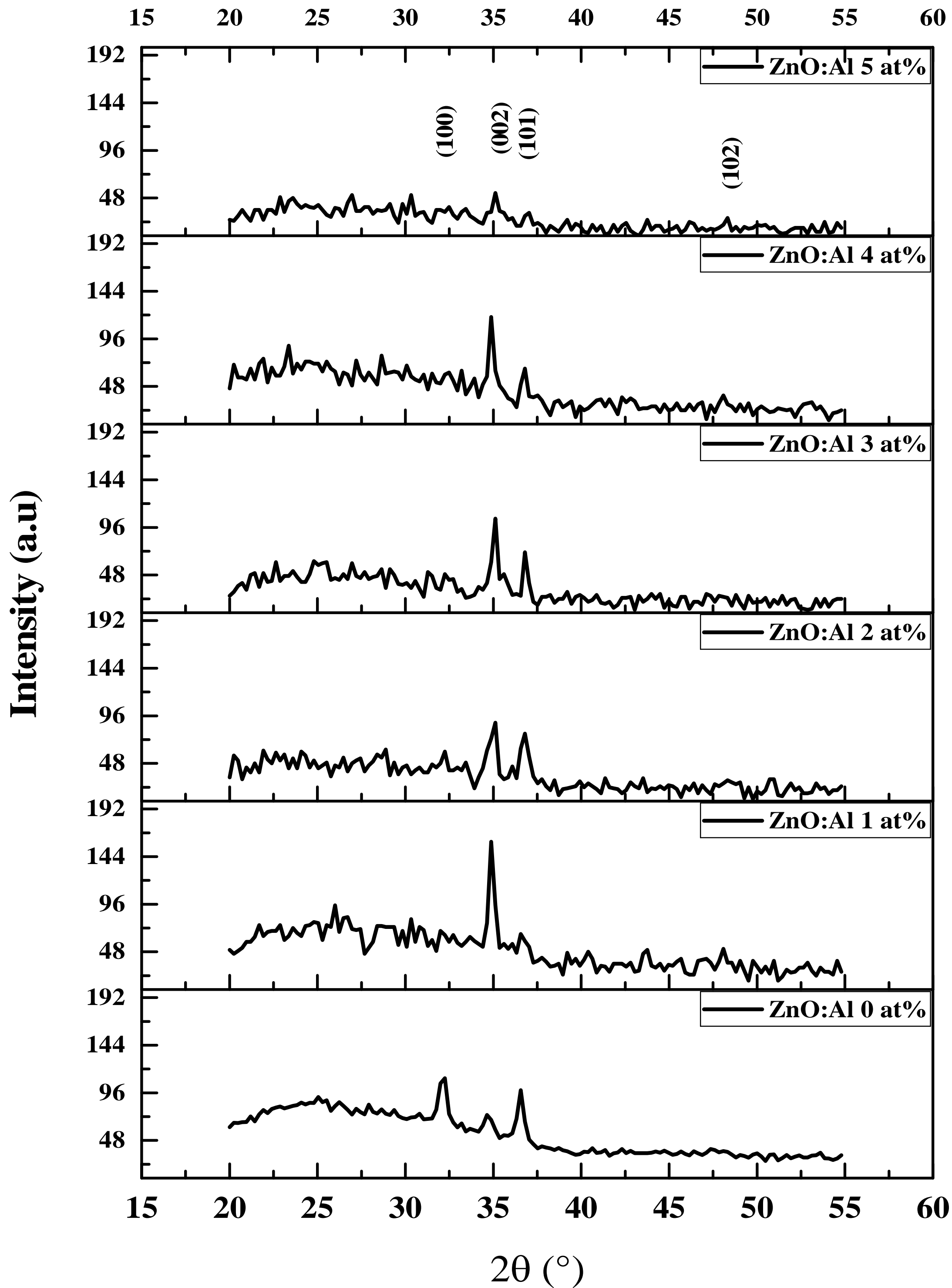

FigIII.11: XRD patterns of undoped ZnO and Al-doped ZnO with various Al doping rates.

Whole Al-doped ZnO thin films displayed an intensive hexagonal ZnO (002) plane, preferential orientation, this indicates that the c-axis of the grains become uniformly

perpendicular to the substrate surface [17]. Nevertheless, the appearance of any secondary phase means a decrease on the diffraction peak intensity of Al-doped ZnO thin films [18]. However, as the Al doping rate increases the diffraction peaks intensity decrease caused by the formation of stresses by the difference in ion size between Zn^{2+} and the Al^{3+} dopant atoms and the segregation of dopants in grain boundaries at high doping rates [19].

From Tab III.3 it was clear that the peak position corresponding to (002) plan was shifted to higher value of 2θ when aluminium incorporated, witch agrees very well with [20, 21, 19]. The increase of 2θ value of the (002) peak may be associated to the decrease of lattice parameters that comes from the oxygen defect or the strain caused by crystallization during the deposition process [20]. Noting that, the compressive stress causes the increase of lattice parameter d spacing, in this case the peak shifts to a lower angle compared with diffraction peak of bulk ZnO, while tensile stress causes decrease of the lattice parameter d spacing and thus peak shifts to a larger angle. Generally, the stress in the films is originated from thermal stress and intrinsic stress [22].

Tab III.3: peaks diffraction angles and FWHM of Al-doped ZnO films with different doping rates.

Al doping rate (at %)	2θ (°)	FWHM
0	34,64	0,37526
1	34,88	0,37526
2	35,12	0,62699
3	35,12	0,35454
4	34,88	0,38
5	35,12	0,38029

III.4.1.1.1.*The texture coefficient:*

The detailed analysis of the relative intensities shows variations in the preferential orientation, which can be clearly understood from the intensities of the diffraction peaks, the textural coefficients from all the films as a function of Al doping rates were presented in FigIII.12.

The calculated texture coefficients for (002) plane are in the range 1.6–2 indicative of selective orientations of crystallites in Al doped ZnO thin films as shown in the previous

figure. Which mean that the deposited Al-doped ZnO thin films have higher degree of orientation along c-axis.

The value of texture coefficients for (002) decreases as the film thickness or average crystalline size goes up, similar results were reported by Y. Wang et al. [23]. The (002) orientation is considered characteristic in Al-doped ZnO thin films [24]. For the undoped ZnO the most intense plane is along (100) plane, that are vertical plane, with respect to the normal as well as the (002) plane (FigIII.13.g) that is parallel to the normal.

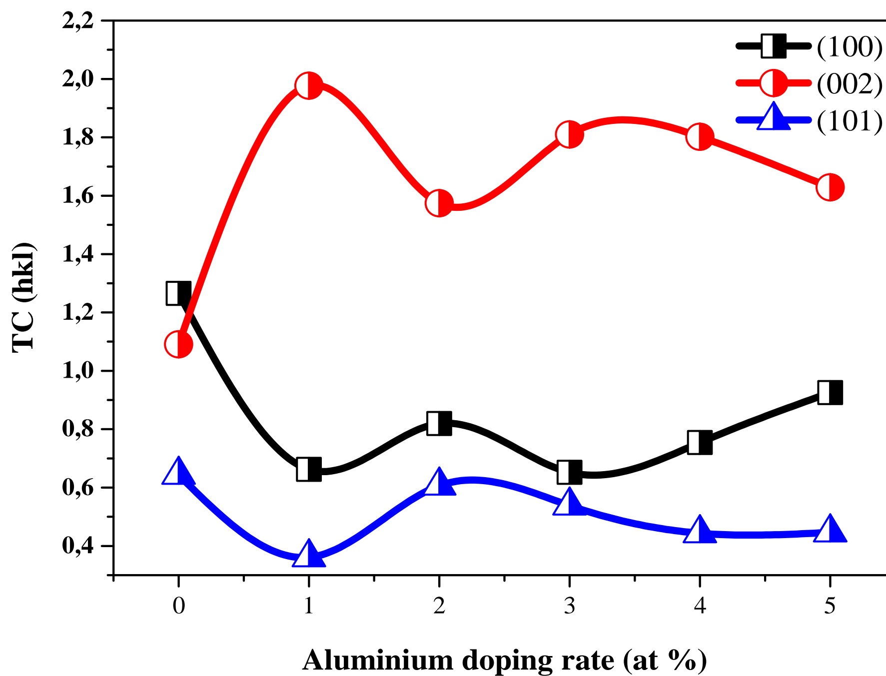

FigIII.12: The variation of the texture coefficient TC(hkl) of (100), (002) and (101) peaks with Al doping rate of ZnO thin films.

FigIII.13 presents simulated structures of ZnO, which explain the origin of the diverse morphology, namely plates (FigIII.13.a); pencils, either pointy or truncated (FigIII.13.b); hexagonal columns (FigIII.13.c) [25].

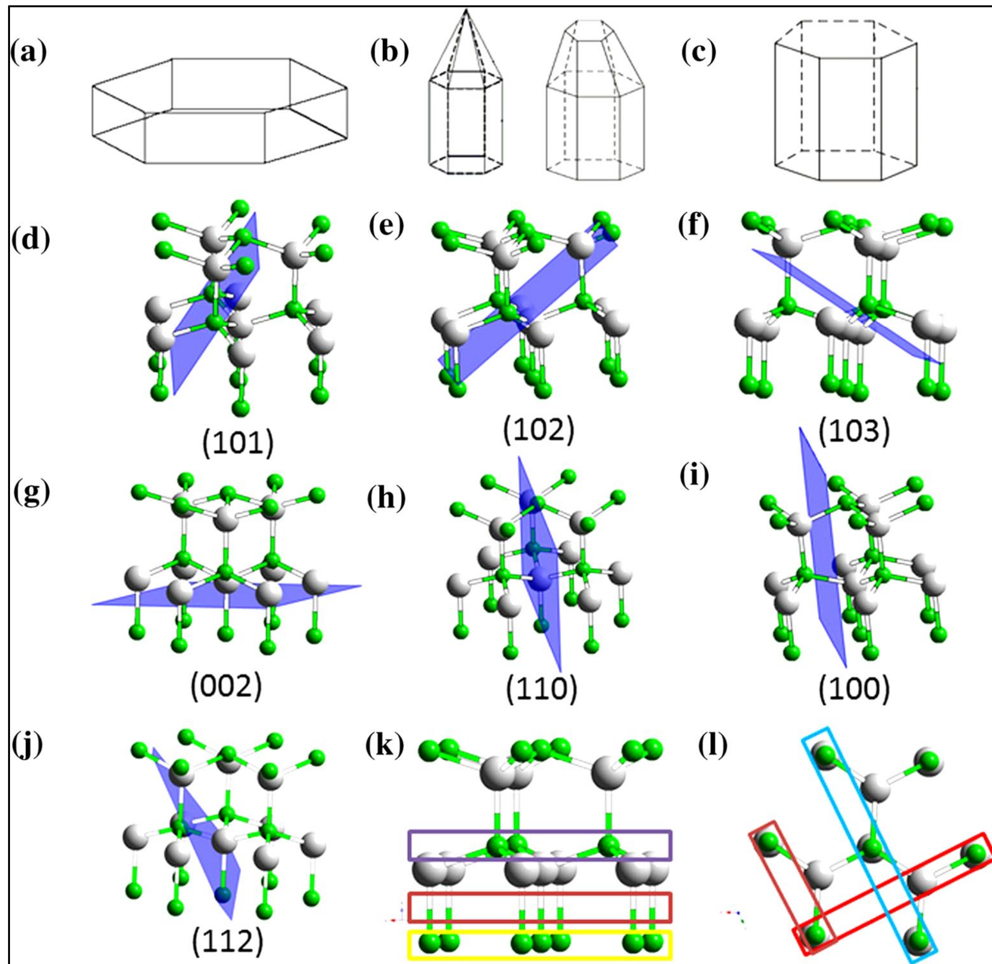

Fig III.13: a–c Idealized crystal habits of different ZnO structures; d–j projections of the crystallographic planes within the wurtzite structure; k, l scheme of the possible substitutional and interstitial sites to incorporate Al^{3+} ions.

III.4.1.1.2.*Grain size variation of Al-doped ZnO thin films:*

The FigIII.14 shows the grain size as a function of the aluminium doping rate; our thin films exhibit a strong relation between the growth process of the grain and the doping rate. Tab III.4 displays Diffraction angle, FWHM and Grain size of ZnO films deposited at different Aluminium doping rates.

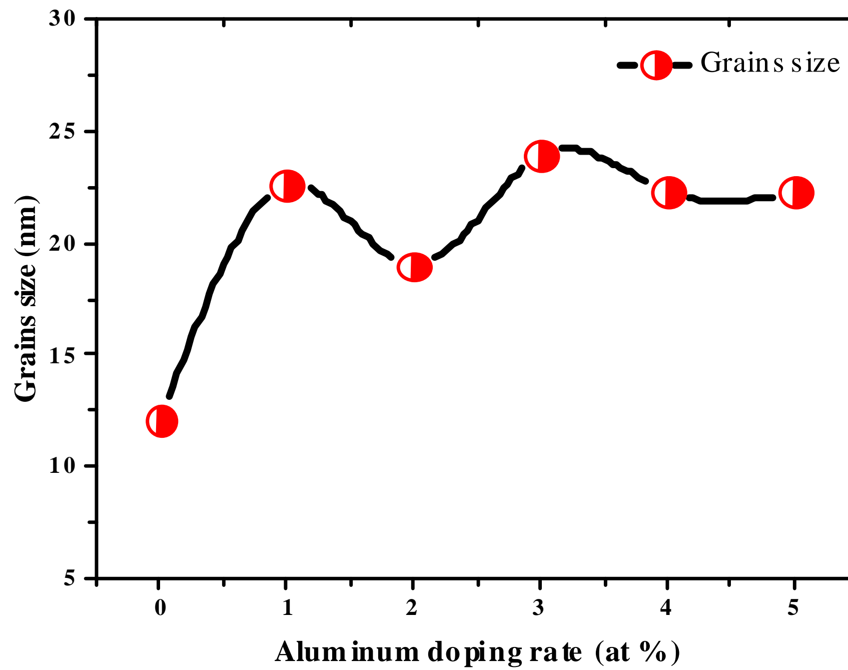

FigIII.14: The variation of grain size of Al doped ZnO thin films.

Tab III.4: Diffraction angle, FWHM and Grain size of ZnO films deposited at different Aluminium doping rates.

Al-doping rate (at %)	(hkl)	2θ (°)	FWHM	Grain size (nm)
0	**(002)**	34,64	0,70246	**12,060**
1		34,88	0,37526	**22,590**
2		35,12	0,62699	**19,008**
3		35,12	0,35454	**23,926**
4		34,88	0,38	**22,308**
5		35,12	0,38029	**22,306**

As clear, the grain size increase slightly when Al concentration increases, whereas the majority of the researchers have reported a marginal decrease in grain size due to Al incorporation [27, 28, and 29]. Rakhshani [30] has reported that Al-doping does not modify the size of the grains. In all these researches Scherrer equation was applied to evaluate the grain size which only takes account of particle size broadening according S. Mondal and Al

[31]. Another equation can be used to evaluate grain size, the W–H equation, thus gives much more reliable results compared to Scherrer equation. Where, the grain size increasing was explained by Al-doped films thickness enhancement observed in this work. This behavior can be also attributed to the various relationships between the nucleation, growth and activation energy of the thin films (presence of slight strain and dislocations in the ZnO lattice due to the Al incorporation) [32]. K. Bahedi et al. [33] has reported that Al-doped ZnO films exhibits a strong grains size, what increases with Al doping rates increment.

III.4.1.1.3. Stress variation of Al-doped ZnO thin films:

The curve of the stress described in FigIII.15, as well from figure of X-ray diffraction we observed that there is a variation of the position of (002) peak from 34.64° to 35.12°, higher angle side toward compared to value of bulk ZnO. This means that stresses induced in our Al doped ZnO thin films are tensile stress [24].

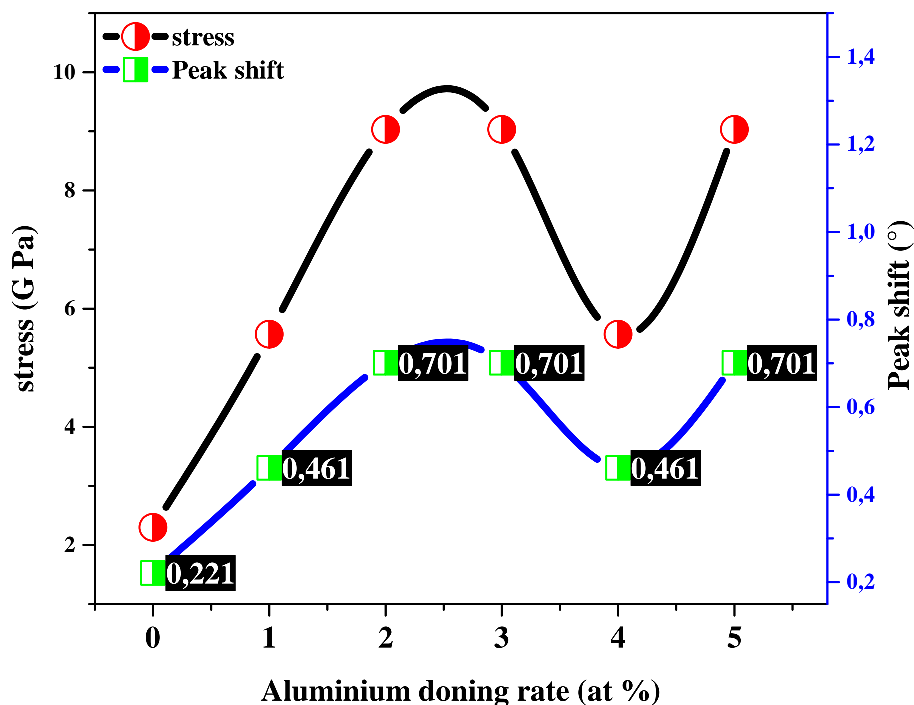

FigIII.15: The variation of stress and peak position shift of ZnO doped with different Al concentrations.

Results of the whole samples are given in the Table III.5. When Al was doped into a ZnO structure, the ZnO lattice was also distorted owing to the difference between the ionic radius of Al^{3+} (0.054 nm) and Zn^{2+} (0.074 nm) what explains the stress increase with increase

of Al concentration [33]. The small stress of the films doped with 1and 4 at% of aluminium indicates that the texture of the films is better which is in agreement with the XRD diffraction. The mismatch between the crystalline film (undoped and Al doped ZnO) and the amorphous substrate (glass in the present work) ascribed to the difference in the thermal expansion coefficients and/or from defects and lattice distortions in the crystal, can be also the stress origin [34, 35].

Table III.5: results of the whole Al doping ZnO thin films

Al-doping rate (at %)	(hkl)	d(A°)	C	e_{zz}	$C_{33\ film}$	σ (GPa)
0	**(002)**	2,570	5,1790	0,0050	213,0157	**-2,299**
1		2,572	5,1445	0,0116	218,7942	**-5,565**
2		2,555	5,1104	0,0182	224,6855	**-9,033**
3		2,555	5,1104	0,0182	224,6855	**-9,033**
4		2,572	5,1445	0,0116	218,7942	**-5,565**
5		2,555	5,1104	0,0182	224,6855	**-9,033**

III.4.1.1.4.*Film thickness calculation of Al doped ZnO thin films:*

Using the cross sectional SEM images, presented in FigIII.17 the thicknesses of Al doped ZnO thin films are observed between 250 nm and 390 nm.

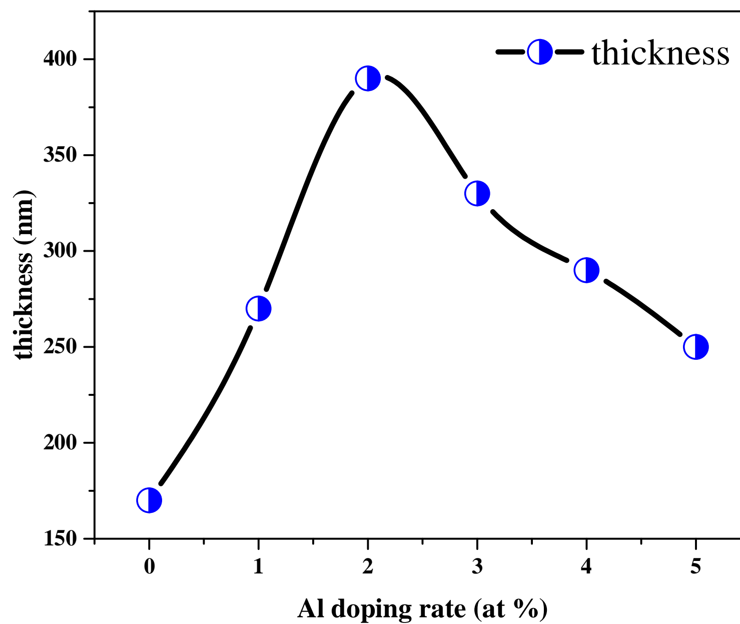

FigIII.16: thickness variation of Al doped ZnO thin films.

It is clear that the aluminium incorporation has a strong effect on the thickness increment, whereas the increasing in Al ions due to the increment in the concentration of aluminium [36] that leads film thickness taking a highest value 390 nm at 2 at% of Al doping.

When Al rate is greater than 2 at% the film thickness decreases. Noting that, whereas the doping rate is equal to 3 at%, 4 at% and 5 at%, the (002) peak intensity decreases. The film thickness decreases also respectively by a factor of 60, 40 and 40 nm. So, this disparity between the decrease in the peak intensity and the decrease in the film thickness clearly indicates that the changes observed are indeed the results of structural changes caused by the aluminum doping [37].

F.A. Garcés et al [38] were reported that the changes in the film thickness can be explained by the transformation of growth model. During the deposition of thinner films, the film growth approximately following a 2D model. While, as thickness increases the film tend to grow following a 3D model.

III.4.1.1.5.*Surface Morphology (Scanning electron microscope):*

FigIII.17 shows the surface morphologies of pure ZnO and Al-doped ZnO deposited by ultrasonic spray pyrolysis. Scanning microscopy observations were used to analyze morphology of the studied samples and determining the films thickness using cross sections. The micrographs show a very good crystallization with a well-defined hexagonal character for the whole samples.

As we can see, the grains fully cover the substrate surface uniformly (FigIII.17 a and b). However, undoped ZO film shows particles with irregular, maybe spherical, shape. Thus, Al doping seems to have modified the shape of the grains, which turned into pyramids (FigIII.17 e and FigIII.18 a). The microstructure is found to be uniform with compact connected grains. E. P. da Silva [39] found that surface roughness increases with increasing Al concentration in ZnO as found in the present work. Moreover, the film became denser with Al incorporation.

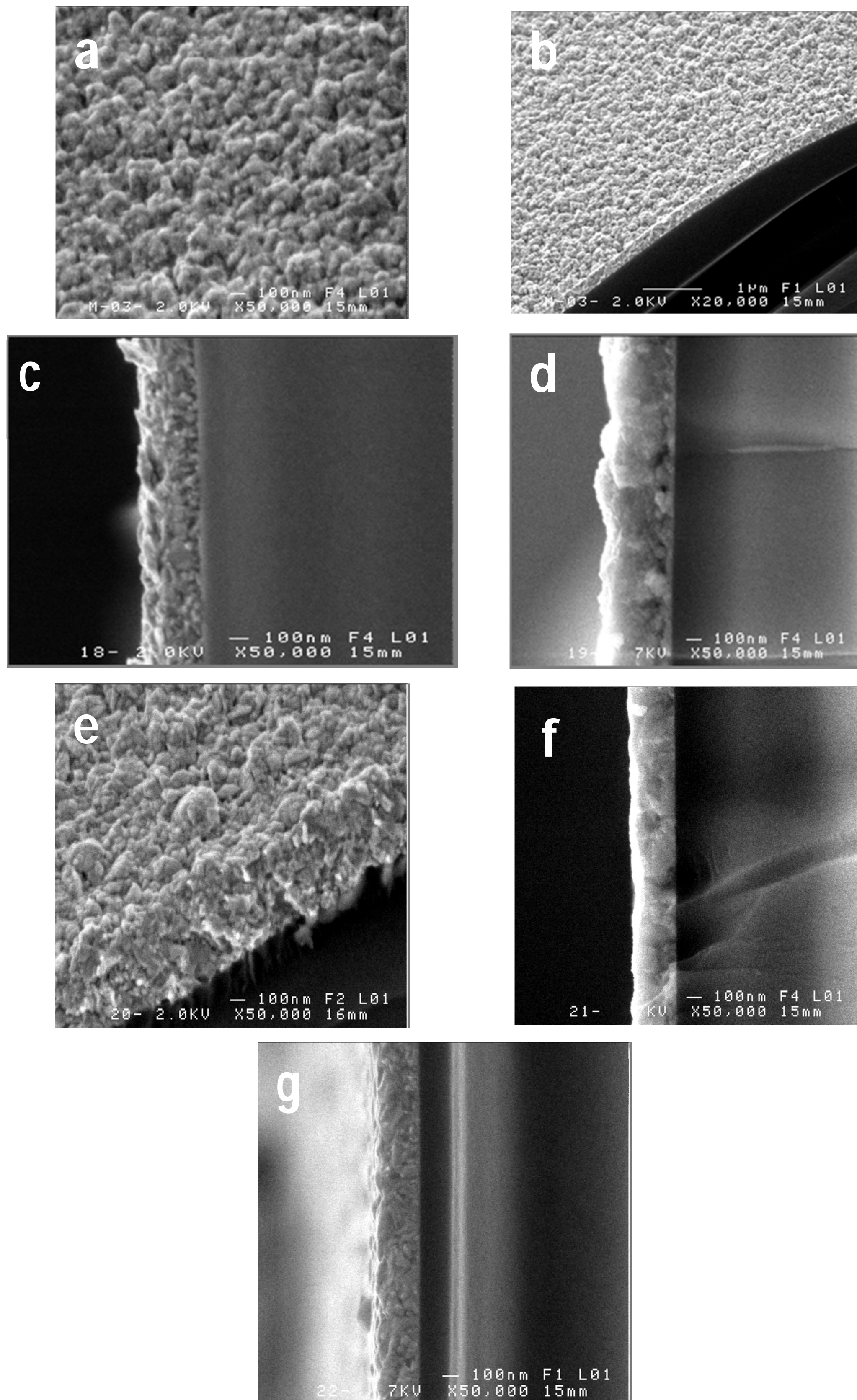

FigIII.17: SEM surface and cross section micrographs of Al-doped ZnO films prepared with various doping rates (a and b) undoped ZnO, (c, d, e, f and g) present Al concentration 1, 2, 3, 4 and 5 at % respectively.

FigIII.18 allows seeing the similar surface morphology of our Al-doped ZnO films with 3 at% and two other Al-doped ZnO films prepared by spray pyrolysis at doping rates 0.5 and 2.5 at% respectively.

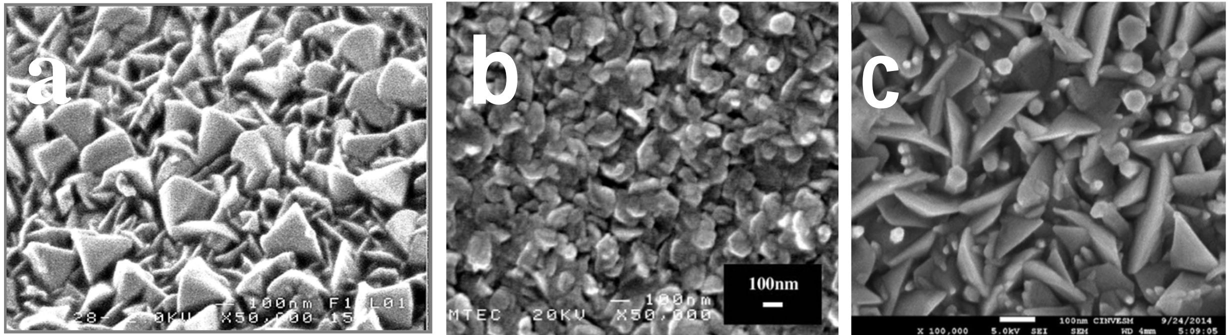

FigIII.18: SEM surface Micrograph of our films Al-doped ZnO at 3 at% (a), (b) Al-doped ZnO (0.5 at%) deposited by spray pyrolysis [40], (c) Al-doped ZnO (2,5 at%) ultrasonic spray pyrolysis [25].

III.4.1.1.6.*The Energy X-ray Dispersive Spectroscopy (EDS):*

To assess the elemental composition of the synthesized undoped ZnO and Al-doped ZnO thin films, the Energy X-ray Dispersive Spectroscopy (EDS) was done and the result is shown in FigIII.19. It reveals that Zn and O elements were contained in the deposited films. Trace amounts of S, Na, Mg, K and Ca are also detected in the film as impurities, as well as O, Si, Ca, K from the glass substrate [25]. Others may be from water, substrate cleaning agents or from the based layer of the Spray process chamber [41]. The high intensity of the Zn and O peaks suggest that the sample mainly contains ZnO.

The main purpose of using this technique (EDS) is the existence confirmation of the Aluminium. All the spectra show the presence of this element, coming from the doping and we notice an increase in the percentage of Al with doping rate increment.

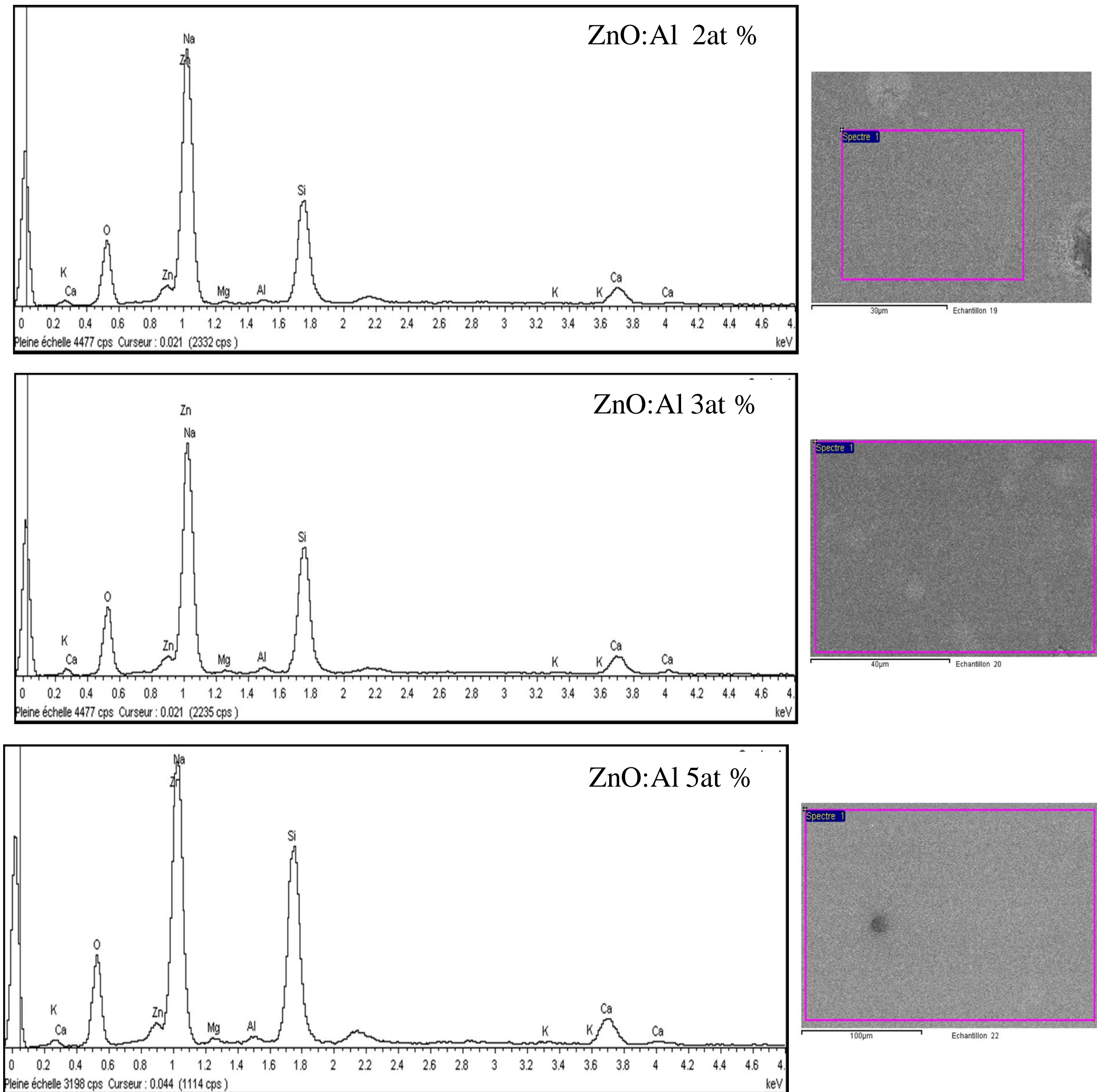

FigIII.19: Energy X-ray Dispersive Spectroscopy spectra of four samples of Al doped ZnO at 2, 3 and 5 at %.

III.4.1.2. Optical characterization (UV-Vis):

We have investigated the transmittance of the ZnO thin films grown with different Al doping rates in the range of 300–1000 nm. The transmittance spectra are reported in FigIII.20. The transmittance of Al doped ZnO thin films decreased with a sharp fundamental absorption edge at around 375 nm of the wavelength.

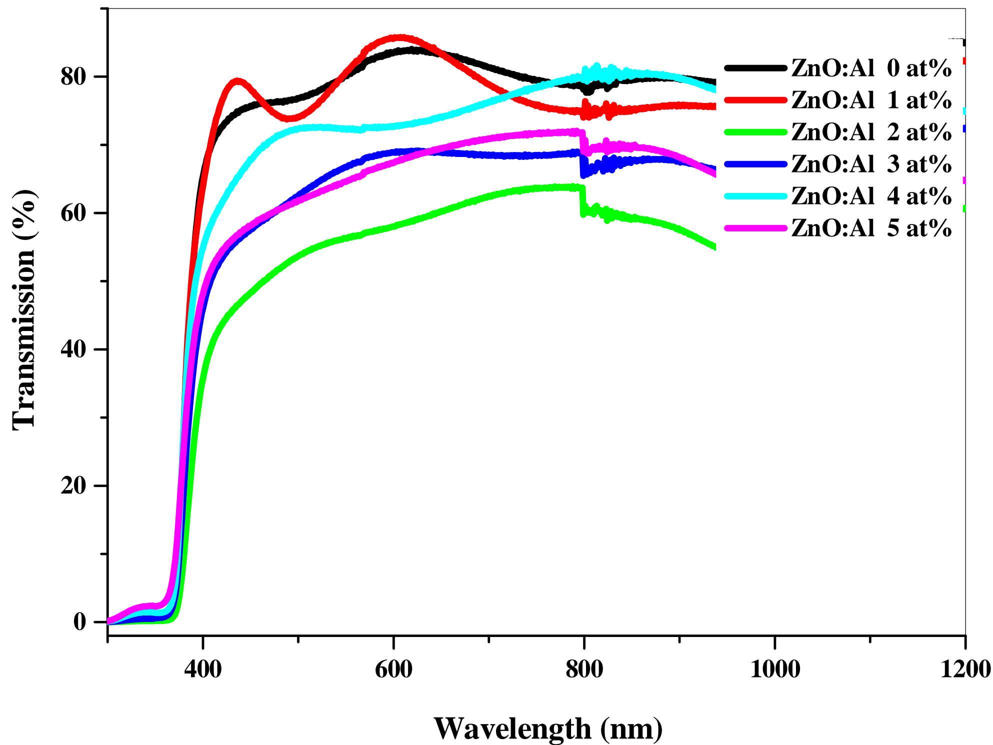

FigIII.20: Variation of the transmittance of the ZnO films doped with Al depending on the wavelength.

All the films, in the visible range, present a high average transmittance bigger than 60%, except the film of ZnO doped with 2 at %, where we observe transmittance greater than 50%, which is the thicker film (see FigIII.16). The spectrum shows a maximum transparency higher than 80% at wavelength around 600 nm for undoped ZnO and ZnO doped with Al rate of 1 at%. However, the transparence reduced with Al doping rate increasing. This is due to free carriers coupling to the electric field hence increasing the reflection [42]. E. Bacaksiz et al. [43] reported significantly reduced transmission when ZnO was doped with higher percentages of Aluminum. Noting that, the reduction of optical transmittance is also related to the crystallinity of the film [44].

III.4.1.2.1.*Band gap energy Urbach energy:*

From the location of the absorption edge of about 350 to 400 nm, the optical energy gaps appeared in the range of 3.25 to 3.27 eV for ZnO and the Al-doped ZnO thin films. The

variation of direct band gap for different Al doping concentration is shown in FigIII.21. The transmittance reduces also led to variation in band gap. This may be attributed to the Oxygen vacancies and the behavior of free carrier's concentration with Al incorporation [42].

While ZnO doped with 1 at% the energy gap decreases strongly from 3.267 eV to 3.253 eV (see Tab III.6), this decrease might be explained in terms of electron concentration dependence of band gap shift in the Al-doped ZnO thin films [43].

An obvious increase in the band gap was observed, the energy gap Eg increased when the Al concentration was increased up to 4at% then decreased when the Al doping was greater than 4 at%, this behavior has been indicated by other authors [45, 46].

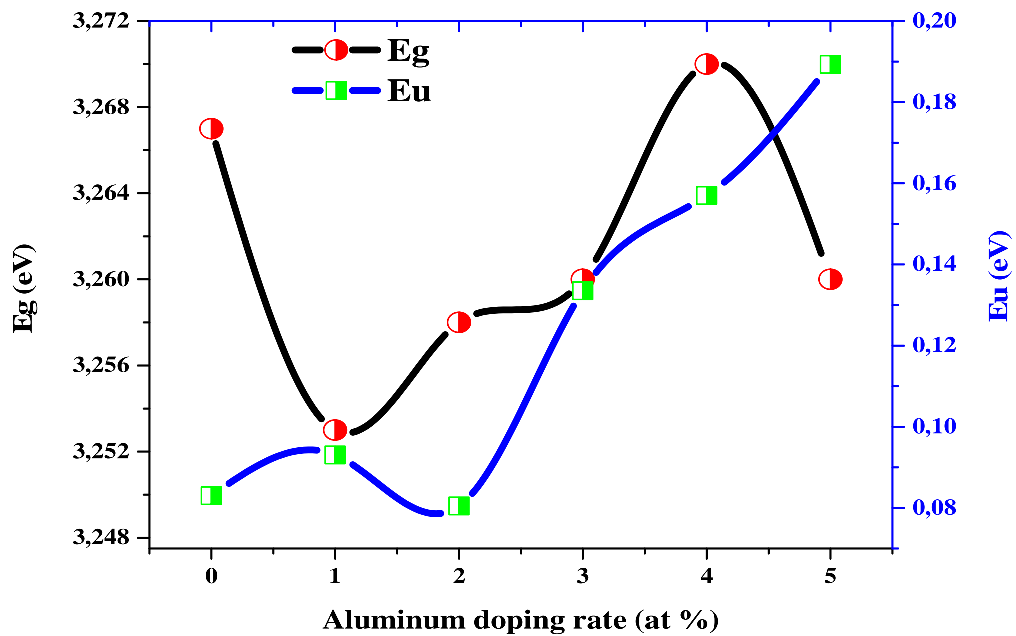

FigIII.21: The variation of optical band gap and Urbach energy of ZnO films doped with different Al concentrations.

Typically, the energy gap increases of the Al-doped ZnO thin films is associated with an increase of the carrier concentration blocking the lowest states in the conduction band, which is well known as the Burstein-Moss effect [47]. The required electronic conduction in Al doped ZnO films is due to itinerant electrons induced by substitution of Al for Zn in the lattice as well as carriers derived from oxygen vacancies. For carrier concentrations above the

critical Mott density, the free electrons are able to occupy the ZnO conduction band, and a subsequent widening of the band gap is typically observed [48].

As clearly seen too, the urbach energy increased slightly with Al doping rate increases, indicating the reduction of structural disorder and defects in the Al doped ZnO thin films.

Tab III.6: calculated optical band gap and Urbach energy of undoped ZnO thin films.

Al-doping rate (at%)	Eg (eV)	Eu (eV)
0	3,267	0,083
1	3,253	0,093
2	3,258	0,081
3	3,26	0,134
4	3,27	0,157
5	3,259	0,189

III.4.1.3.*Electrical characterization:*

III.4.1.3.1.*Resistivity of Al-doped ZnO thin Films:*

For the applicability of the produced Al-doped ZnO thin films to photovoltaic devices, the knowledge of electrical parameters like electrical conductivity and resistivity are highly important and necessary. FigIII.22 presents the electrical conductivity (as well as resistivity) of the Al-doped ZnO thin films as a function of the Al content, where we can observed that the highest electrical conductivity was achieved with the Al concentration of 3 at% corresponding to a conductivity of $6{,}17\times10^{2}$ $(\Omega.cm)^{-1}$, as tabulated in the Tab III.7. However, the conductivity increases up to 3 at% Al doping rate, after wards decrease slightly.

This increase of electrical conductivity, thus decreasing resistivity, with increasing Al content into ZnO lattice can be ascribed to the abundance number of free electrons in the ZnO lattice arising from the Al ions. This implies that the Al ions in the ZnO lattice are acting as a charge carriers reservoir and acceptor impurities [49]. R. R. Kothawale and R. M. Mohite [50] have reported that the electrical resistivity depends on grain size; it increases with increase in grain size.

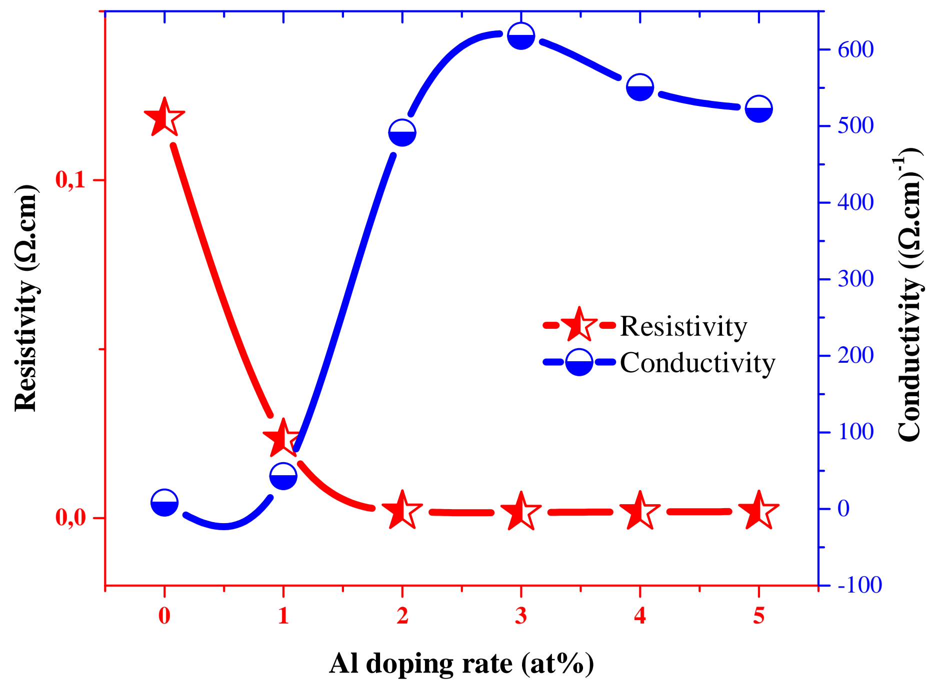

FigIII.22: The variation of electrical conductivity with atomic doping rate of aluminium.

With further increase in Al concentration the conductivity value started to decrease slightly. Beyond a certain doping concentration, a decrease in conductivity has been reported [51]. In this case, the doping atoms do not occupy the lattice sites but instead result in some kind of defects, precisely in grain boundaries. Thus, there is a segregation of dopant atoms at the non-crystalline regions which produces disorder in the lattice. These defects act as scattering centers giving rise to various scattering mechanisms resulting in a decrease in conductivity [31].

Tab III.7: measured electrical resistivity and conductivity of Al-doped ZnO thin films deposited with varied doping rates.

Al-doping rate (at%)	Thickness (nm)	I (°A)	U (Volt)	Resistivity (Ω.cm)	Conductivity $(\Omega.cm)^{-1}$
0	170	0,03	20	0,1183	8,45
1	270	0,03	2,48	0,0233	42,93
2	390	0,03	0,15	0,0020	491,39
3	330	0,03	0,141	0,0016	617,80
4	290	0,03	0,18	0,0018	550,69
5	250	0,03	0,22	0,0019	522,66

In the Tab III.8 we show a comparison between the electrical conductivity, the carrier's concentration and transmission values of our Al doped ZnO thin films deposited by ultrasonic spray and those obtained by different deposition methods.

Noting that, based on the Hall Effect measurements performed on Al-doped ZnO the type of carrier is found n-type with carrier concentration of the order of 10^{21} cm^{-3}.

Tab III.8: The electrical and optical properties of Al-doped ZnO thin films.

	Deposition technique	electrical conductivity $(\Omega.cm)^{-1}$	carriers Concentration (cm^{-3})	Transmission (in visible range)	ref
Al doping ZnO	Ultrasonic Spray	3.4	10^{21}	> 60	Our films
	Ultrasonic Spray	0.01-0.17	--	--	[52]
	Ablation laser	10-140	--	--	[53]
	Sputtering	10^{2}	$4.7x10^{20}$	90	[54]
	Sputtering	$4x10^{3}$	$8.0x10^{20}$	--	
	Sputtering	$4x10^{3}$	10^{21}	--	
	Sputtering	$7x10^{3}$	10^{21}	--	

III.4.1.4.*In summary*: From the obtained results, for Al-doped ZnO thin films, following conclusions can be drawn:

1. Whole Al-doped ZnO thin films displayed an intensive hexagonal ZnO (002) plane, this later intensity decreases with Al incorporation. Doping ZnO films by Al improves the crystallites size with increased stress. The film thickness enhanced then decreased at higher Al rates under the effect of structural changes. The SEM analysis shows that the Al doping change the grain shape and make the film denser.
2. All the films, in the visible range, present a high transparency mostly bigger than 60%, which reduced when the Al-doping rate increases with a sharp absorption edge at around 375 nm. The optical energy gaps appeared in the range of 3.25 to 3.27 eV.
3. The electrical conductivity increased with Al incorporation. The highest value was achieved at 3 at% of Al doping rate ($6,17\times10^{2}$ $(\Omega.cm)^{-1}$).

III.4.2.*Effect of Indium doping:*

In this part we studied the effect of Indium doping concentration on doped ZnO thin films properties deposited using ultrasonic spray pyrolysis and $In(NO_3)_3.xH_2O$ (from sigma Aldrich with molar mass 390,91 g.mol^{-1}) as dopant source.

III.4.2.1.*Structural Characterization:*

The analysis of our samples by X-ray diffraction was obtained for undoped and In- doped ZnO thin films at different concentrations of Indium (FigIII.23). The whole prepared films are polycrystalline with a hexagonal würtzite structure of ZnO, which is confirmed by the presence of set diffraction peaks. The diffraction peaks appears around the angles 32, 34, 36, 47 and 62° which corresponding with diffraction planes (100), (002), (101), (102) and (103) respectively. There is no peak corresponding with In, suggesting that the replacement of $Zn^{2+}$with In^{3+}ions does not change the hexagonal wurtzite structure [15, 55].

As we can see, while the In doping rate goes up the (002) peak intensity decrease strongly accompanied by an increase in the (100) peak intensity, although the (101) peak intensity almost unchanged. This mean that higher concentration of In is responsible for the preference of (100) crystal formation over (002) plane. We can further argue that In incorporation may induce more homogeneity in the crystal structure [56]. Noting that, the appearance of diffraction peaks corresponding with (102) and (103) planes was only in undoped ZnO.

For undoped ZnO, 1 at% and 2 at% concentration of In the dominant diffraction peak was (002) which mean that the films have a c-axis preferred growth orientation, normal to the substrate. For 3 at% and 4 at% concentration of In the crystal undergo reorientation, with the (100) orientation preferred and (002) peak intensity decrease. In the In 2 at% sample, the (100), (002) and (101) diffraction peaks are approximately equal, showing that the film is composed of grains with various orientations [57]. The disappearance of the diffraction peaks may return to the structural deterioration phenomenon which is observed for Indium concentrations 5 at%. So, at higher doping level insoluble In atoms segregate at the grain boundaries inhibit the growth of In-doped ZnO crystals [58]. It is clear from XRD patterns that as the In content increased the film adopts a preferred orientation, with the c-axis (002) which changes above 2 at% to become (100).

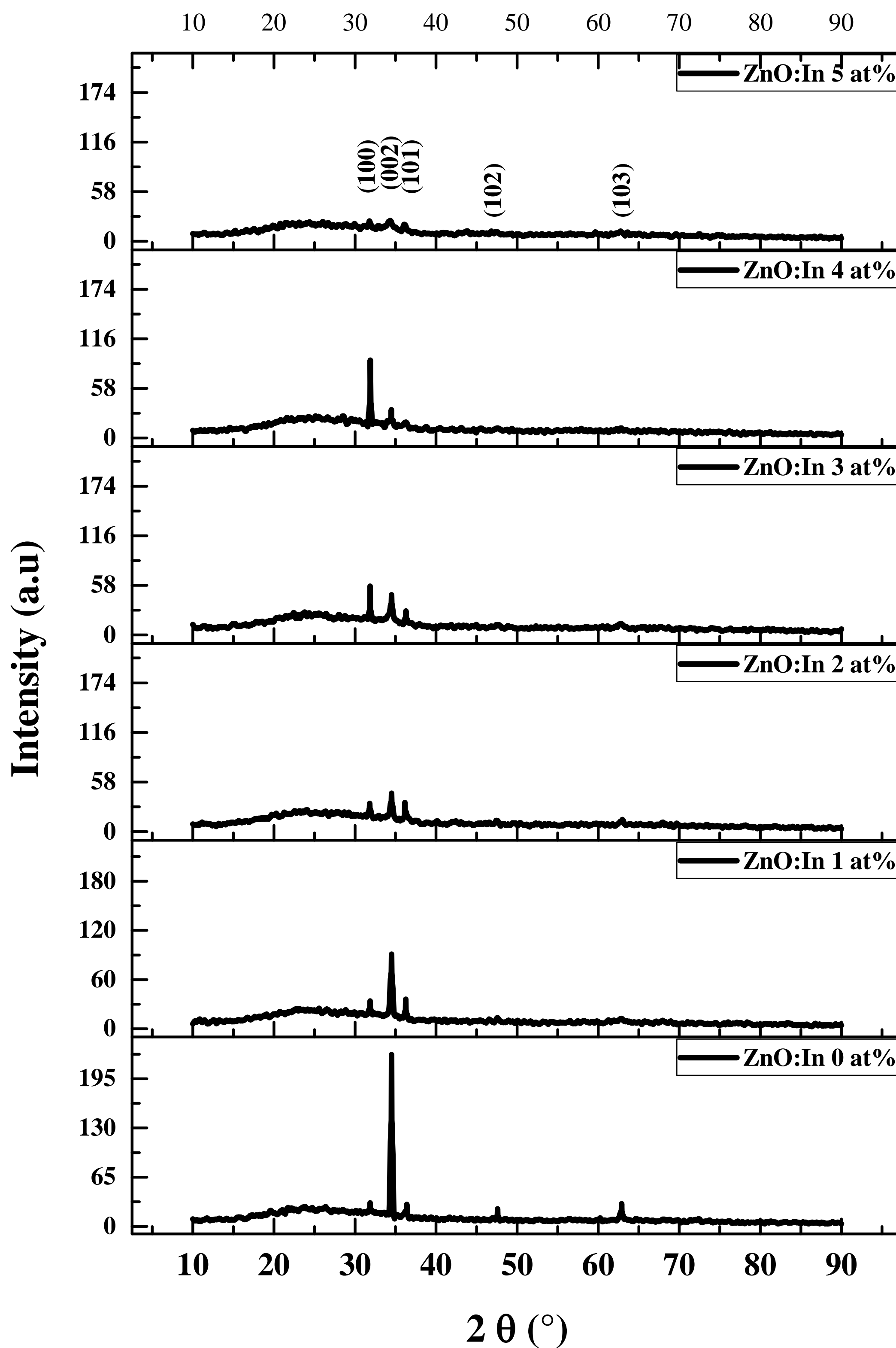

Fig III.23: X-ray diffraction analysis (XRD) of Indium doped ZnO.

One can conclude that, the Films doped with lower indium concentration exhibited a preferential growth orientation along (002) plan, while higher doping concentration changed the preferential growth orientation to another plane, (100). A similar result has been observed by T.V. Vimalkumar and al [17] J.L. van Heerden and R. Swanepoel [59] G. Singh et al [60].

III.4.2.1.1.*The texture coefficient:*

As mention before, the change of preferred orientation is analyzed using the texture coefficient. FigIII.24 represents the different values of $TC_{(002)}$, $TC_{(101)}$ and $TC_{(100)}$ calculated for the thin films of ZnO undoped and doped Indium.

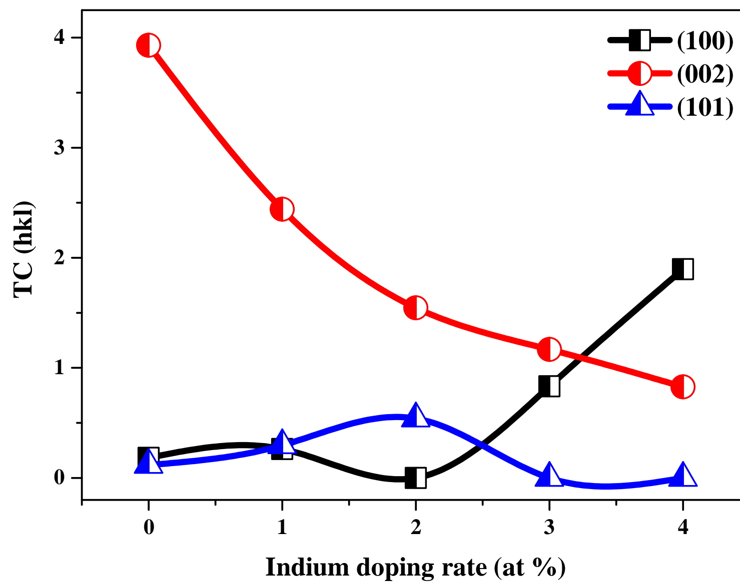

FigIII.24: The variation of the texture coefficient TC(hkl) variation of (100), (002) and (101) peaks with In doping rate of in ZnO thin films.

We can note that the undoped ZnO thin films has a preferential orientation along the (002) orientation, while the orientation of the In-doped ZnO thin films is towards the peak (100). This might be explain by dramatic structural deterioration was observed for Indium concentrations (> 2%).

The value of $TC_{(002)}$ decrease strongly as the indium concentration increases accompanying with increase in the $TC_{(100)}$ value, while that $TC_{(101)}$ overall has not changed. These results indicate that the crystal quality of the In-doped ZnO thin films can be maintained by incorporation with suitable amounts of In. The migration velocity of Indium is faster than Zn and O atoms in the ZnO lattice due to the weaker In–O bond than Zn–O bond. The In atoms could have more chance to reach Zn site earlier than O atoms during the deposition process

and O sites would be reduced, therefore the crystallinity of our thin films was quickly altered [61].

III.4.2.1.2.*Grain size of ZnO doped Indium thin films:*

Improvement of structural quality of the Indium doped ZnO thin film reached on the lowest value of the full width at half maximum (FWHM) of the (002) peak, summarized numerically in Tab III.9 and graphically in FigIII.25 represents the variation of crystallite size of ZnO thin films as a function of indium doping rate.

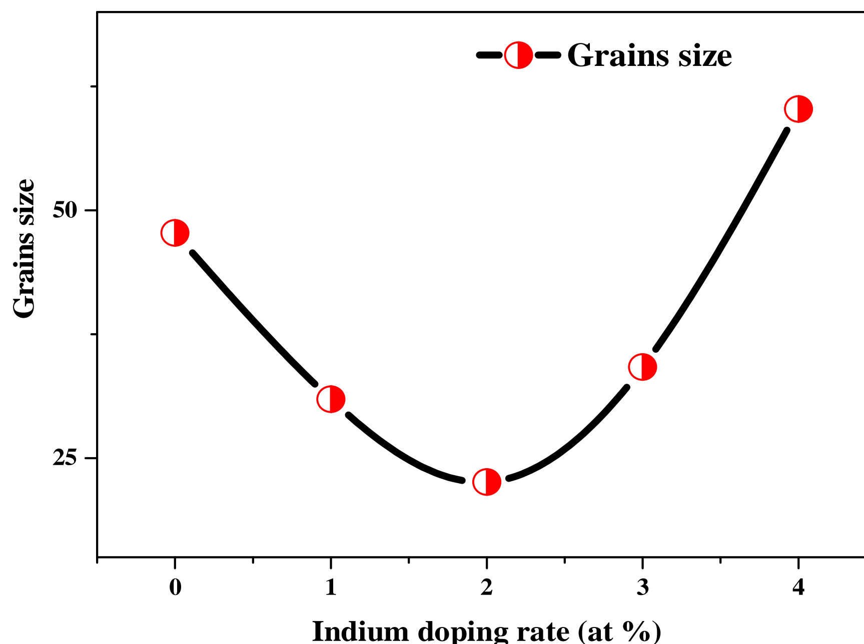

Fig III.25: Variation of crystallite size of ZnO thin films as a function of indium doping rate.

The grain size of the films is decreased with the increasing in doping atomic percentage of In up to 2 at% where it take a base value of 22.59 nm. Thus can be attributed to the random growth orientation whereas the lowest peak intensities values were found for In concentration of 2 at%. These results suggest an increase in the width of peak broadening which may be ascribed to the decrease in the size of the crystallites [55].

As the Indium concentrations are higher than 2 at%, we observed that the grain size increased, this result is in good agreement with reported XRD patterns, where the films desired a new growth orientation. Similar results were reported by A. J. Regina Mary and S. Arumugam [58].

Tab III.9: diffraction angles, FWHM and the grain size measurements.

In-doping rate (at %)	2θ (°)	FWHM	Height	Grain size (nm)
0	34,51	0,1775	213,1	**47,72**
1	34,51	0,2737	82,76	**30,94**
2	34,51	0,37496	32,23	**22,586**
3	34,51	0,24775	30,48	**34,18**
4	34,48	0,14062	16,5	**60,219**
5	/	/	/	/

III.4.2.1.3.*Stress variation of In-doped ZnO thin films:*

The calculated values of stress for different indium contents are shown in FigIII.26. From the X-ray diffraction patterns we observed the (002) peak position shifts toward the higher angle side compared to value of bulk ZnO, whereas there is a variation from 34.48° to 34.51°. This means that stresses induced in our Al doped ZnO thin films are tensile stress [24].

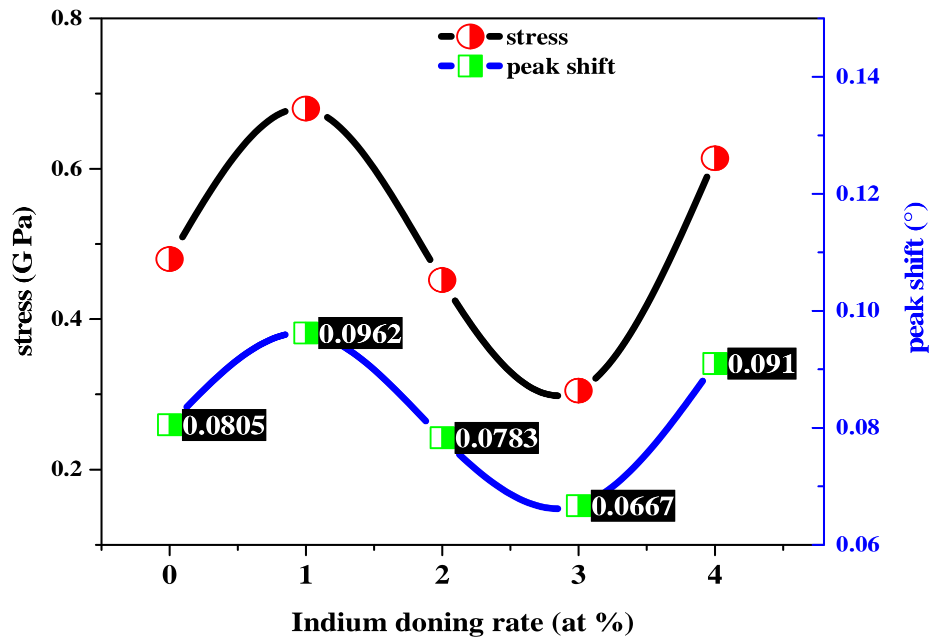

FigIII.26: Variation of stresses and (002) peak shift of the In-doped ZnO thin films.

For pure ZnO thin films the stress is mainly caused by the different thermal expansion coefficient and lattice mismatch between the glass substrate and the ZnO thin films [34, 35].

For In-doped ZnO films The inbuilt chemical pressure due to the difference in ionic radius of In^{3+} (0.80 Å) and Zn^{2+} (0.74 Å) has been anticipated to be the reason for releasing stress in In-doped ZnO films. Results of the whole samples are presented in the Tab III.10.

The stress eventually becomes the weakest at critical indium content which is 3 at%. For high indium content, indium atoms are pushed into interstitial sites leading to the expansion of the hexagonal lattice, thereby enhancing the stress in the In-doped ZnO films [62].

Tab III.10: Results of In-doped ZnO thin films deposited at varied doping rates.

In-doping rate (at %)	(hkl)	d(A°)	C	ezz	$C_{33\ film}$	Stress σ (GPa)
0	**(002)**	2,600	5,199	0,001	209,685	**-0,480**
1		2,599	5,197	0,002	210,055	**-0,680**
2		2,600	5,200	0,001	209,633	**-0,452**
3		2,601	5,201	0,001	209,360	**-0,305**
4		2,599	5,198	0,001	209,932	**-0,614**
5		/	/	/	/	/

III.4.2.1.4.*Film thickness calculation of In-doped ZnO thin films:*

FigIII.27 shows the film thickness values for different doping rate of indium, where we observe that the thickness increasing as the indium concentration increases, where it took the highest value of 342.68 nm at 3 at% of indium. For indium doping rate of 4 at% the film thickness decreased up to 250 nm, noting that for this doping rate the grain size was the highest (60 nm) and (100) plane found as preferred growth orientation. Whereas S. Edinger et all [57] found that the elongated, plate let-like grains appearing in the In-doped ZnO thin films that has the (100) plane as preferred orientation.

The film thickness increases with In percentage increment can be return into two possible reasons: the disturbance of grain growth due to the stress produced in the doped films or the increasing number of nucleation sites leading to the formation of thicker layers during dopant incorporation [63].

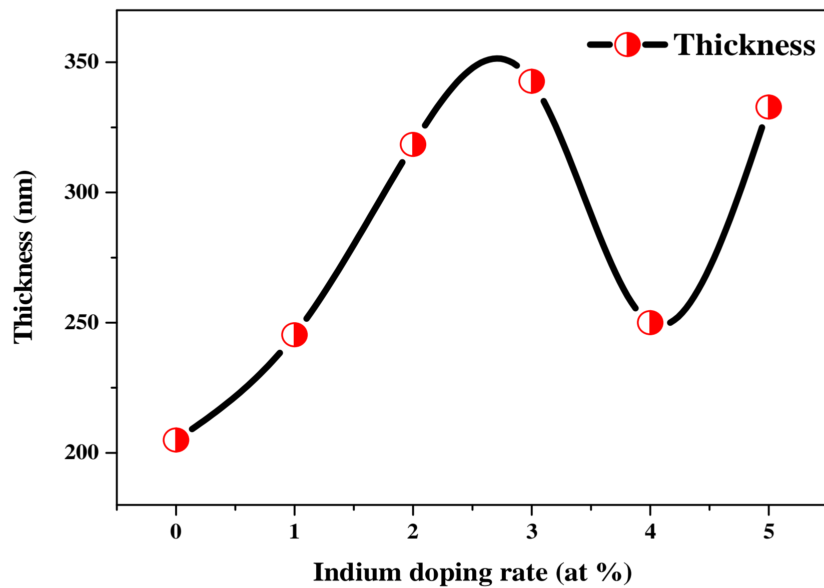

FigIII.27: The variation of film thickness of the In-doped ZnO films.

III.4.2.2.*Optical characterization (UV-Vis):*

FigIII.28 illustrates the optical transmission spectra of In-doped ZnO thin films with doping rates 1, 2, 3, 4 and 5 at% recorded as a function of wavelength in the range of 200 nm to 900 nm.

We observe for the whole samples a large absorption in the UV region and a high transparency in the visible region. However the transmission increase when In doping rates increasing. The transmittance goes up from 60% to higher than 80%. The lowest transmission value was found for pure ZnO and 1 at% In concentration, which was higher than 60% in the visible region; afterward the transmittance has improved due to the In incorporation.

All the samples show a sharp absorption edge at hand of 380 nm in the UV region. This later shifts towards shorter wavelengths indicates that the optical band gap increases with the increasing of indium content [64], as will be seen next. An absence of the interference fringes indicates that the films roughness prepared with these conditions are elevated.

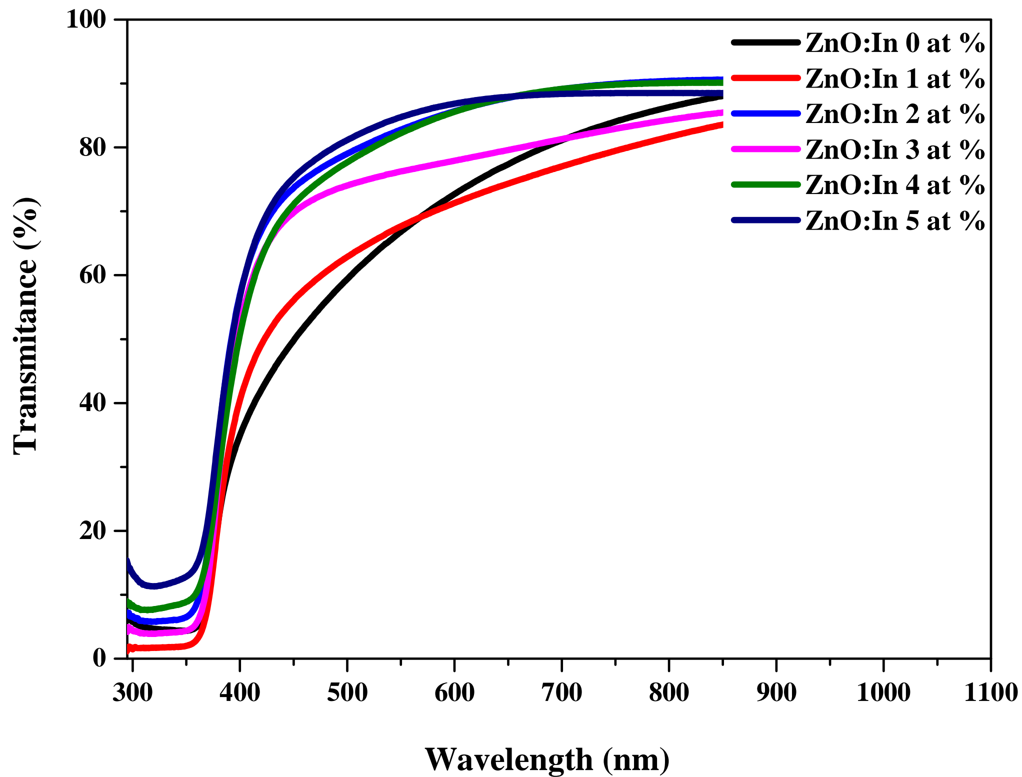

Fig III.28: Transmittance variation of the Indium doped ZnO films according to the wavelength.

The transmittance enhancement in the visible region can be associated to an improvement of the film quality with indium incorporation during growth process, similar behavior observed in refs [65, 66 and 67].

III.4.2.2.1.*Band gap energy and urbach energy:*

The band gab and Urbach energy were estimated using the transmittance spectrum; the TabIII.11 shows the band gap and Urbach energy values of undoped and doped ZnO thin films grows in different In doping rates. FigIII.29 presents the relation between optical band gap energy and In concentration.

Clearly that the optical band gap Eg was equal 3.21 eV for undoped ZnO film; afterward increases up to 3.23 eV for 1 at%, 2 at% and 3 at% indium concentration (blue shift) that is connected with crystal quality improving [65]. However, at higher indium concentration Eg trend to decrease until 3.187 eV (red shift).

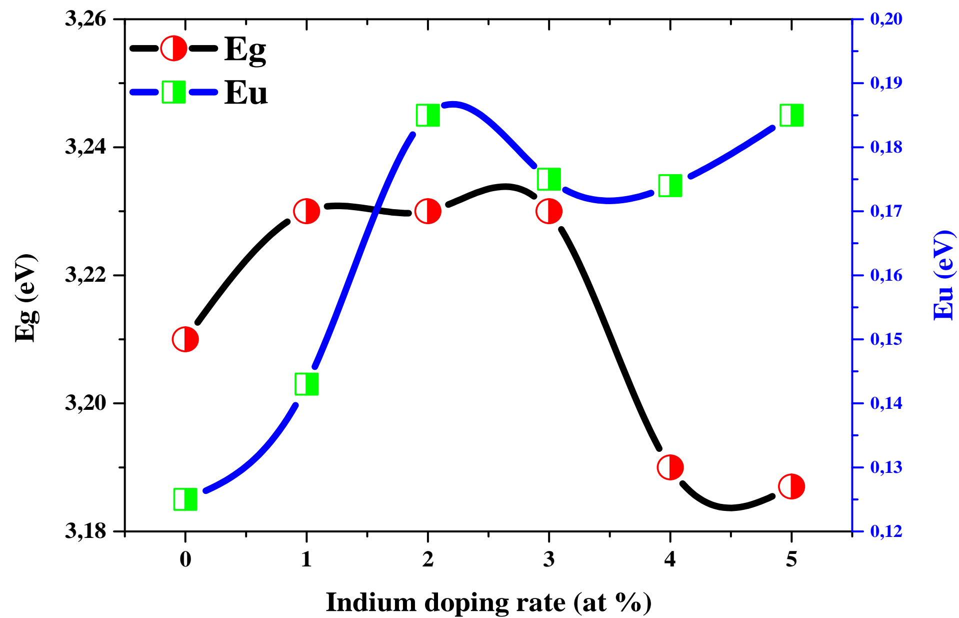

Fig III.29: the optical band gap Eg and Urbach energy Eu as a function of In doping rate.

The narrowing band gap energy is attributed to the existence of localized defect states (In impurities in Zn) into the forbidden band [68], which induce the formation of new recombination centers with lower energy state. The increase in the Eg should be also due to the increasing carrier concentration with In content [61].

The urbach energy increased with indium doping rates increase, as expected. However, the Urbach energy is closely related to the disorder in the ZnO lattice. Since the ion radius of In is larger than Zn, the In incorporation into the film is then followed by the lattice distortion and consequently disorder creation [67].

Table III.11: The optical band gap Eg and Urbach energy Eu of In-doped ZnO thin films.

In-doping rate (at %)	Eg (eV)	Eu (eV)
0	**3,21**	**0,125**
1	**3,23**	**0,143**
2	**3,23**	**0,185**
3	**3,23**	**0,175**
4	**3,19**	**0,174**
5	**3,187**	**0,185**

III.4.2.3.*Electrical characterization:*

Undoped ZnO is an n type TCO and has a high resistivity. By adding Indium impurity to semiconductor, it substituted by Zn (because of their similarity of ionic radius). Since In has one more electron than Zn, acts as donor impurity and creates an n type semiconductor [69]. The electrical properties of the samples are investigated by electrical resistivity and conductivity measurements.

III.4.2.3.1.*Electrical conductivity of Indium doped ZnO thin films:*

The effect of indium doping on the electrical conductivity was obtained at different doping rates and it was shown in FigIII.30 that doping had a significant effect of the electrical conductivity of ZnO doped with indium. The estimated electrical resistivity and conductivity with respect to indium doping are tabulated in the TabIII.12.

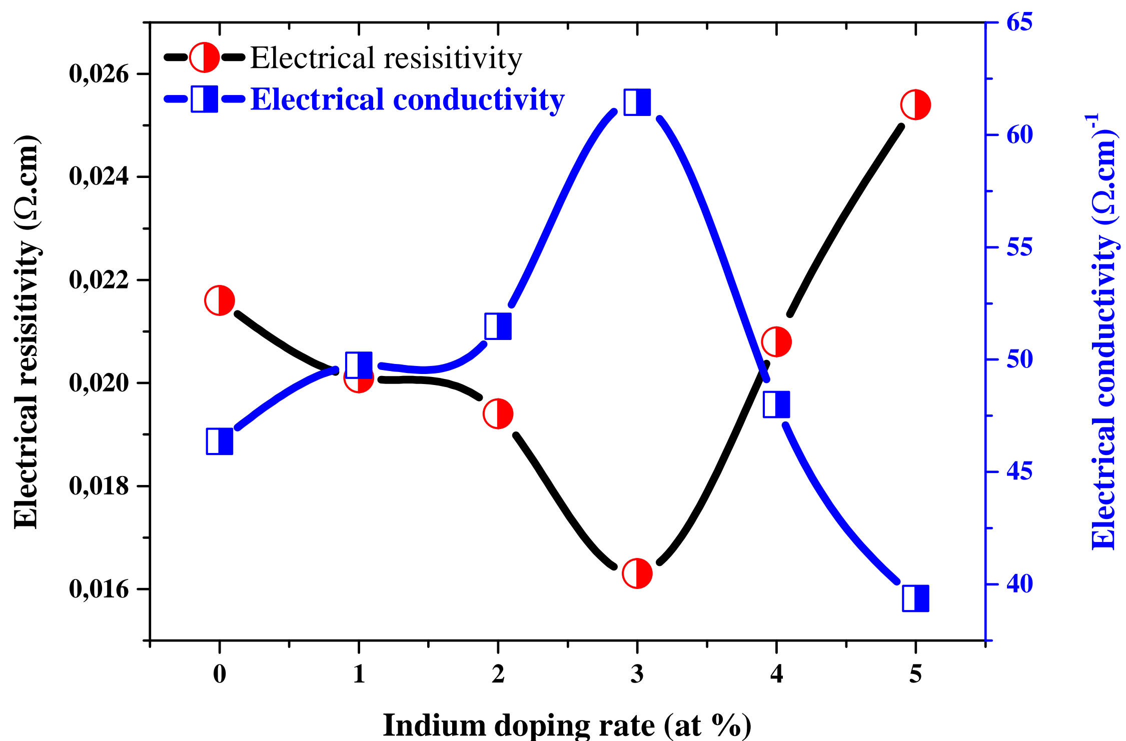

Fig III.30: The variation of electrical conductivity of ZnO doped at different In concentrations.

From the FigIII.30, at lower indium concentration (from 1at % to 3at %) an increase in conductivity was observed (from $0,497\times10^2\ (\Omega.cm)^{-1}$ to $0,515\times10^2\ (\Omega.cm)^{-1}$). This may be due by the substitution of indium ions (In^{3+}) in place of zinc ions (Zn^{2+}), which induces a free

electron to conduction band, besides free electrons produced from interstitial zinc and oxygen vacancies. Thereby the carrier concentration enhances [68, 70].

With further increase of In concentration (4 at% and 5 at%) the conductivity is decreased. This could be due to the inactivity of added dopant atoms. Therefore, at higher doping rates a saturation of substitutional sites takes place and this leads to another mode of dopant incorporation, which ends by a decrease in crystallinity [29], as observed from XRD patterns, thus the electrical conductivity go to the lowest values.

Tab III.12: estimated electrical resistivity and conductivity of In-doped ZnO thin films.

In-doping rate (at %)	Thickness (Cm)	I (A)	U (Volt)	Resistivity (Ω.cm)	Conductivity $(\Omega.cm)^{-1}$
0	$2,067 .10^{-05}$	0,03	3	**0,0216**	**46,36**
1	$2,267 .10^{-05}$	0,03	2,55	**0,0201**	**49,74**
2	$2,009 .10^{-05}$	0,03	2,78	**0,0194**	**51,48**
3	$1,999 .10^{-05}$	0,03	2,34	**0,0163**	**61,44**
4	$1,996 .10^{-05}$	0,03	3	**0,0208**	**48,00**
5	$0,021 .10^{-08}$	0,03	3,46	**0,0254**	**39,36**

III.4.2.4.*In summary*: From the obtained results, for In-doped ZnO thin films, following conclusions can be drawn:

1. The whole prepared In-doped ZnO films are polycrystalline with a hexagonal würtzite structure of ZnO. When In-doping rate goes up the (002) peak intensity decrease strongly accompanied by an increase in the (100) peak intensity. The crystallite size found in the range of 22,6 to 60,22nm. The film thickness found mostly increased with in incorporation from ~200 to 343 nm.
2. We observed a high transparency for all samples in the visible region greater than 70%; the transparency has improved due to the In incorporation, with a sharp absorption edge at hand of 380 nm. The optical energy gaps varied from 3,187 to 3.23 eV.
3. The electrical conductivity increased for lower In concentration then decreased for the higher. The highest value was achieved at 3 at% of In doping rate ($0,52\times10^{2}$ $(\Omega.cm)^{-1}$).

References:

[1] A. Souissi, A. Boukhachem, Y. BenTaher, A. Ayadi, A. Mefteh, M. Ouesleti, S. Guermazi, M. Amlouk, Optik, 125 (2014) 3344-3349.

[2] N. Renaut, M. Jimenez, J. Dutroncy, M. Traisnel, Thin Solid Films, 589 (2015) 161-164.

[3] M. Kumar, A. Kumar, A. C. Abhyankar, ACS Applied Materials & Interfaces, 7 (2015) 3571-3580.

[4] S. Benramache, B. Benhaoua, N. Khechai, F. Chabane, Matériaux & Techniques, 100 (2012) 573-580.

[5] T. P. Rao, M. C. S. Kumar, S. A. Angayarkanni, M. Ashok, Journal of Alloys and Compounds, 485 (2009) 413-417.

[6] N. A. Jayah, H. Yahaya, M. R. Mahmood, T. Terasako, K. Yasui and A. b. M. Hashim, Nanoscale Research Letters, 10 (2015) 1-10.

[7] A. I. Abd Ali, International Journal of Scientific & Engineering Research, 5 (2014) 2250-2256.

[8] A. Bedia, F.Z. Bedia, M. Aillerie, N. Maloufi, B. Benyoucef, Energy Procedia, 74 (2015) 529-538.

[9] S. Abed, H. Bougharraf, K. Bouchouit, Z. Sofiani, B. Derkowska-Zielinska, M. S. Aida, B. Sahraoui, Superlattices and Microstructures, 85 (2015) 370-378.

[10] D. Miao, H. Hu, L. Gan, Journal of Alloys and Compounds, 639 (2015) 400-405.

[11] S. Benramache, B. Benhaoua, O. Belahssen, Optik, 125 (2014) 5864-5868.

[12] R. Mimouni, O. Kamoun, A. Yumak, A. Mhamdi, K. Boubaker, P. Petkova, M. Amlouk, Journal of Alloys and Compounds, 645 (2015) 100-111.

[13] S. Ben-Ameur, A. Barhoumi, R. Mimouni, M. Amlouk, H. Guermazi, Superlattices and Microstructures 84 (2015) 99-112.

[14] S. Benramache, B. Benhaoua, Superlattices and Microstructures, 52 (2012) 1062-1070.

[15] G-X. Liang, P. Fan, XI-M. Cai, D-P. Zhang and Z-H. Zheng, Journal of Electronic Materials, 40(3) (2011) 267-273.

[16] B. Sarma, D. Barman and B. K Sarma, Applied Surface Science, 479 (2019) 786-795.

[17] T.V. Vimalkumar, N. Poornima, K.B. Jinesh, C. Sudha Kartha and K.P. Vijayakumar, Appl.Surface Sci, 257 (2011) 8334-8340.

[18] O. Mohamed, Synthesis and characterization of Zinc Oxide (ZnO) Thin films deposited by spray pyrolysis for applying: electronics and photonics, doctoral thesis, University Mohamed Khider of Biskra, 2018.

[19] G. He, B. Huang, S. Wu, J. Li, Sixth International Conference on Thin Film Physics and Applications, 6984 (2008) 69842E (1- 4).

[20] M-C. Jun and J-H. Koh, Nanoscale Res Lett, 7 (2012) 1-7.

[21] M. Vadivel, R. Ramesh Babu, K. Ramamurthi, Chem Tech, 7 (2015) 1206-1211.

[22] B. L. ZHU, X. H. Sun, S. S. Guo, X. Z. Zhao, J. Wu, R. Wu and J. Liu, Japanese Journal of Applied Physics, 45(2006) 7860–7865.

[23] Y. Wang, W. Tang, L. Zhang, J. Mater. Sci. Technol, 31 (2015) 175-181.
[24] H-J. Li, Z-J. Wang, H. Xia, Z-Y. Xiong, J-X. Wang, B-C. Yang, Optics Communications, 282 (2009) 247–252.
[25] J. A. B. Miranda, O. Calzadilla, S. S-J. Hernández, I. Diez-Pérez, J. Díaz, F. Sanz, F. F. Chále-Lara, F. J. E Faller, F. Caballero-Briones, Materials Science: Materials in Electronics, 29 (2018) 2016-2025.
[26] K. Bahedi, M. Addou, M. El Jouad, Z. Sofiani, H. EL Oauzzani, B. Sahraoui, Applied Surface Science, 257 (2011) 8003-8005.
[27] A. A. Al-Ghamdia, O. A. Al-Hartomya, M. El Okrc, A.M. Naward, S. El-Gazzard, F. El-Tantawyd, F. Yakuphanoglu, Spectrochimica Acta Part A: Molecular and Biomolecular Spectroscopy, 131 (2014) 512-517.
[28] S.H. Sabeeh, R.H. Jassam, Results in Physics, 10 (2018) 212-216.
[29] A. Nakrela, N. Benramdane, A. Bouzidi, Z. Kebbab, M. Medles, C. Mathieu, Results in Physics, 6 (2016) 133-138.
[30] A.E. Rakhshani, Appl. Phys. A, 92 (2008) 413-416.
[31] S Mondal, S R Bhattacharyya and P Mitra, PRamana journal of physics, 80 (2013) 315-326.
[32] M. Rouchdi, E. Salmani, B. Fares, N. Hassanain, A. Mzerd. Results in Physics, 7 (2017) 620-627.
[33] K. Bahedi, M. Addou, M. El Jouad, Z. Sofiani, H. EL Oauzzani, B. Sahraoui, Applied Surface Science, 257 (2011) 8003-8005.
[34] T. P. Rao, M. C. S. Kumar, S. A. Angayarkanni, M. Ashok, Journal of Alloys and Compounds, 485 (2009) 413-417.
[35] Z. Y. Alami, M. Salem, M. Gaidi, J. Elkhamkhami, Advanced Energy: An International Journal, 2 (2015) 11-24.
[36] A. El Manounia, F.J. Manjón, M. Mollar, B. Marí, R. Gómez, M.C. López, J. R. Ramos-Barrado, Superlattices and Microstructures, 39 (2006) 185–192.
[37] M. Ajili, N. Jebbari, N. Kamoun Turki and M. Castagné, EPJconf, 29, 00002 (2012) 1-9.
[38] F. A. Garcés, N. Budini, R. D. Arce, J. A. Schmidt , Procedia Materials Science, 9 (2015) 221-229.
[39] E. P. da Silva, M. Chaves, G. J. da Silva, L. B. de Arruda, P. N. Lisboa-Filho, S. F. Durrant, J. R. Ribeiro Bortoleto, Materials Sciences and Applications, 4 (2013) 761-767.
[40] C. Euvananont, S. Pakdeesathaporn, P. Pratoomwan, V. Yodsri, Y. Boontongkong, C.Thanachayanont and C. Boothroyd, A microstructural investigation of Al-doped ZnO films prepared by spray pyrolysis, 25th Annual Conference Microscopy Society of Thailand, Thailand, 2008.
[41] M. A. Haque and M. Sigamani, Asian J. Chem, 25 (2013) S205-S208.
[42] F. K. Mugwang'a, P. K. Karimi, W. K. Njoroge and Omayio, J Fundam Renewable Energy, 5 (2015) 1-6.
[43] E. Bacaksiz, S. Aksu, S. Yılmaz, M. Parlak, M. Altunbaş, Thin Solid Films, 518 (2010) 4076-4080.
[44] M. Khudhr, K. H. Abass, International Journal of Engineering and Technologies, 7

(2016) 25-31.

[45] M. Suchea, S. Christoulakis, Katsarakis N, Kitsopoulos T, Kiriakidis G.Thin Solid Films, 515 (2007) 6562-6566.

[46] S. J. Baik, J. H. Jang, C. H. Lee, W. Y. Cho, K. S. Lim; Appl Phys Lett. 70 (1997) 3516-3518.

[47] M-C. Jun and J-H. Koh, Nanoscale Research Letters, 7 (2012) 1-7.

[48] H. H-C. Lai, T. Basheer, V. L. Kuznetsov, R. G. Egdell, R. M-J. Jacobs, M. Pepperand Peter, P. Edwards, Journal of Applied Physics, 112 (2012) 083708 (1-5).

[49] A.A. Al-Ghamdi, O. A. Al-Hartomy, M. El Okr, A.M. Nawar, S. El-Gazzar,F. El-Tantawy, F. Yakuphanoglu, Spectrochimica Acta Part A: Molecular and Biomolecular Spectroscopy, 131 (2014) 512-517.

[50] R. R. Kothawale and R. M. Mohite, Advanced Materials Research, 1110 (2015) 218-221.

[51] D. Raviendra and J. K. Sharma, J. Appl. Phys. 58 (1985) 838-844.

[52] R- B-H Tahar, Jornal of the european ceramic society 25 (2005) 3301- 3306.

[53] J. Mass, P. Bhattacharya, R.S. Katiyar; Materials sciences and engineering, 103 (2003) 9-15.

[54] I. Saadeddin, Preparation and characterization of new transparent conducting oxides based on SnO_2 and In_2O_3: Ceramics and thin films, doctoral thesis, University of Bordeaux I, (2007).

[55] L. K. Dintle, P. V. C. Luhanga, Ch. Moditswe, C. M. Muiva, Physica E: Low-dimensional Systems and Nanostructures, 99 (2018) 91-97.

[56] S. D. Senol, International Journal of Applied Ceramic Technology, 16 (2018) 138-145.

[57] S. Edinger, N. Bansal, M. Bauch, R. A. Wibowo, G. Újvári, R. Hamid, G. Trimmel, T. Dimopoulos, Journal of Materials Science, 52 (2017) 8591-8602.

[58] A. J. Regina Mary and S. Arumugam, International Research Journal of Engineering and Technology, 04 (2017) 192-196.

[59] J.L. van-Heerden, R. Swanepoel , Thin Solid Films, 299 (1997) 72-77.

[60] G. Singh, S. B. Shrivastava, D. Jain, S. Pandya,T.Shripathi and V. Ganesan, Bull. Mater. Sci, 33(2010) 581-587.

[61] M.S. Kim, K.G. Yim, S. Kim, G. Nam, D-Y. Lee, J. Soo-Kim, J. Su-Kimand, J.Y. Leem, Acta Physica Polonica A, 121 (2012) 217-220.

[62] B. Singhand, S. Ghosh, Journal of Electronic Materials, 43 (2014) 3217-3221.

[63] J. Ungula, F. B. Dejene and H. C. Swart, SA Institute of Physics (Proceedings of SAIP), (2016) 82-87.

[64] A. Bedia, F.Z. Bedia, M. Aillerie, N. Maloufi, B. Benyoucef , Energy Procedia, 74 (2015) 529-538.

[65] B. El-Filali, J.A. Jaramillo-Gomez , T.V. Torchynska, J.L. Casas-Espinola, L. Shcherbyna, Optical Materials, 89 (2019) 322-328.

[66] N. Lameche, S. Bouzid, M. Hamici, M. Boudissa, S. Messaci, K. Yahiaoui, Optik, 127 (2016) 9663-9672.

[67] A. Hafdallah, F. Yanineb, M.S. Aida, N. Attaf, Journal of Alloys and Compounds, 509 (2011) 7267-7270.

[68] A. Bouaine, A. Bourebia, H. Guendouz , Z. Riane, Optik, 166 (2018) 317-322.
[69] M. R. Rokn-Abadi, M. Behdani, H. Arabshahi and N. Hosseini, International Review of PHYSICS, 12 (2009) 103-106.
[70] S. P. Bharath, K. V. Bangera, G.K. Shivakumar, Superlattices and Microstructures, 124 (2018) 72-78.

Chapter IV:

Results and Discussion for

(Pneumatic Study)

IV.1.*Introduction:*

In the present chapter, we will discuss the deposition of undoped and Aluminium doped zinc oxide thin films, using the pneumatic spray pyrolysis technique, to study the effect of substrate temperature, with two different carrier gas (air) pressures, and the doping rates on the structural, optical and electrical properties of the films.

IV.2.*Chapter Objectives:*

The objectives of this chapter are:

1. Present structural, optical and electrical properties discovered in the present study, as a patterns, picture and tables.
2. Interpretation and discussion this results.

IV.3. *Effect of substrate temperature:*

Undoped Zinc oxide (ZnO) thin films have been deposited with various substrate temperatures 300, 350, 400 and 450 °C, with 1 and 1,5 bar as a carrier gas (air) pressure, using pneumatic spray pyrolysis technique onto glass substrates. The effects of substrate temperature on the crystallization behavior, optical and electrical properties of the films have been studied.

IV.3.1.*Part one:* Substrate temperature – Spray pressure: 1,5 bar

In this part we studied the effect of the substrate temperature on undoped ZnO thin films properties sprayed at air pressure of 1,5 bar.

IV.3.1.1.*Structural Characterization:*

FigIV.1 displays X-ray diffraction (XRD) patterns of ZnO films deposited at various substrate temperatures 300, 350, 400, 450°C. We can mention that all the films showed only a strong peak at 2θ at hand 34°, which in the diffraction angle 2θ region from 10° to 90°. Thus identified only the (002) peak of hexagonal ZnO are observed. The diffraction patterns emphasize that our ZnO films have a hexagonal structure [1].

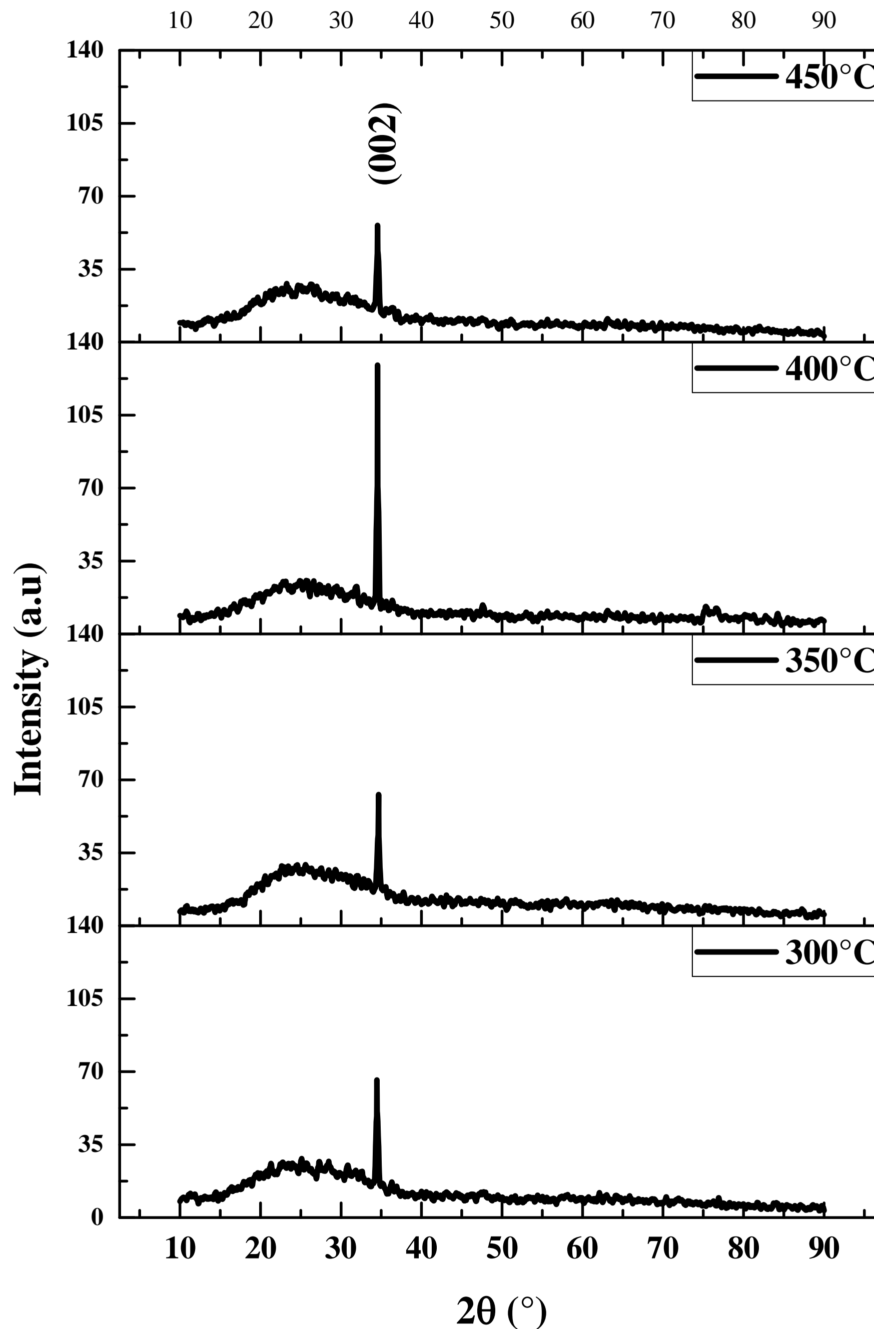

FigIV.1: X-ray diffraction (XRD) patterns of ZnO films deposited with various substrate temperatures at 1,5 bar as carrier gas pressure.

The highest diffraction peak intensity was found at 400°C substrate temperature, while the rest intensity values were approximate; see TabIV.1. Strong diffraction peak with narrow FWHM implies high crystallinity. However, with substrate temperature increasing the ZnO (002) peak position was changed significantly. That is, the ZnO (002) peak position was

shifted with increasing the substrate temperature to higher angle side toward compared to value of bulk ZnO. This shift means that the lattice constant c decreases with increasing the substrate temperature, which is considered to be related to the residual stress in the ZnO thin films [2].

Tab IV.1: peaks diffraction angles (2θ) and intensity of ZnO films deposited at various substrate temperatures with 1,5 bar as carrier gas pressure.

	2θ (°)	intensity
300 °C	34,45	66
350 °C	34,66	63
400 °C	34,54	129
450 °C	34,54	56

IV.3.1.1.1.*Grains size of undoped ZnO thin films:*

The calculated grain sizes corresponding to (002) diffraction peaks are given in TabIV.2. The variation of our films grains size in dependence of substrate temperature were presented in FigIV.2.

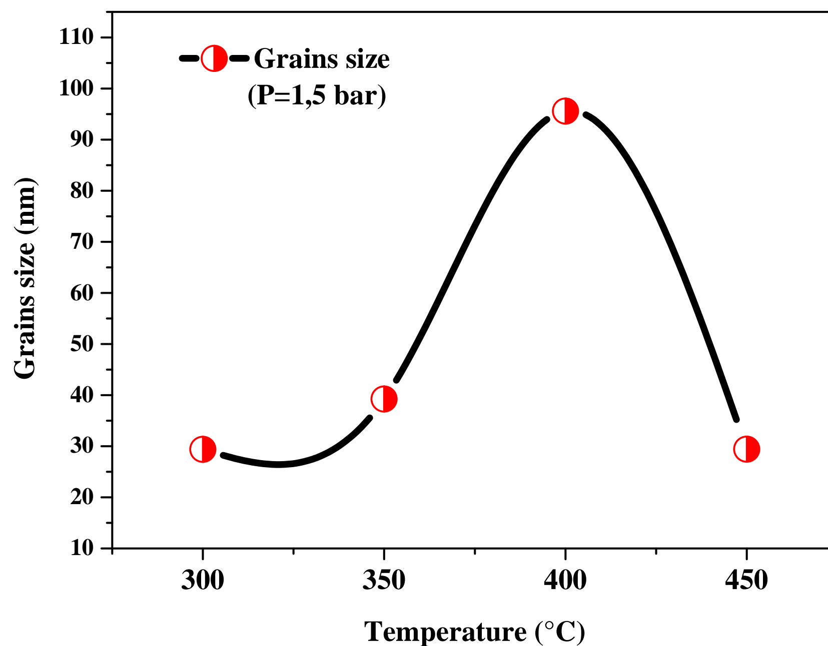

FigIV.2: The grain size variation of ZnO films with substrate temperature deposited at 1.5 bar.

The average crystallite size, is varied in the range of 29-96 nm, was calculated form the full width at half maximum. As can be seen, the grain size increases from 29 to 96 nm with substrate temperature from 300 to 400 °C and then again decreases to 29 nm for 450 °C. Moreover, it can be noted that the optimal value of the average grain size of the undoped ZnO films, 95.6 nm, was obtained for substrate temperature 400°C (see TabIV.2), similar result found by A. Rahal et all [3].

The lattice constant *c* of undoped ZnO thin films calculated (see Tab IV.3) was approached to the lattice constant of bulk ZnO (c_0=5.206 Å) indicating the strain is along the c-axis. The increase of the grain size has been indicated by the enhancement of the crystallinity and c-axis orientation of ZnO thin films [4]. At high temperature atoms have more energy to acquire a correct site in the crystal lattice, which leads the grains to grow larger [5].

Tab IV.2: Variation of diffraction angle, FWHM and Grain size with substrate temperature of ZnO films deposited at 1,5 bar as carrier gas pressure.

Substrate temperature (°C)	2θ (°)	FWHM	Grain size
300°C	34,4831	0,288	**29,40**
350°C	34,6494	0,216	**39,22**
400°C	34,549	0,0886	**95,59**
450°C	34,5754	0,288	**29,41**

IV.3.1.1.2.*Stress variation of undoped ZnO thin films:*

The variation of the film stress and peak shift is described in FigIV.3. Calculated values of stress in the undoped ZnO thin films are listed in TabIV.3. Shifts in the (002) peak position also indicate stress in the films. The deficiency of crystallites during the growth can allocate the intrinsic stress. The intrinsic stress is caused in the thin films by the deposition parameters such as substrate temperature, carrier gas pressure and deposition duration [5].

From the TabIV.3, the lattice constant c_{film} values of the ZnO thin films deposited at various substrate temperatures are greater than to the c value of bulk ZnO (c_{bulk} = 5.204 Å). This indicates that the unit cell of ZnO film is elongated along the growth direction, namely, compressively strained [2]

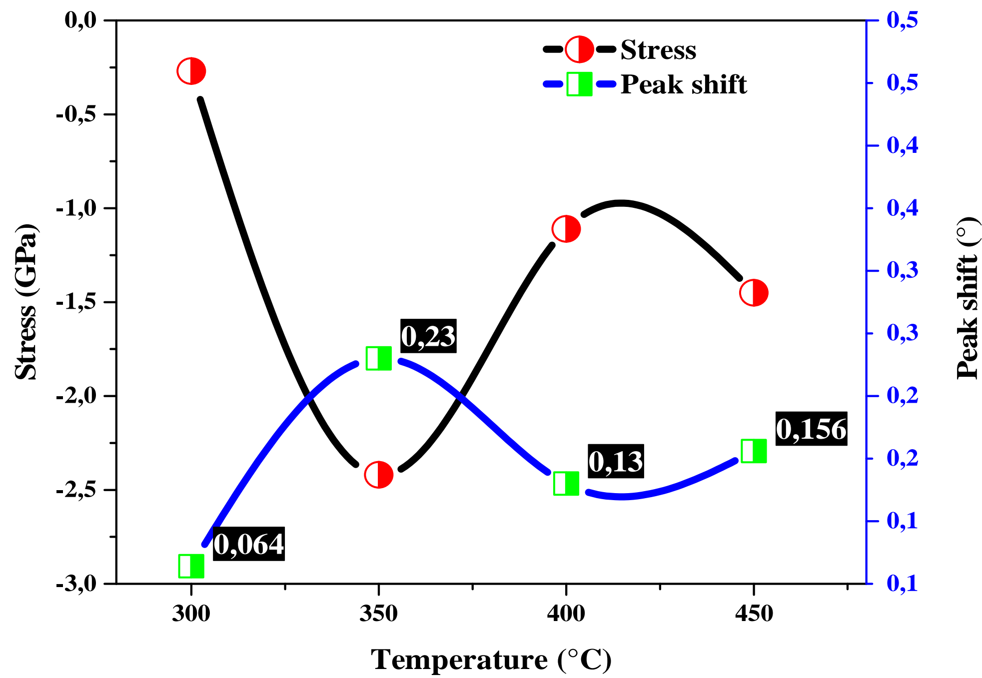

FigIV.3: The variation of the stress and peak shift as a function of substrate temperature with 1,5 bar as carrier gas pressure.

However, from the TabIV.3, is obviously that, whole of stresses have a negative signal (strain e_{zz}>0) that means tensile stresses occur, as the peak shift described. As the FigIV.3 shows, there is a decrease in the film stress with an increase in the substrate temperature. In addition, the ZnO thin film deposited at 350°C was found to have the highest stress among the samples and was in almost stress Free State [2]. These results demonstrate that the stress in the ZnO thin film deposited by spray pneumatic method is relaxed with increasing the substrate temperature.

Tab IV.3: Results of undoped ZnO thin films deposited at varied substrate temperatures.

Substrate temperature (°C)	(hkl)	d (Å)	C	e_{zz}	C_{33film}	Stress σ (GPa)
300°C	(002)	2,60 0921	5,2018	0,000607	209,2983	**-0,27**
350°C		2,588818	5,1776	0,005257	213,2399	**-2,42**
400°C		2,596111	5,1922	0,002455	210,8539	**-1,11**
450°C		2,594189	5,1884	0,003193	211,4794	**-1,45**

The stress relaxation with substrate temperature increasing arises from the thermal mismatch of different layers, namely, the ZnO film and substrate due to the difference in their thermal expansion coefficients.

IV.3.1.1.3.*Film thickness of undoped ZnO thin films:*

The variation of undoped ZnO thin films thickness deposited at different substrate temperatures is shown in FigIV.4. The film thickness decreased from 222 to 110 nm when substrate temperature varied from 300 to 400 °C, then increase again to 223 nm for 450 °C.

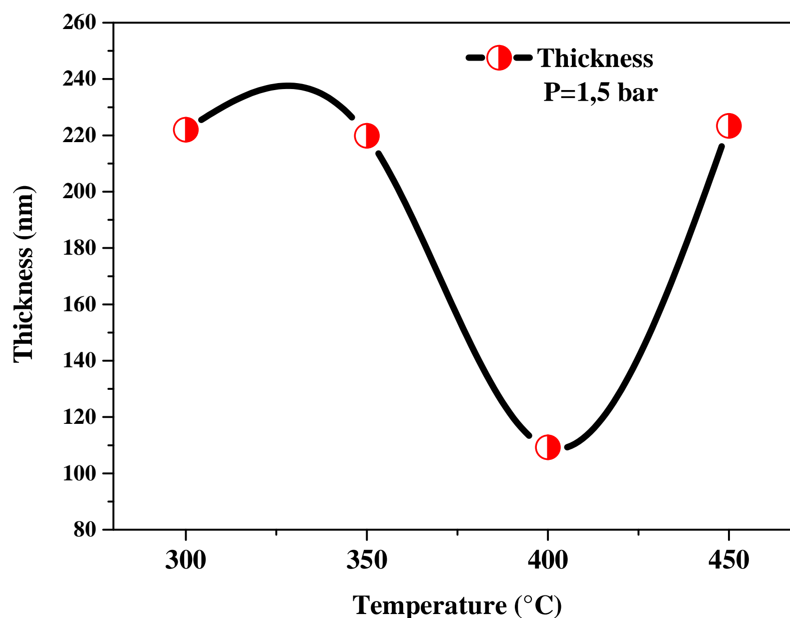

FigIV.4: The thickness variation of undoped ZnO thin films deposited at different substrate temperatures.

As can be seen, from FigIV.4, the films deposited for various substrate temperatures show a decrease of thickness from 222 to 110 nm as the temperature increase from 300 to 400 °C, similar behavior seen by M. Othmane et all [4]. This maybe due by rapid surface diffusion of material from the strained surface areas at the grain centers to the grain boundary regions [6], without missing that the deposition air pressure was high relatively thus allowing produce more stresses [7]. Noting that, a maximum grain size value and strong diffraction peak with narrow FWHM, which implies high crystallinity, were observed for the sample deposited at 400 °C as substrate temperature; this will create a denser film and thus a lowest thickness.

IV.3.1.2. Optical characterization (UV-Vis):

The percentage of transmission is measured using UV-Vis Spectrophotometer. The optical transmission of ZnO films was determined from the transmission measurement in the range of 290–1000 nm. The optical transparency of the ZnO thin film is one of the most important factors which need to be taken into consideration for a better TCO.

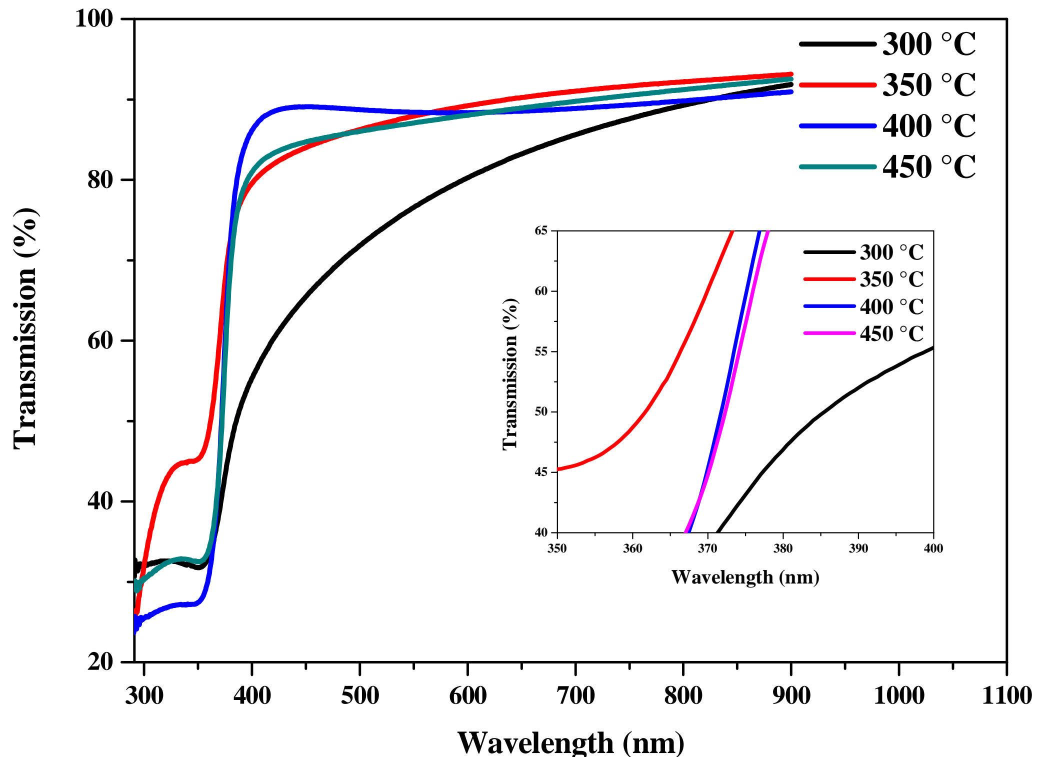

FigIV.5: Transmittance versus wavelength of ZnO thin films grown at different substrate temperatures with pressure of 1,5 bar.

FigIV.5 show the transmittance spectra of four ZnO thin films grown at different substrate temperatures ranging from 300 to 450°C with an interval of 50 °C, with 1,5 bar as carrier gas (air) pressure. The films deposited at 300, 350 and 400°C present a high transmittance above to 80% in the visible wavelength range and sharp absorption edge near to 375 nm. The rest film, deposited at 300°C present a lower transmittance, but greater than 70%. The increase of transmittance related to an increase of films grain size [8], noted that the weakest grain size value recorded at 300 °C.

However, the spectra show that the whole films are highly transparent in the visible region while a strong absorbance is seen in wavelengths below 380 nm. The abrupt fall in the transmission (as shown in the inset of FigIV.5) for wavelengths below 380 nm refers to the absorbance in ZnO. This corresponds to the region of the onset fundamental absorption in the layers due to the transition between the valence band and the conduction band [6].

Moreover, we observed that all spectra appears a bump (boss) between wavelength 290 nm to 350 nm, the latter means that our ZnO films have included a porosity which may be due to, the thickness effects, the light scattering due to the difference of the quality of the film surface or grain size [7], plus high carrier gas pressure. In addition, the films show an absence of interference fringes in the transmission spectrum, thus produced by the interference of light reflected from air film and film substrate interface. This unfortunately indicates that our film surfaces are neither smooth.

IV.3.1.2.1.*Band gap energy and Urbach energy of undoped ZnO:*

We can see in FigIV.6, which present the variation of the band gap energy Eg and urbach energy Eu of undoped ZnO thin films deposited at varied substrate temperature with 1,5 bar as deposition air pressure,

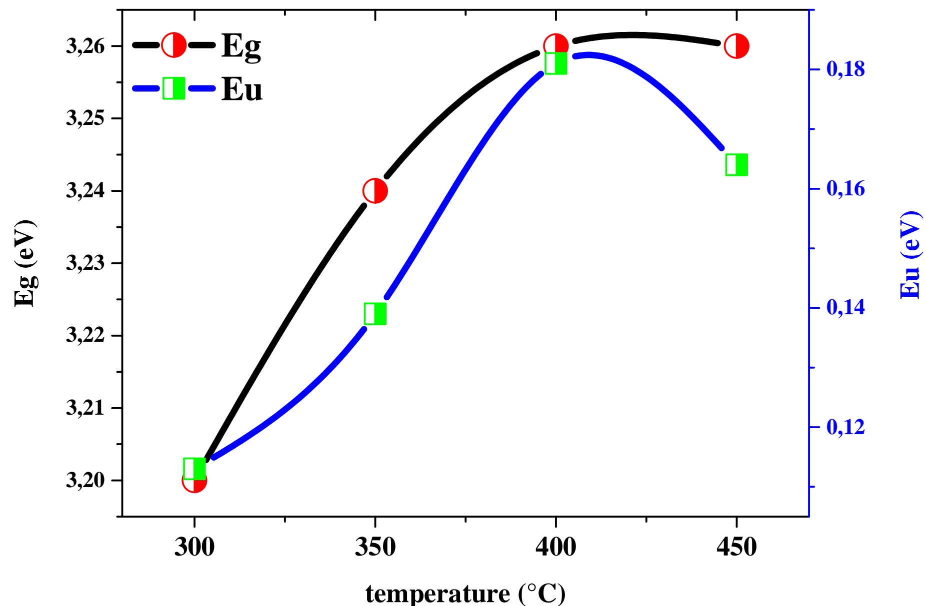

FigIV.6: band gap and Urbach energy of undoped ZnO thin films grown at different substrate temperatures with pressure of 1,5 bar.

that corresponding to an increase of the substrate temperature pendant the growth, the band gap energy increases, from 3.20 eV to 3.26 eV, and similar changes with the corresponding Urbach energy, from 0.11 eV to 0.18 eV which was slightly almost (see TabIV.4). The Urbach energy is directly link to the defects in the crystal layer, at a low value of Urbach energy directly correspond a high crystalline quality.

The increase of direct band gap Eg with the increasing of substrate temperature from 300 to 450 °C, indicates an improvement of the quality of the film. We attribute this behavior to the weak presence of the structural defects [9]. In a similar study, A. Bedia et al [10] have reported the enlargement of the optical band gap in ZnO films with the increase of the grain sizes with the substrate temperature during growth.

Tab IV.4: calculated optical band gap and Urbach energy of undoped ZnO thin films.

Substrate temperature (°C)	Eg (eV)	Eu (eV)
300°C	**3,2**	**0,113**
350°C	**3,24**	**0,139**
400°C	**3,26**	**0,181**
450°C	**3,26**	**0,164**

IV.3.1.3.*Electrical characterization:*

IV. 3.1.3.1.*Resistivity of Zinc Oxide Films:*

Dependences of the film resistivity on substrate temperature for the undoped ZnO thin films are shown in FigIV.7 Measured electrical resistivity and conductivity using four probes technique is presented in TabIV.5. It is obvious from the curve that the resistivity of the films increases from $0,5\times10^{-3}$ to $28,7\times10^{-3}$ Ω.cm with substrate temperature increment from 300 to 450 °C. Similar behavior was found by [11, 12]. The minimum resistivity $0,5\times10^{-3}$ and $0,8\times10^{-3}$Ω.cm, thus maximum conductivity, are found for samples deposited at lowest substrate temperature 300 and 350°C.

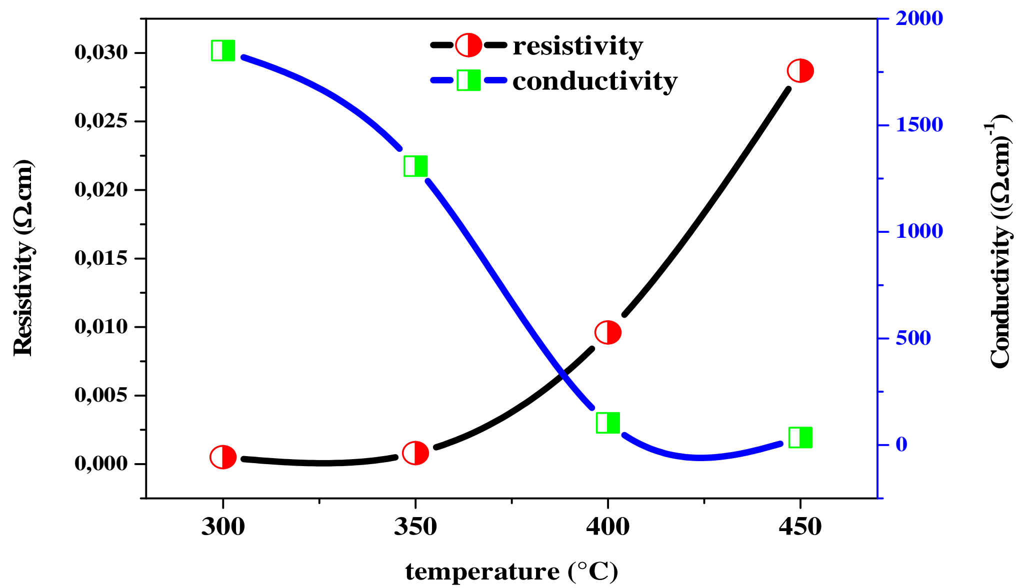

FigIV.7: The variation of electrical conductivity and resistivity of undoped ZnO films deposited at 1,5 bar.

However, the electrical conduction in ZnO is dominated by electrons generated from O^{2-} vacancies and Zn interstitials, however, lower resistivity produced by higher crystal orientation. This phenomenon is due to the reduction in the scattering of the carriers at the grain boundaries and crystal defects, which increases the carrier mobility [13].

Tab IV.5: measured electrical resistivity and conductivity of undoped ZnO thin films deposited at varied substrate temperatures.

substrate temperature (°C)	Thickness (nm)	I (A)	U (Volt)	Resistivity (Ω.cm)	Conductivity $(\Omega.cm)^{-1}$
300°C	221,966	0,03	0,07	**$0,5\times10^{-3}$**	**$18,50\times10^{2}$**
350°C	219,8	0,03	0,1	**$0,8\times10^{-3}$**	**$13,08\times10^{2}$**
400°C	109,225	0,03	2,53	**$9,6\times10^{-3}$**	**$1,04\times10^{2}$**
450°C	223,346	0,03	3,7	**$28,7\times10^{-3}$**	**$0,35\times10^{2}$**

IV.3.2.*Part two*: Substrate temperature – Spray pressure: 1 bar

In this part we studied the effect of the substrate temperature on undoped ZnO thin films properties sprayed at air pressure of 1 bar, noted that the whole deposition process conditions are remained unchanged.

IV.3.2.1.*Structural Characterization:*

The XRD patterns of undoped ZnO films grown in various substrate temperature with 1 bar as a carrier gas (air) pressure showed at FigIV.8, present the same form, that is only a (002) diffraction peak. This indicates that ZnO thin films prepared by spray pneumatic display a good orientation perpendicular to the substrate surface (c-axis).

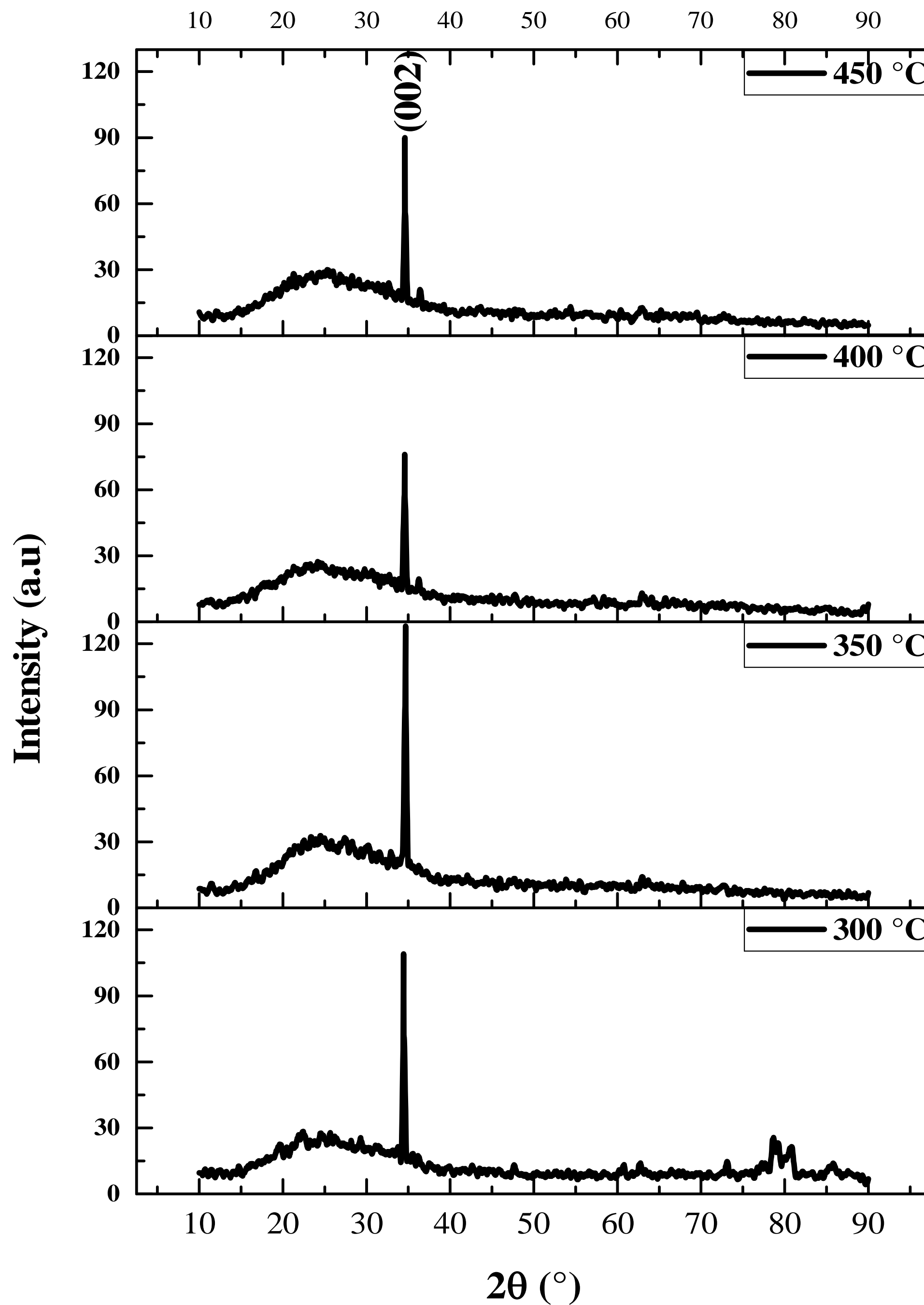

FigIV.8: X-ray diffraction (XRD) patterns of ZnO films deposited with various substrate temperatures at pressure of 1 bar.

The diffraction peak angles in the present case appears a shifts compared with the (002) peak position of powder ZnO (34.42°) as given in TabIV.6, the diffraction angles of the films were higher. Which result in the decrease of c-axis value, this indicates that ZnO films suffer a compressive or tensile stress along the interfaces. The smaller FWHM value indicates that the ZnO films are more textured along the c-axis [8].

Tab IV.6: peaks diffraction angles (2θ) and intensity of ZnO films deposited at various substrate temperatures with 1 bar as carrier gas pressure.

substrate temperatures (°C)	2θ (°)	intensity
300°C	34,418	109
350°C	34,6464	128
400°C	34,5518	76
450°C	34,6085	90

IV.3.2.1.1. Grain size calculation of undoped ZnO thin films:

The calculated grain sizes of the (002) diffraction peaks and the results are given in TabIV.7. The variation of undoped ZnO films grains size versus substrate temperature were illustrated in FigIV.9.

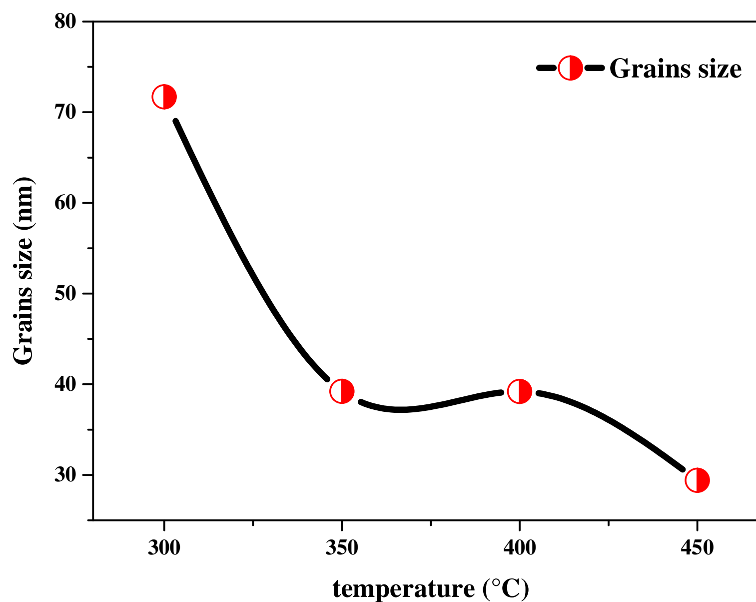

FigIV.9: The grain size variation of ZnO films deposited at 1 bar, according to (002) peak, with different substrate temperatures.

The average crystallite size, is varied in the range of 29-72 nm, was calculated form the full width at half maximum. As can be seen, the grain size decreases with substrate temperature increment, reverse to the results found in the previous case (1,5 bar of air pressure). That, at higher deposition air pressure (1,5 bar) the droplet becomes more fine which makes the reaction droplets-substrate occur, thereby film growth efficiency. In addition, we can estimate, that 1,5 bar of deposition air pressure, is appropriate to achieve a thin films of Zinc Oxide with crystalline structure, as found in ref [7]. The optimal value of the average grain size, 72 nm, was obtained at substrate temperature 300°C (see TabIV.7). The grain size decrease is probably because of the large strain in the films, caused by low pressure, which affects the normal growth of ZnO grains [14]. Moreover, B. Godboleis et all [15] observed that the grain size decreases with the increase in thickness (consider FigIV.11).

Tab IV.7: Variation of diffraction angle, FWHM and Grain size with substrate temperature of ZnO films deposited at 1 bar as carrier gas pressure.

substrate temperature (°C)	2θ (°)	FWHM	Grains size
300°C	34,418	0,1181	**71,69**
350°C	34,6464	0,216	**39,22**
400°C	34,5518	0,216	**39,21**
450°C	34,6085	0,288	**29,41**

IV.3.2.1.2.*Stress variation of undoped ZnO thin films:*

FigIV.10 represents the variation of the film stress and peak shift as a function of substrate temperature deposited at 1 bar as carrier gas pressure. Calculated values of stress in the undoped ZnO thin films are listed in TabIV.8.

For ZnO thin films deposited at 300°C the stress found positive (strain $e_{zz}<0$) which mean that the film is exhibited a compressive stress in the plane of the substrate surface, and to tensile stress for the rest ZnO films deposited at 350, 400 and 450°C.

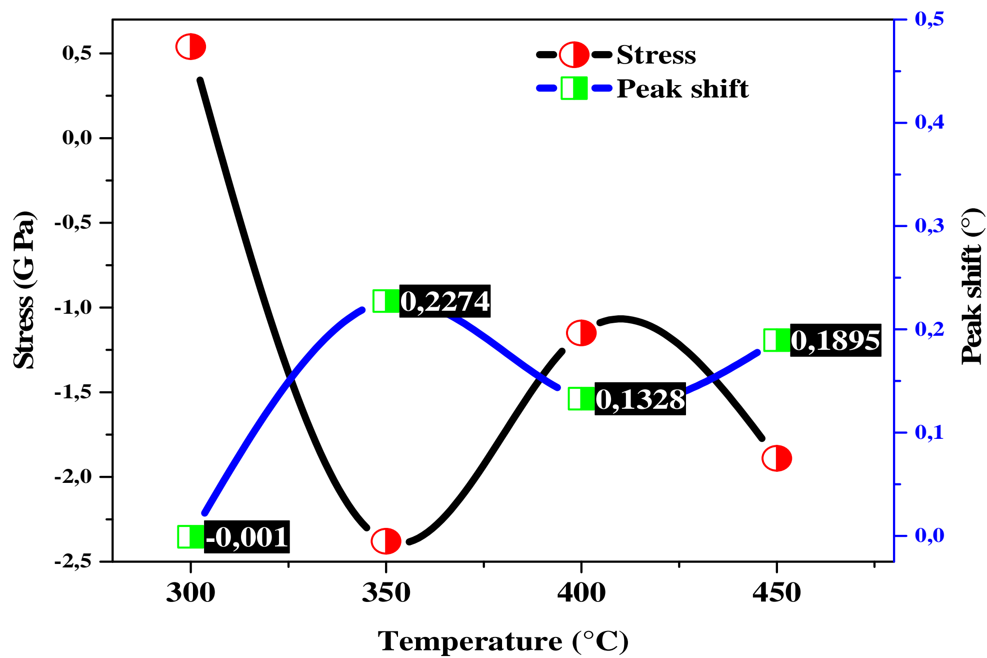

FigIV.10: The variation of the stress and peak shift as a function of substrate temperature at pressure of 1 bar.

The stress, along the c-axis, changes from compressive to tensile by providing sufficient thermal energy [16]. However, as the figure shows, there is a decrease in stress when substrate temperature increasing. In this work, the stress in undoped ZnO thin film is considered to be the intrinsic stress which is attributed to lattice mismatch between the ZnO film and substrate [2].

Tab IV.8: Results of undoped ZnO thin films deposited at varied substrate temperatures.

substrate temperature (°C)	(hkl)	d(A°)	C	ezz	$C_{33\ film}$	Stress σ (GPa)
300°C	(002)	2,606	5,2114	-0,00123	207,7699	**0,54**
350°C		2,5896	5,1781	0,005174	213,1683	**-2,38**
400°C		2,596	5,1918	0,002533	210,9202	**-1,15**
450°C		2,592	5,1836	0,004118	212,2655	**-1,89**

IV.3.2.1.3.*Film thickness variation of undoped ZnO thin films:*

The variation of undoped ZnO thin films thickness deposited at different substrate temperatures is shown in FigIV.4.The film thickness increased from 210 to 340 nm with substrate temperature increment from 300 to 350 °C and then decrease to 220 nm for 450 °C.

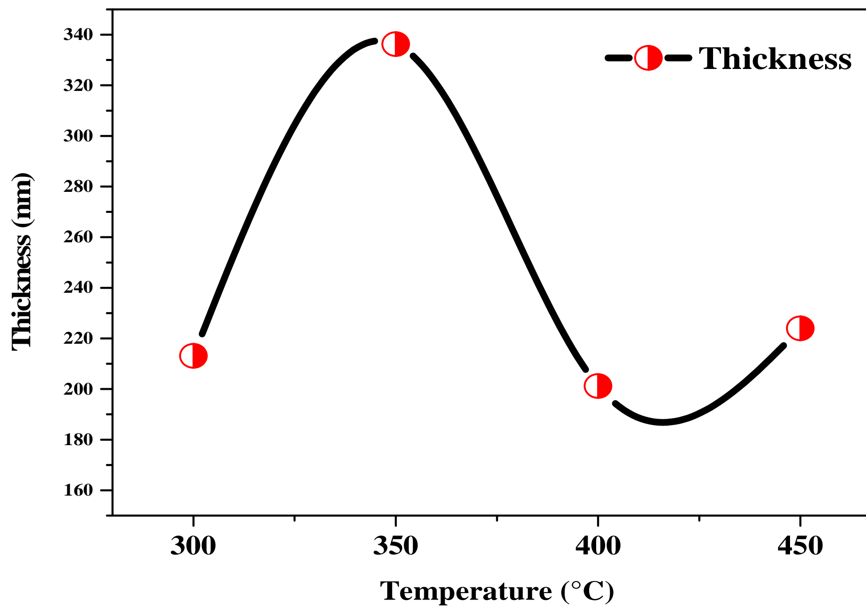

FigIV.11: The thickness variation of undoped ZnO thin films deposited at different substrate temperatures.

The film thickness decrease with substrate temperature increment was also in good agreement with the literatures [17, 18]. However, at lower temperatures, the film thickness is more due to incomplete decomposition and powdery nature of films while for higher temperatures thickness is less due to the early evaporation of precursor solution [19].

IV.3.2.2.*Optical characterization (UV-Vis):*

FigIV.12 show the transmittance spectra of ZnO thin films grown in various substrate temperature 300, 350, 400 and 450°C, with 1 bar as carrier gas (air) pressure. The films deposited at 300, 350 and 450°C present a high transmittance above to 80% for 350 and 450 °C and above to 70 % for 400 °C, this is in the visible wavelength range, and sharp absorption edge near to 375 nm. The rest film, deposited at 400°C, present a lesser transmittance, greater

than 60% and sharp absorption edge exposed to shift toward near to 380 nm. However, as can be seen, the increase in the substrate temperature improves the films optical transmission; one can note that the substrate temperature effect is clearly observed in the film quality. In addition the increase of transmittance related to an alteration of films grain size [8].

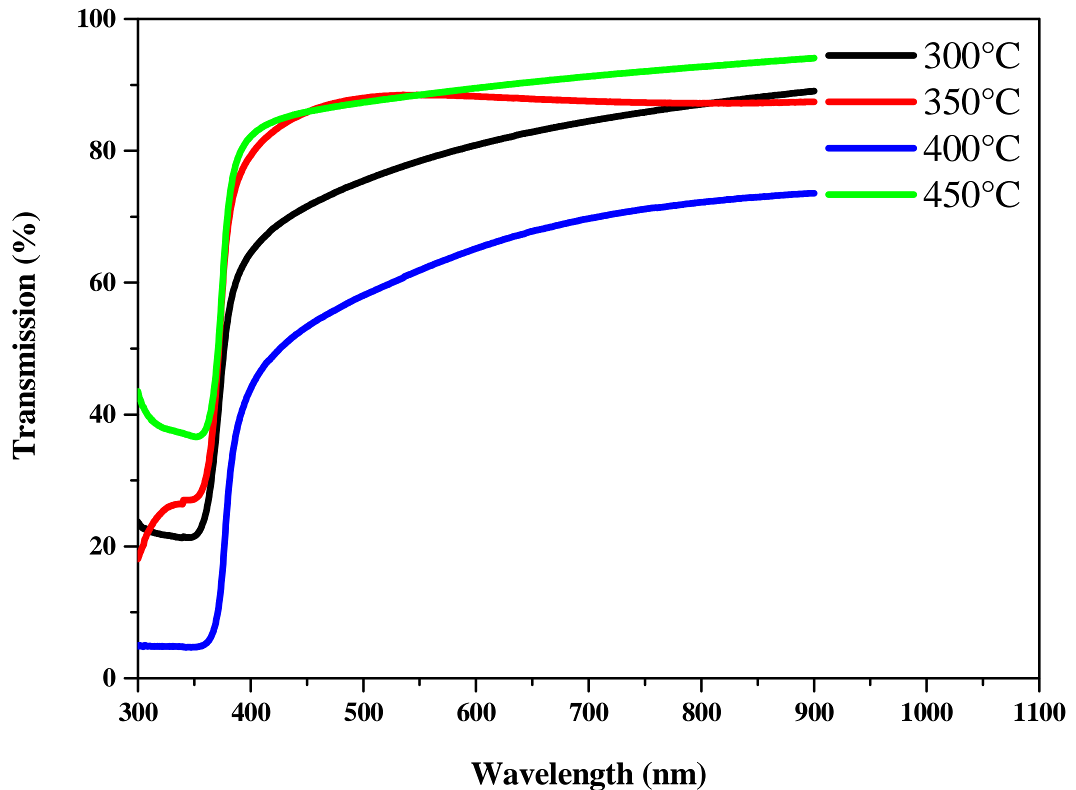

FigIV.12: Transmittance versus wavelength of ZnO thin films grown at different substrate temperatures at pressure of 1 bar.

The observed intensive increase in absorption result to the direct electrons transition, as previous mention. The highest optical transparency was recorded at 350 and 450 °C. The spectra exhibit a shift in the bang edge due to the variation of substrate temperature with the absorption edge shifted to shorter wavelength at higher growth temperature, similar behavior was found by T. Parasada et all [17].

IV.3.2.2.1.Band gap energy and Urbach energy:

The variation of optical band gap versus growing process temperature was shown in FigIV.13. From the curve the band gap decrement from 3.26 to 3.23 eV was observed, when the deposition temperature was changed from 300 to 400 °C, and then increase again to 3.257

eV for 450 °C (see Tab IV.9). For the corresponding Urbach energy, a weak increase from 0.11 to 0.18 eV with deposition temperature varied from 300 to 350 °C was observed, followed by smaller values. However, the weak Urbach energy found directly correspond to high crystalline quality.

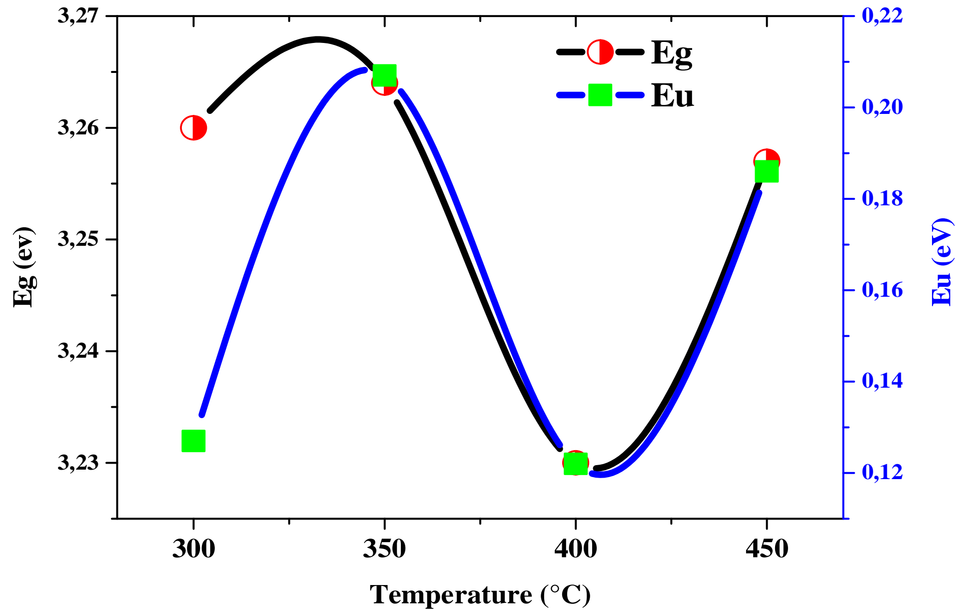

FigIV.13: band gap and Urbach energy of undoped ZnO thin films grown at different substrate temperatures at pressure of 1 bar.

As previously elucidated, this decrease in direct band gap is in agreement with the variation in grain size, which decrease with substrate temperature increment, and this was predicted by the shifts of absorption edges toward shorter wavelength (see again FigIV.12) for films growing at increasing deposition temperatures.

Tab IV.9: calculated optical band gap and Urbach energy of undoped ZnO thin films.

Substrate temperature (°C)	Eg (eV)	Eu (eV)
300°C	**3,26**	**0,127**
350°C	**3,264**	**0,207**
400°C	**3,23**	**0,122**
450°C	**3,257**	**0,186**

IV.3.2.3.*Electrical characterization:*

IV.3.2.3.1.*Resistivity of Zinc Oxide Films:*

The resistivity change of undoped ZnO films with different substrate temperature is shown in FigIV.14. The resistivity films increased from $4,8\times10^{-3}$ to $13,2\times10^{-3}\Omega$.cm with increased deposition temperature, noted that, the resistivity is weak and the change remains slight in the same order. Thus, the conductivity decreased.

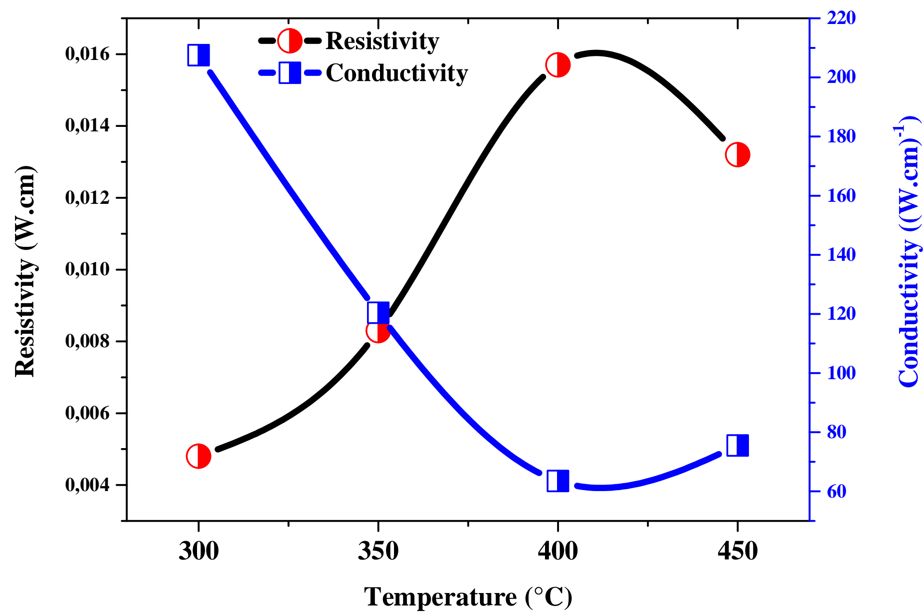

FigIV.14: The variation of electrical conductivity and resistivity of undoped ZnO films deposited at 1 bar.

Tab IV.10: measured electrical resistivity and conductivity of undoped ZnO thin films deposited at varied substrate temperatures.

Substrate temperature (°C)	Thickness (nm)	I (A)	U (Volt)	Resistivity (Ω.cm)	Conductivity $(\Omega.cm)^{-1}$
300 °C	213,13	0,03	0,65	**$4,8\times10^{-3}$**	**$2,08\times10^{2}$**
350 °C	336,284	0,03	0.71	**$8,3\times10^{-3}$**	**$1,20\times10^{2}$**
400 °C	201,179	0,03	2,25	**$15,7\times10^{-3}$**	**$0,64\times10^{2}$**
450 °C	223,949	0,03	1,7	**$13,2\times10^{-3}$**	**$0,76\times10^{2}$**

As was observed, the conductivity of ZnO thin film decreases with increase in temperature, which indicating its semiconducting electrical behavior. The film deposited at 300 °C substrate temperature shows the higher conductivity ~210 $(\Omega.cm)^{-1}$ than deposited at 350, 400 and 450 °C (see Tab IV.10). As before mentioned, this behavior can be attributed to the reduction in the scattering of the carriers at the grain boundaries and crystal defects [13].

IV.3.2.4.*In summary:* From the obtained results, for ZnO thin films deposited at various substrate temperatures with two carrier gas (air) pressures, following conclusions can be drawn:

1. From XRD analysis, all the films showed only a strong peak at hand of 2θ=34°, this emphasizes that ZnO films have a hexagonal structure with high crystallinity. The highest diffraction peak intensity was found at 400°C with 1,5 bar and at 350°C for 1 bar, of substrate temperature and carrier gas pressure respectively. The substrate temperature increment changes significantly the (002) peak intensity and position, i.e. film crystallinity quality and make more or less stress. For 1,5 bar, the film thickness and crystallite size found mostly unchanged, in the range of 220 nm and 30 nm respectively, with crystallite size of ~100 nm and thickness of 110 nm found for the sample deposited at 400°C. For 1 bar, the crystallite size decreased, from 72 to 30 nm, with substrate temperature increases, while the thickness has not changed (~ 220 nm), despite 340 nm of thickness found for sample prepared at 350°C.
2. All the films display high transparency greater than 80%, with absorption edge around 375 nm. The substrate temperature increases enhances the transparency. The optical energy gaps increased from 3,20 to 3,26 eV with substrate temperature increment in the case of 1,5 bar as pressure; and decreased from to 3,264 to 3,23 eV in the case of 1 bar.
3. The electrical conductivity decreased with substrate temperature increases. For 1,5 bar of pressure, the highest values, $18,5\times10^{2}$ and $13,1\times10^{2}$ $(\Omega.cm)^{-1}$, were found for films deposited at 300 and 350°C respectively. For 1 bar of pressure, The highest values, $2,1\times10^{2}$ $(\Omega.cm)^{-1}$, was found for film deposited at 300 °C.

IV.4.*Effect of doping (Aluminium doped ZnO):*

In order to find out the impact of Aluminium doping rate, we have deposited undoped and Al doped ZnO samples with different doping rates 1, 2, 3, 4 and 5 at % on glass substrates using pneumatic spray pyrolysis technique, the effects of Al-doping rate on the structural, optical and electrical characteristics of ZnO thin films were obtained. In addition, whole of thin films have analyzed and discussed. Mention that, the Al-doped were deposited at 400°C as substrate temperature with 1bar, 0,1 $mo.l^{-1}$, 0,2 $ml.min^{-1}$ and 20 min as carrier gas (air) pressure, start solution molarity, solution flow rate and deposition time respectively. In fact, these experimental conditions were selected based on the results obtained in the current work and the group search results.

IV.4.1.*Structural Characterization:*

The crystal phases and structures of the synthesized Al-doped ZnO were performed using X-ray diffraction analysis. Typical XRD spectra for undoped and Al-doped ZnO thin films with various at% Al of 0, 1, 2, 3, 4 and 5 are shown in FigIV.15. The whole films, undoped and Al-doped of ZnO, exhibited a strong orientation along c-axis (002) perpendicular to the substrate surface, which belong to a hexagonal crystal structure. Noted that, No characteristics reflection peaks related to Al and other related impurities alumina phases were detected in the X-ray pattern, which supports that whole Al atoms substituting Zn in the crystal lattice or redundant Al segregating to the non-crystalline region in the grain boundary [20, 21].

The sharp peaks and high intensity reflect that the synthesized Al-doped ZnO films are well crystalline. However, for Al-doping ratio 4 at% new diffraction peak appear with lower intensity, (101), thus indicate that the great member of Al atoms causes a loss of preferential orientate through the film growth, similar behavior observed in refs [22, 23]. Besides, for this latter the spectrum is of poor quality, and this indicates that high Al doping rate causes a decrease of the crystalline quality.

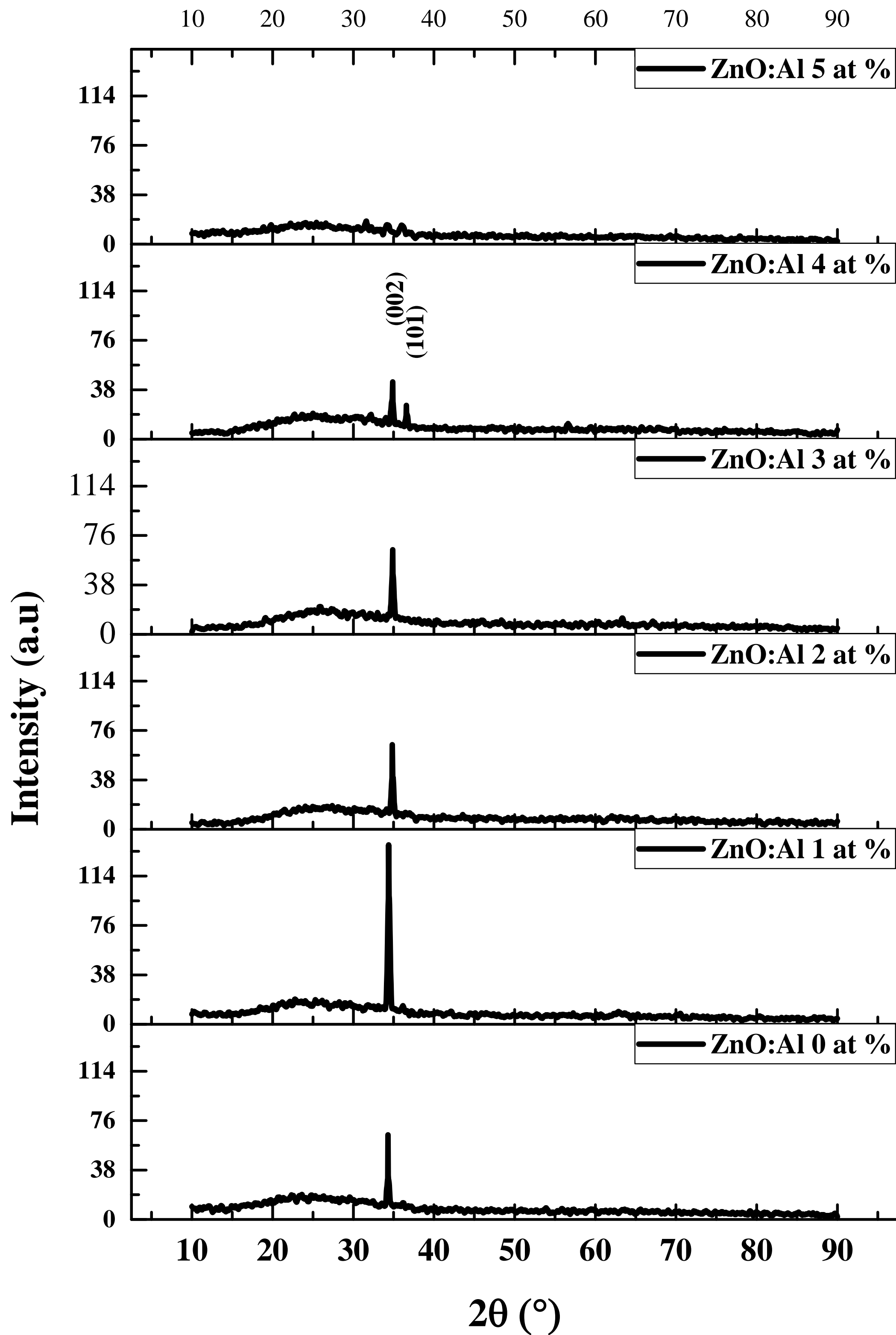

FigIV.15: XRD patterns of undoped ZnO and Al-doped ZnO with various Al doping rates, at air pressure of 1 bar and 400°C substrate temperature.

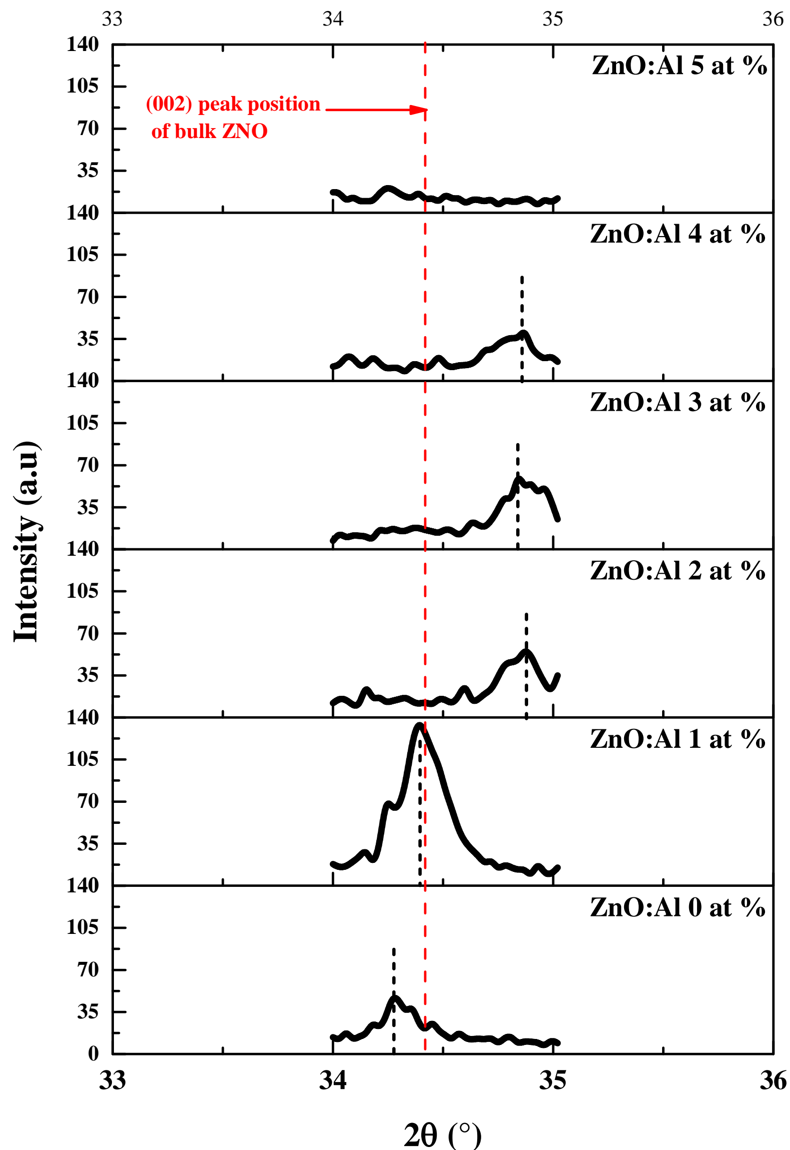

FigIV.16: The variation of (002) peak position and intensity of undoped and doped ZnO deposited with various doping rates and at 1 bar.

The (002) diffraction peak intensity of Al-doped ZnO films decreased with doping rates increasing, as represented in FigIV.16. This indicates that the doping rate increase cause a distortion in films crystallinity. In fact, the incorporation of Al into of Zn may give rise to the generation of different sorts of stress caused by the differences in the ion size between Al (0,054 nm) and Zn (0.074 nm), which could be the reason behind the modifications in the structure [21]. When the Al atoms are substituted into Zn sites in the crystal, the lattice constant in c-axis are expected to be shorten, so the position of the ZnO (002) peak will undergo a shift to the higher 2θ value [24].

When the Al doping rate increasing to 5 at%, the diffraction peak completely disappears, which Emphasizes the film amorphous structure, the act of carrier gas pressure was important and causing a fast loss of crystallinity. Furthermore, when peaks sharper and higher in intensity indicating to the increase the grain size.

IV.4.1.1.*Grain size calculation of Al-doped ZnO thin films:*

The effect of doping rates on the films grain sizes is represented in FigIV.17; Tab IV.11 shows the calculated grain sizes values. The results show an improvement in grain sizes versus undoped ZnO. The increasing of Al doping rates increased the grain size from 29 nm to 55 nm.

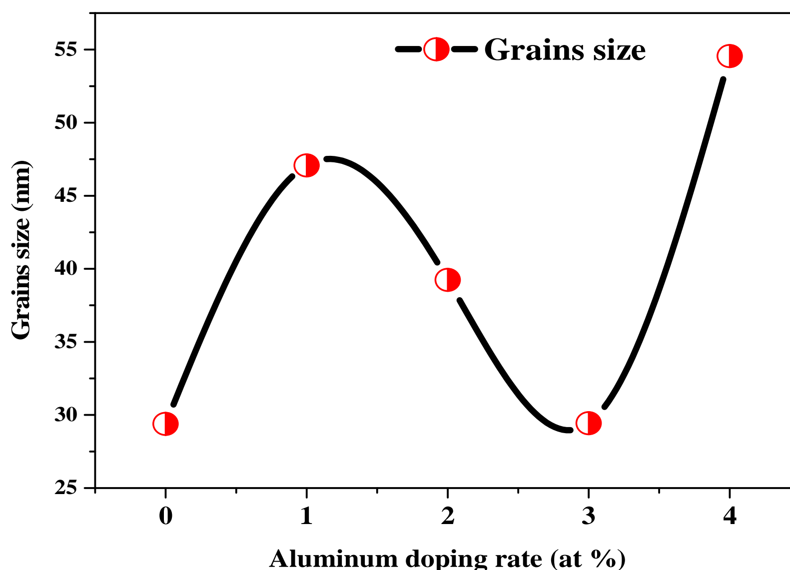

FigIV.17: Grain size of Al-doped ZnO films according to (002) diffraction peak, in dependence of the aluminium doping rates deposited at 1 bar and 400°C.

In fact, during growth of the Al-doped ZnO films, the replacement of Zn^{2+} ions by Al^{3+} ions takes place. Mention that Zn^{2+} radius is greater than that of Al^{3+}, so the grain size decreases with Al incorporation. A minimum size was found, 29,436 nm, in the 3 at% Al-doped ZnO sample, with thickness 342,684 nm, this phenomenon can be attributed to the increasing of the structural defects which can be achieved by development of Al atoms number existing in the lattice [25, 26], and grain growth disturbed by compression stresses due to the difference in ionic radii between Zn and Al [27]. Or probably due by the increment the number of nucleation sites on the substrate causing by doping Al^{3+}ions in Zn^{2+}, therefore, smaller grains

and dense film structure result from the increased degree of preferential alignment. The columnar grain growth enhances with the thickness and it reduces the grain sizes [28].

Tab IV.11: Variation of diffraction angle (2θ), FWHM and intensity with Al-doping rate.

Al-doping rates (at %)	2θ(°)	FWHM	Height	Grains size (nm)
0	34,3076	0,288	33,95	**29,389**
1	34,74	0,18	126,4	**47,078**
2	34,851	0,216	41,5	**39,243**
3	34,8919	0,288	44,36	**29,436**
4	34,87	0,15538	30,03	**54,556**
5	/	/	/	**/**

IV.4.1.2.Stress variation of Al-doped ZnO thin films:

FigIV.18 shows the variation of the stress and peak shift as a function of aluminium doping rates deposited at 1 bar and 400°C as carrier gas pressure and substrate temperature respectively.

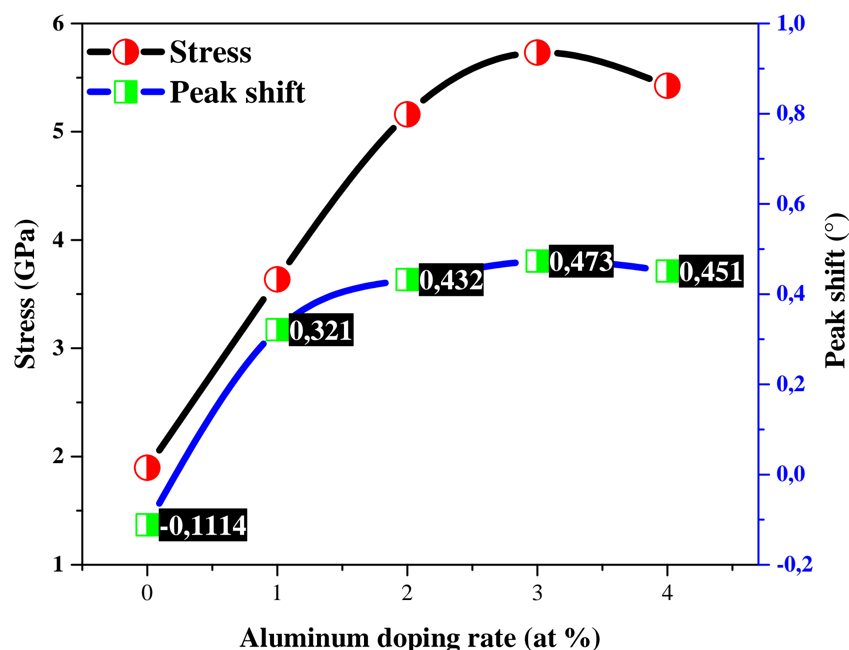

FigIV.18: The variation of the stress and peak shift as a function of aluminium doping rates at 1 bar as air pressure and 400°C substrate temperature.

As can be seen, for undoped ZnO the stress found positive (strain $e_{zz}<0$) suggesting that the film is subjected to compressive stress in the plane of the substrate surface, and to tensile stress for the rest samples. This stress in the thin films is caused by the combined effect of Al-doping in ZnO and thickness [5]. However, the films stress increasing from 1.89 to 5 GPa when the Al doping rates increases (see TabIV.12).

Strains originate, in thin films, principally causes from mismatch between the crystalline film and the amorphous substrate, the difference in the thermal expansion coefficients of the film and the substrate and/or from defects and lattice distortions in the crystal [17, 29], this later can be due to the presence of foreign atoms (Al atoms).

Tab IV.12: Results of Al-doped ZnO thin films deposited at varied aluminium doping rates.

Aluminium doping rate (at %)	(hkl)	d(A°)	C	e_{zz}	$C_{33\ film}$	σ (GPa)
0	(002)	2,6138	5,2277	-0,0044	205,1964	**1,896**
1		2,5823	5,1646	0,0078	215,4097	**-3,636**
2		2,5743	5,1486	0,0108	218,09	**-5,160**
3		2,571	5,1428	0,0120	219,0836	**-5,732**
4		2,5729	5,14589	0,0114	218,5512	**-5,425**
5	/	/	/	/	/	**/**

IV.4.1.3. Film thickness variation of Al-doped ZnO thin films:

Fig IV.19 shows the variation of Al-doped ZnO thin films thickness deposited at different dopant concentration. The film thickness increased from 200 to 350 nm when Al doping rate varied from 0 to 5 at %.

Moreover, as the film thickness increases under Al-doping rate increment effect, the intensity of the (002) peak decreases when Al-doping rate increase from 1 to 4 at% (consider FigIV.15). This suggests that the crystalline quality of the films is impaired and the preferred orientation along the c-axis going to change. The peak intensity and crystallite size are associated with the crystallinity of the films; however, Poor crystallinity in thinner ZnO film could be due to incomplete growth of crystallites [30, 31]. The weakest thickness value found at 4 at % Al doping rate may be due to the appearance of new growth orientation (101), thus, change in the growth model [32].

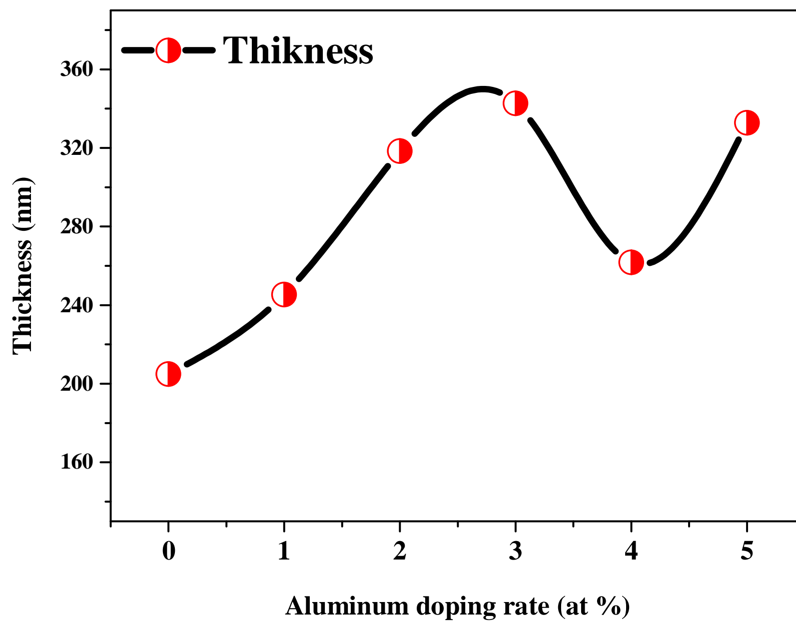

FigIV.19: The variation of Al-doped ZnO thin films thickness deposited at different doping rates.

IV.4.2.*Optical characterization (UV-Vis):*

FigIV.20 displays the optical transmittance at room temperature as a function of wavelength for undoped and Al-doped ZnO thin films. The transmittance spectrum indicates a high degree of optical transparency close to 80% in the visible region, despite 5 at% Al concentration where the transparency reduced less than 50%, which was hardly visible to naked eye. From the transmittance spectra, we note that all spectra have a sharp fundamental absorption edge between wavelength 300 to 360 nm, corresponds to the transition from valence band to the conduction band. This is important for applications such as solar cell, windows and transparent conductive films.

For high Aluminium doping concentration (> 3at %) the transmittance goes to decrease with the Al content, thus may be due to the increase in thickness of the films [26] observed in the current work.

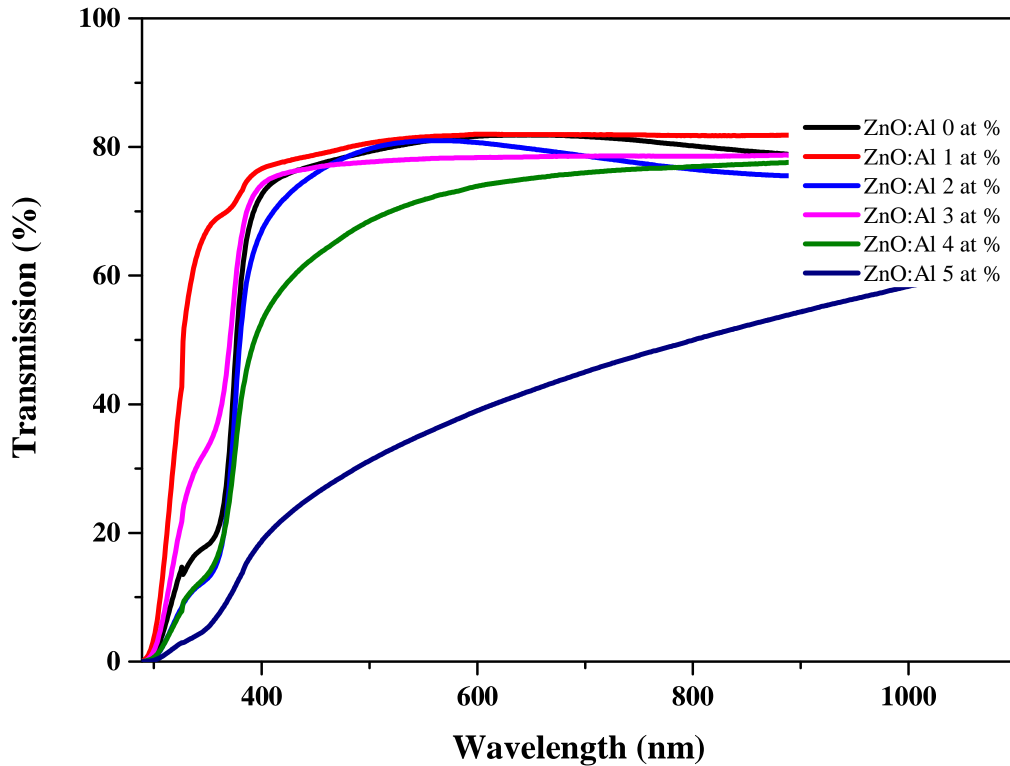

Fig IV.20: Transmittance versus wavelength of Al-doped ZnO thin films grown with different doping rates at 1 bar air pressure and 400°C substrate temperature.

In addition to that, a shift in the absorption edge towards shorter wavelengths for 1 and 3 at% and towards the longer for 2, 4 and 5 at% has observed. This indicates that the optical band gap affected by the dopant incorporation, similar behavior war found by W. L. Liu and Y. F. Zhang [33]. An absence of the interference fringes indicates that the films roughness prepared with these conditions are elevated.

IV.4.2.1.*Band gap energy and Urbach energy of Al-doped ZnO thin films:*

The dependence of optical band gap and Urbach energy on the doping rate for the Al doping ZnO is depicted in FigIV.21. The obtained Eg values of Al-doped ZnO films were illustrated in TabIV.12. As can be seen, increase in the Al doping rate decreased the optical band gap and Urbach energy Eg and Eu respectively.

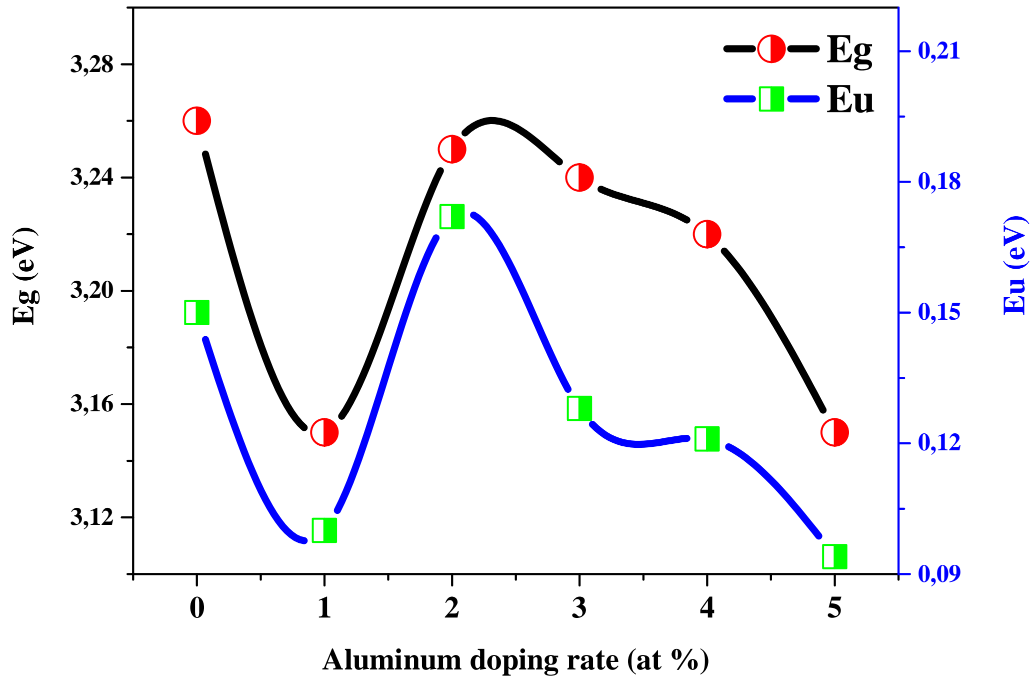

FigIV.21: band gap and Urbach energy of Al-doped ZnO thin films grown with different doping rates.

Similar behavior reported by M. R. Islam et al [36] and P. P. Sahay et al [35]. The direct band gap decrement; with increased Al doping rates may be attributed to the presence of unstructured defects, which increase the density of localized states in the band gap and consequently decrease the energy gap. For the thicker films, these allowed states could well merge with the conduction band resulting in the reduction of the energy band gap [34, 35]. Noted that, high intensity, widest grain size, lowest stress and greatest electrical conductivity were found for the thicker sample, which is Al doping rate equal 1 at%.

Tab IV.13: calculated optical band gap and Urbach energy of Al-doped ZnO thin films.

Aluminium doping rates (at%)	Eg (eV)	Eu (eV)
0	**3,26**	**0,15**
1	**3,15**	**0,1**
2	**3,25**	**0,172**
3	**3,24**	**0,128**
4	**3,22**	**0,121**
5	**3,15**	**0,094**

IV.4.3.*Electrical characterization:*

IV.4.3.1.*Electrical conductivity of Al-doped ZnO thin films:*

Dependence of the film conductivity on Al doping rates for the undoped and Al-doped ZnO thin films are indicated in FigIV.22.

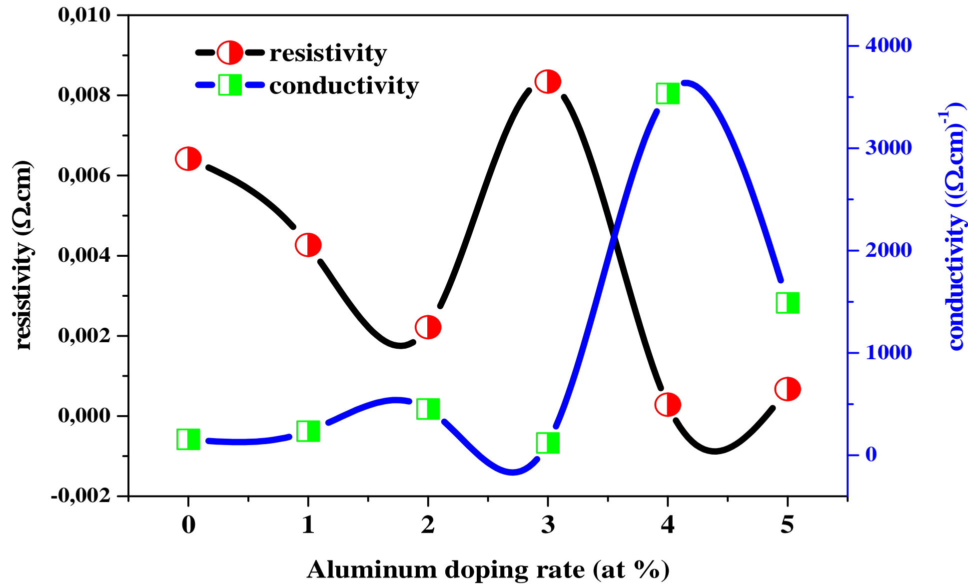

FigIV.22: The variation of electrical conductivity and resistivity of Al-doped ZnO films deposited at 1 bar and 400°C.

It is obvious that there is a decrease in the resistivity with increase of dopant concentration; this is attributed to the large number of free carrier as a result of electrons coming from the donor Al^{3+} ions incorporated as substitutional ions in Zn^{2+} cation sites or in interstitial positions. Moreover, it is possible that the increase of Al doping can also cause a decrease in the crystal grain size, also affecting the mobility [25, 22]. A. A. Al-Ghamdi et al. [21] reported that, with increasing of Al concentration the Al atoms get in more neck contact into Zn sites leading to the acceleration of driving force of charge carrier’s transport, thus conductivity increases.

A maximum resistivity of $83,45\times10^{-4}$ Ω.cm was obtained for films doped with 3 at% aluminium, as shown in TabIV.14**,** witch consistent with highest value of stress found 5,732GPa and lowest value of grain size 29.436 nm obtained for this sample, Which was considered the thickest. While, The highest electrical conductivity of $3,54\times10^{3}$ $(\Omega.cm)^{-1}$ of Al-

doped ZnO thin film was obtained at 4 at% concentration, whereas the biggest grain size 54,56 nm obtained for this sample with film thickness of 261,82 nm. However, the larger grain size and decreased grain-boundary effect resulting from the increased carrier mobility increased the conductivity [36].

Tab IV.14: measured electrical resistivity and conductivity of Al-doped ZnO thin films.

Aluminium doping rates (at %)	l'épaisseur (nm)	I (A)	U (Volt)	Resistivity (Ω.cm)	Conductivity $(\Omega.cm)^{-1}$
0	204,933	0,03	0,9	**$64,16 .10^{-4}$**	**155,857**
1	245,359	0,03	0,5	**$42,68 .10^{-4}$**	**234,3199**
2	318,419	0,03	0,2	**$22,15 .10^{-4}$**	**451,390**
3	342,684	0,03	0,7	**$83,45 .10^{-4}$**	**119,835**
4	261,713	0,03	0,045	**$2,829 .10^{-4}$**	**3534,917**
5	332,819	0,03	0,058	**$6,72 .10^{-4}$**	**1489,173**

IV.4.4.In summary: From the obtained results, for Al-doped ZnO thin films, following conclusions can be drawn:

1. The whole films exhibited a strong orientation along c-axis (002) perpendicular to the substrate surface, which belong to a hexagonal crystal structure; with well crystallinity. For Al-doping ratio 4 at% new diffraction peak appear, (101), thus indicate that the Al incorporation causes a loss of preferential orientate. The Al doping into ZnO lattice may generate different sorts of stress. The crystallite sizes improved by Al doping versus pure ZnO from 29 nm to 55 nm and the film thickness increased from 205 to 343 nm.
2. The transmittance spectrum indicates a high transparency close to 80% in the visible region, despite 5 at% Al concentration where the transparency reduced less than 50%. All spectra have a sharp absorption edge between wavelength 300 to 360 nm. The Al doping rate increment decreased the optical band gap, which found in the range of 3,15 to 3,26 eV.
3. The electrical conductivity increased with Al concentration increment. This is attributed to the large number of free electrons coming from the donor Al^{3+} ions incorporated as substitutional ions or in interstitial positions.

References

[1] X-Y. Li, H-J. Li, Z-J Wang, H. Xia, Z-Y. Xiong, J-X. Wang, B-C. Yang, Optics Communications, 282 (2009) 247-252.
[2] J.W. Jeon, M. Kim, L.W. Jang, J. L. Hoffman, N. S. Kim, and In. H. Lee, Electronic Materials Letters, 8 (2012) 27-32.
[3] A. Rahal, S. Benramache and B. Benhaoua, Engineering Journal, 18(2014) 0125-8281.
[4] M. Othmane, A. Attaf, H. Saidi, F. Bouaichi, N. Lehraki, M. Nouadji, M. Poulain and S. Benramache, International Journal of Nanoscience, 15 (2015) 1650007 (8p).
[5] G. Kaur, A. Mitra and K. L. Yadav, Progress in Natural Science: Materials International, 25 (2015) 12-21.
[6] S. Zargou, S.M. Chabane Sari, A.R. Senoudi1, M. S. Aida, N. Attaf, I.F. Hakem, J. Mater. Environ. Sci, 7 (2016) 3134-3147.
[7] M. Othmane, Synthesis and characterization of Zinc Oxide (ZnO) Thin films deposited by spray pyrolysis for applying: electronics and photonics, doctoral thesis, University Mohamed Khider of Biskra, 2018.
[8] G. A. Kumar, M. R. Reddy, K. N. Reddy, IOP Conf. Series: Materials Science and Engineering, 73 (2015) 012133 (4p).
[9] X. Zhang, S. Ma, F. Li, F. Yang, J. Liu, Q. Zhao, J. Alloys Compd, 574 (2013)149-154.
[10] A. Bedia, F.Z. Bedia, M. Aillerie, N. Maloufi, B. Benyoucef, Energy Procedia, 74 (2015) 529-538.
[11] S. Benramache, B. Benhaoua and F. Chabane, Journal of Semiconductors, 33 (2012) 093001 (5p).
[12] T. K. Roy, D. Sanyal, D. Bhowmick, A. Chakrabarti, Materials Science in Semiconductor Processing; 16 (2013) 332-336.
[13] V. P. Deshpande, S. D. Sartale, A. N. Vyas, A. U. Ubale, International Journal of Materials and Chemistry, 7 (2017) 36-46.
[14] A. Khayatian, V. Asgari, A. Ramazani, S. F. Akhtarianfar, M. AlmasiKashi, S. Safa, Materials Research Bulletin, 94 (2017) 77-84.
[15] B. Godbole, N. Badera, Sh. Shrivastava, D. Jain, V. Ganesan, Materials Sciences and Applications, 2 (2011) 643-648.
[16] M. Saleem, L. Fang, Q. L. Huang, D. C. Li, F. Wu, H. B. Ruan and C. Y. Kong, Surface Review and Letters, 19 (2012) 1250055 (9p).
[17] T. P. Rao, M. C. Santhosh-Kumar, S. A. Angayarkanni, M. Ashok, Journal of Alloys and Compounds, 485 (2009) 413-417.
[18] S. Bensmaine, B. Benyoucef, Physics Procedia, 55 (2014) 144-149.
[19] S. S. Shinde, P. S. Shinde, C. H. Bhosale, K. Y. Rajpure, Journal of Photochemistry and Photobiology B: Biology, 104 (2011) 425-433.
[20] W. Y. Zhang, D. K. He, Z. Z. Liu, L. J. Sun, Z. X. Fu, J. Optoelectron. Adv. Mater, 4 (2010) 1651-1654.
[21] A. A. Al-Ghamdi, O. A. Al-Hartomy, M. El-Okr, A. M. Nawar, S. El-Gazzar, F. El-Tantawy, F. Yakuphanoglu, Spectrochimica Acta Part A: Molecular and Biomolecular Spectroscopy, 131 (2014) 512-517.
[22] A. El-Manounia, F. J. Manjón , M. Mollar , B. Marí , R. Gómez , M.C. López , J. R. Ramos-Barrado, Superlattices and Microstructures, 39 (2006) 185-192.
[23] R. Sabryand, D. KH. Kafi, International Journal of Applied and Natural Sciences, 2 (2013) 29-38.

[24] G. He, Bo. Huang, S. Wu, J. Li, SPIE, 6984 (2008) 69842 (4p).
[25] P. P. Sahay, R. K. Nath, Sensors and Actuators B, 134 (2008) 654-659.
[26] B. Joseph, P. K. Manoj, V. K. Vaidyan, Ceramics International, 32 (2006) 487-493.
[27] C-L. Tsai, Y-J. Lin, Ch-J. Liu, L. Horng, Y-T. Shih, M-Sh. Wang, Ch-Sh. Huang, Ch-Sh. Jhang, Y-H. Chen, H-Ch. Chang, Applied Surface Science, 255 (2009) 8643-8647.
[28] G. Kaur, A. Mitra and K. L. Yadav, Progress in Natural Science: Materials International, 25 (2015) 12-21.
[29] Z. Y. Alami, M. Salem, M. Gaidi, J. Elkhamkhami, Advanced Energy: An International Journal (AEIJ), 2 (2015) 11-24.
[30] S. Rahmane, M. Salah Aida, M. Abdou Djouadi, N. Barreau, Superlattices Microstruct, 79 (2015) 148-155.
[31] V. Kumar, N. Singh, R. M. Mehra, A. Kapoor, L. P. Purohit, H. C. Swart, Thin Solid Films, 539 (2013) 161-165.
[32] F. A. Garcés, N. Budini, R. D. Arce, J. A. Schmidt, Procedia Materials Science, 9 (2015) 221-229.
[33] W. L. Liu and Y. F. Zhang, Integrated Ferroelectrics, 188 (2018) 112-120.
[34] M. R. Islam and J. Podder, Cryst. Res. Technol, 44 (2009)286-292.
[35] P. P. Sahay, S. Tewari and R. K. Nath, Cryst. Res. Technol, 42(2007) 723-729.
[36] E. M. Mkawi, K. Ibrahim, M. K. M. Ali, M. A. Farrukh and A. S. Mohamed, Applied Nanoscience, 5 (2015) 993-1001.

General Conclusion

This thesis work focused on the synthesis and characterization of zinc oxide thin films using spray pyrolysis technique, with two atomization modes, in order to study the effect of the deposition conditions as well as the mode atomization used, on the structural, optical and electrical thin films properties.

In the first part, we have studied the effect of start solution (solute) molarity, aluminium and indium doping rate on the Structural, optical and electrical properties of ZnO thin films deposited using ultrasonic spray pyrolysis. In the second, the effect of spray pressure, substrate temperature and aluminium doping rate on the Structural, optical and electrical properties of ZnO thin films deposited using pneumatic spray pyrolysis has been studied.

From the results acquired during the various characterizations conducted and the corresponding discussions, we can conclude that: A matching of the observed diffraction peaks corresponding to the (100); (002) (101) and (102) planes confirms that the ZnO films synthesized at different start solution molarity exhibit polycrystalline structure that belongs to the hexagonal; and for high solution molarity (> 2 $mol.l^{-1}$) ZnO films suffer high stress. However, all the films showed an average of optical transparency of about 85 % in the visible range, then the decreasing trend of the optical band gap lead an enhancement in the optical transmittance, that when the molarity increasing from 0,05 to 0,5$mol.l^{-1}$, also we have observed, that there is an increment on the electrical conductivity of ZnO films was from 0.023×10^{-2} $(\Omega\text{-cm})^{-1}$ when the molarity of solution was 0,075 $mol.l^{-1}$.

As for the other process when ZnO thin films are doped with aluminium and indium by ultrasonic spray pyrolysis, it's clear that the effect of indium is slightly obvious on the ZnO thin films properties, compare to the ZnO doped by aluminium , whereas all the Al doped ZnO films were polycrystalline with a peaks (002) correspond to the hexagonal wurtzite structure, with diffraction peak of about 34° on X-ray diffraction results, the film thickness taking a highest value390nm at 2 at% of aluminium doping; also when Aluminium concentration was 1at%, we observed that the doped ZnO thin films have an enhanced optical transmittance higher than 85% in the visible range with crystal size of 23 nm, the transparency decreases with Al incorporation. The microscopic observations showed a modification of grain shape with Al content and that the films trend to be denser. The electrical conductivity reveals an increase on its value as the aluminum doping increase, whereas it has the highest value was $6,17\times10^{2}(\Omega.cm)^{-1}$ at 3at% of Al concentration. For

indium doping, whole of doped ZnO films were polycrystalline that belongs hexagonal wurtzite structure; the higher In doping rates changes the preferred growth orientation from (002) to (100); the films thickness increases as the In concentration increases, whereas the bigger value (about 350nm) was found at 3 at%. The UV-Vis results showed that the indium incorporation enhanced the optical transmission of ZnO thin films to become higher than 85%. The electrical conductivity took the maximum value, 0.62×10^{-2} $(\Omega.cm)^{-1}$,at 3 at% of indium concentration, which is considered a promising sample.

For the second part when the pneumatic spay was used to deposit undoped and Al doped ZnO, we can conclude that: All the undoped ZnO thin films, deposited at 1 and 1.5 bar as carrier gas (air) pressure with different substrate temperature, displays a very good orientation perpendicular to substrate surface (c-axis) and an optical transmission sometimes up to 90%. the undoped ZnO thin films prepared at 1,5 bar and 400°C as spray pressure and substrate temperature respectively shows high crystallinity with (002) lone preferred growth orientation; also for this sample the grain size found the biggest (96 nm) with electrical conductivity about $1{,}04\times10^{-2}(\Omega.cm)^{-1}$. Other samples attract attention, which was deposited at 1 bar and 350°C as spray pressure and substrate temperature respectively, whereas it revealed a high crystallinity and transparency; it was also the thicker films (336.3 nm) with grain size around 40 nm and electrical conductivity equal to $1{,}20\times10^{2}(\Omega.cm\ )^{-1}$. For the other process when the ZnO doped by aluminium, the whole films exhibited a strong orientation along c-axis (002) that belong the hexagonal crystal structure, whereas the higher Al doping rate caused a loss of crystallinity, when the Al incorporation induced increasing stresses in the lattice and enhanced the film thickness. The UV-Vis results showed that the Al doping decreased the optical transmission of ZnO thin films to become less than 50% after it was around 80%. The electrical conductivity took the maximum value, 35.35×10^{2} $(\Omega.cm)^{-1}$,at 3 at% of Al concentration.

Finely, we conclude that there is a very important factors to get the best properties between dopant and doping rate, affect directly on the structural, optical and electrical characteristics, this brings us to choose an appropriate concentration rate values. However, based on the above the Al Doped ZnO films deposited by pneumatic spray showed promising electrical and optical properties and they have more advantages than the other due to good stability at acceptable temperatures and lower cost to manufacture.

Abstract:

Deposition and analysis of Zinc Oxide thin films elaborated using spray pyrolysis for photovoltaic applications

Undoped and doped (by Al and In) ZnO thin films were deposited via two types of spray pyrolysis technique, ultrasonic and pneumatic onto glass substrates, to investigate the effect of several factors on the structural, optical and electrical properties of ZnO thin films. In the first part, we have deposited set samples of ZnO thin films using ultrasonic spray pyrolysis process with various start solution molarities for undoped ZnO and various doping concentrations for Al and In doped ZnO films. In the second, ZnO thin films were deposited using pneumatic spray pyrolysis process with two deferent spray pressure (1 and 1,5 bar) and various substrate temperatures for each pressure; also ZnO films with various aluminium doping rates were prepared. As well as, All the ZnO thin films were analyzed by assorted techniques X-ray diffraction, X-ray Dispersive Spectroscopy (EDS), SEM, UV-Vis, Hall Effect, four and two probes technique. This study allowed us to get ZnO thin films with very important structural, optical and electrical properties, which are very promising in photovoltaic applications.

Keywords**:** Spray pyrolysis, ZnO, Ultrasonic, Pneumatic, Molarity, ZnO:Al, ZnO:In, substrate temperature, XRD, SEM, UV-Vis, Electrical properties.

مُلَخَّص:

ترسيب وتحليل الشرائح الرقيقة لأكسيد الزنك المحضرة باستخدام الانحلال الحراري بالرش للتطبيقات الفولتضوئية

قمنا في هذه الدراسة بترسيب شرائح رقيقة من أكسيد الزنك، مطعمة وغير مطعمة (بالألمنيوم والأنديوم)، وذلك بنوعين من تقنية الانحلال الحراري، بالموجات فوق الصوتية والرش الهوائي، لدراسة تأثير مجموعة من العوامل على الخصائص البنيوية، الضوئية والكهربائية لهذه الشرائح. في الجزء الأول، قمنا بتحضير عدة شرائح رقيقة لأكسيد الزنك باستعمال طريقة الانحلال الحراري بالموجات فوق الصوتية وذلك بتراكيز مولية مختلفة للمحلول الابتدائي في حالة الشرائح غير المطعمة وتراكيز تطعيم مختلفة في حالة الشرائح المطعمة بالألمنيوم والأنديوم. بينما في الجزء الثاني، تم تحضير شرائح رقيقة لأكسيد الزنك بطريقة الانحلال الحراري بالرش الهوائي وذلك باستخدام ضغطي رش هوائي مختلفين (1 و 1،5 bar) ودرجات حرارة مسند مختلفة من أجل كل ضغط. كذلك تم تحضير الشرائح مطعمة بتراكيز مختلفة لذرات الألمنيوم.

تم دراسة خصائص جميع الشرائح المحضرة باستخدام مختلف التقنيات: حيود الأشعة السينية، التحليل الطيفي للأشعة السينية EDS، المجهرالالكتروني الماسح، الاشعة فوق البنفسجية-المرئية، مفعول هول، تقنية مسبارين واربعة مسابير للدراسة الكهربائية. في الحقيقة، سمحت لنا هذه الدراسة بالتحصل على شرائح رقيقة لأكسيد الزنك ذات خصائص جد مهمة والتي تعتبر جد واعدة لاستعمالها في التطبيقات الفولتضوئيّة.

الكلمات المفتاحية: الانحلال الحراري، الشرائح الرقيقة لأكسيد الزنك، الموجات فوق الصوتية، الرش الهوائي، المولارية، أكسيد الزنك المطعم ، درجة حرارة المسند، الخصائص البنيوية، الخصائص الضوئية، الخصائص الكهربائية.

Résumé:

Dépôt et analyse de couches minces d'oxyde de zinc élaborées à l'aide d'un spray pyrolyse pour applications photovoltaïques

Des couches minces de ZnO non dopées et dopées (par Al et In) ont été déposées par deux modes de spray pyrolyse, ultrasonique et pneumatique sur un substrat de verre, pour étudier l'effet de plusieurs facteurs sur les propriétés structurelles, optiques et électriques des films minces de ZnO. Dans la première partie, nous avons déposé plusieurs échantillons de films minces de ZnO par spray pyrolyse ultrasonique avec diverses molarités de la solution de départ pour le ZnO non dopé et diverses taux de dopage pour des films de ZnO dopés à l'aluminium et à l'indium. Dans le deuxième, des couches minces de ZnO ont été déposées par le spray pyrolyse pneumatique avec deux différentes pressions de spray (1 et 1,5 bars) et des températures de substrat différentes pour chaque pression; des films de ZnO avec différents taux de dopage en aluminium ont été également préparés. Toutes les couches minces de ZnO ont été analysées par diverses techniques: diffraction des rayons X, analyse EDS, MEB, UV-Vis, effet Hall, technique de quatre et deux pointes. Cette étude nous a permis d'obtenir des couches minces de ZnO ayant des propriétés structurelles, optiques et électriques très importantes, qui sont très prometteuses dans les applications photovoltaïques.

***Mots clés*:** Spray pyrolyse, Couches minces de ZnO, Ultrasonique, Pneumatique, Molarité, ZnO: Al, ZnO: In, température de substrat, DRX, MEB, UV-Vis, propriétés électriques.

Main Group Chemistry 15 (2016) 57–66
DOI 10.3233/MGC-150183
IOS Press

The synthesis and characterization of sprayed ZnO thin films: As a function of solution molarity

Fouad Bouaichi[a], Hanane Saidi[a], Abdallah Attaf[a,*], Mohamed Othmane[a], Nadia Lehraki[a], Malika Nouadji[a], Marcel Poulain[b] and Said Benramache[a]
[a]*Physic Laboratory of Thin Films and Applications LPCMA, University of Biskra, Algeria*
[b]*Photonic Material laboratory, Université de Rennes 1, France*

Abstract. In the present paper, the structural, electrical and optical properties of zinc oxide thin films were studied as a function of solution molarity. The ZnO thin films were deposited on glass substrates via the ultrasonic spray technique at 350°C. Polycrystalline films with a hexagonal wurtzite structure with (100) and (002) preferential orientation corresponding to ZnO films were observed. The optimal values of the crystallite size of the ZnO films were observed with (002) plan in 0.4 and 0.5 mol/l of solution molarity. All films exhibit an average optical transparency about 85%, in the visible region. The shift of optical transmittance towards smaller wavelength can be showed by the decrease of band gap caused by the change of crystallite size in polycrystalline. The maximum electrical conductivity of ZnO films was found of 2.29 $(\Omega.cm)^{-1}$ with 0.075 mol/l of solution molarity.

Keywords: ZnO, thin film, Ultrasonic spray, crystalline structure, optical properties, electrical conductivity

1. Introduction

Zinc oxide (ZnO) has a wurtzite (WZ) structure, this is a hexagonal crystal structure, ZnO is available as large bulk single crystals with lattice parameter: a = 0.3249 nm, c = 0.5206 nm belonging to the space group P63mc, and is characterized by two interconnecting sublattices of Zn^{2+} and O^{2-}, such that each Zn ions is surrounded by a tetrahedron of O ions, and vice-versa [1–4]. Transparent conducting oxides (TCO) (such as ZnO) based glasses have gained much interest in science and technology, which are a unique class of materials based on metal oxides that exhibits both optical transparency, low resistivity and good optical gap energy due to their interesting applications such as transparent conductive, ferromagnetism, semiconductors, piezoelectric and solar cells, and are widely exploited in various technological applications [1–13].

*Corresponding author: Abdallah Attaf, Physic Laboratory of Thin Films and Applications LPCMA, University of Biskra, Algeria. Tel.: +213773681758; Fax: +21333543190; E-mail: ab_attaf@univ-biskra.dz.

ISSN 1024-1221/16/$35.00 © 2016 – IOS Press and the authors. All rights reserved